Llenceu aquesta pàgina i substituïu-la per aquella que us faciliti la Unitat d'Informació i Projecció Institucionals (UIPI), disponible al formulari següent
http://www.upf.edu/uii/sgrafics/formulari_tesi.htm

UNIVERSITAT POMPEU FABRA

Time-Domain Numerical Methods in Room Acoustics Simulations

Wave Propagation, Source Generation and Locally-Reacting Boundary Conditions

CARLOS SPA CARVAJAL

TESI DOCTORAL UPF/2009

Director de la tesi

Dr. Adan Garriga Torres
Centre Intenacional de Mètodes Numèrics en Enginyeria

A Javiera... por todas las cosas que sin ti
nunca hubiera logrado.

A mis padres... por ayudarme siempre,
una y otra vez.

Acknowledgements

I would like to express profound gratitude to my advisors, Dr. Adan Garriga and Dr. Jose Escolano, for their invaluable support, encouragement, supervision and useful suggestions throughout this research work. Their moral support and continuous guidance enabled me to complete my work successfully. I wish to express my appreciation to Dr. Vicente López, General Manager of Barcelona Media Centre d'Innovació and Full Professor of the Technology deparment of UPF, who, as my consultant advisor, helped me overcome my doubts in doing this thesis.

I am as ever, especially indebted to my parents, Mr. Ramon Spa and Ms. Estrella Carvajal for their love and support throughout my life. I also wish to thank my brother, Mr. Ramon Spa Jr. for his support and understanding during my study. Moreover, I am also thankful to Dr. Toni Mateos, Dr. Esteban Maestre, Dr. Alfonso Pérez, Mr. Jaume Durany, and Mr. Alberto Rey, who guided me about the direction of my thesis from the beginning. Finally, my sincere thanks go to my girlfriend, Mrs. Javiera Palma, who shared her love and experiences with me.

Abstract

Room acoustics is the science concerned to study the behavior of sound waves in enclosed rooms. The acoustic information of any room, the so-called impulse response, is expressed in terms of the acoustic field as a function of space and time. In general terms, it is nearly impossible to find analytical impulse responses of real rooms. Therefore, in the recent years, the use of computers for solving this type of problems has emerged as a proper alternative to calculate the impulse responses.

In this Thesis we focus on the analysis of the wave-based methods in the time-domain. More concretely, we study in detail the main formulations of Finite-Difference methods, which have been used in many room acoustics applications, and the recently proposed Fourier Pseudo-Spectral methods. Both methods are based on the discrete formulations of the analytical equations that describe the sound phenomena in enclosed rooms.

This works contributes to the main aspects in the computation of impulse responses: the wave propagation, the source generation and the locally-reacting boundary conditions.

Resum

L'acústica de sales s'encarrega de l'estudi del comportament de les ones sonores en espais tancats. La informació acústica de qualsevol entorn, coneguda com la resposta impulsional, pot ser expressada en termes del camp acústic com una funció de l'espai i el temps. En general, és impossible obtenir solucions analítiques de funcions resposta en habitacions reals. Per tant, en aquests últims anys, l'ús d'ordinadors per resoldre aquest tipus de problemes ha emergit com una solució adecuada per calcular respostes impulsionals.

En aquesta Tesi hem centrat el nostre anàlisis en els mètodes basats en el comportament ondulatori dins del domini temporal. Més concretament, estudiem en detall les formulacions més importants del mètode de Diferències Finites, el qual s'utilitza en moltes aplicacions d'acústica de sales, i el recentment proposat mètode Pseudo-Espectral de Fourier. Ambdós mètodes es basen en la formulació discreta de les equacions analítiques que descriuen els fenòmens acústics en espais tancats.

Aquesta obra contribueix en els aspectes més importants en el càlcul numèric de respostes impulsionals: la propagació del so, la generació de fonts i les condicions de contorn de reactància local.

Preface

In general, the sound distribution produced by the propagation of the acoustic field within a room is strongly related to the geometry of the enclosure and the absorbing properties of the materials. In fact, one can perceive the loudness and the echo of a specific room, leading to a particular distribution of the acoustic variables which depend on position and time.

The acoustic phenomena in rooms are very complex and in general it is extremely hard to find analytical expressions for the complete characterization of the acoustic field. For this reason, the use of computers for predicting the acoustic field in rooms arises as an important contribution in the design of room acoustics.

Nowadays, the room acoustics simulations of real and virtual environments play an important role in different fields. As an example, for giving to architects a tool capable to predict with high accuracy the acoustic features of any room before it is constructed. Similarly, these applications can be used for improving the acoustics of built rooms, such as theaters, auditoriums or concert halls.

Furthermore, in audio processing and multimedia applications, obtaining recorded sounds with a particular echo is commonly demanded in order to give sense of immersion. Sometimes, a particular sound is not possible to record, hence, using room acoustic simulations, we are capable to transform an anechoic sound (sound recorded with no influence of the room) into a sound with an echo obtained with the computer simulations.

Thus, computer room acoustics simulations are an important tool for predicting and improving the acoustics quality of built or unbuilt rooms. Moreover, the computer game and entertainment industries together with the training simulators based on virtual reality technologies need, day after day, to find more realistic auditive sensations in order to create a highly immersive environment with spatial attributes. Therefore, in this document the improvement in room acoustics simulations is treated according to the necessities of the industry of these days.

This document can be downloaded from

http://www.agarriga.org/carlos/phd.pdf

Contents

List of Figures

Abbreviation and Acronyms

1-D	One dimensional
2-D	Two dimensional
3-D	Three dimensional
BC	Boundary Conditions
ABC	Absorbing Boundary Conditions
BEM	Boundary Elements Method
FEM	Finite Elements Method
CAD	Computer Aided Design
W-DWM	Wave Digital Waveguide Mesh
DWM	Digital Waveguide Mesh
ISM	Image Source Methods
RTM	Ray-Tracing method
FDM	Finite-Difference Methods
FDTD	Finite-Difference Time-Domain
PSTD	Pseudo-Spectral Time-Domain
FIR	Finite Impulse Response
FFT	Fast Fourier Transform
LRI	Locally reacting impedance
PDE	Partial Differential Equation
PML	Perfect Matched Layer
SI	International System (units)

Notations and Conventions

Conventions

The next conventions are used throughout this thesis:

- Time-domain scalar quantities are denoted by lowercase characters, e.g., $a(t)$.
- Frequency-domain scalar quantities are denoted by uppercase characters, e.g., $A(\omega)$.
- Time-domain vector quantities are denoted by boldface lowercase characters, e.g., $\mathbf{a}(t)$.
- Frequency-domain vector quantities are denoted by boldface uppercase characters, e.g., $\mathbf{A}(\omega)$.
- Time-domain matrix quantities are denoted by underlined, boldface lowercase characters, e.g., $\underline{\mathbf{a}}(t)$.
- Frequency-domain matrix quantities are denoted by lowercase characters, e.g., $\underline{\mathbf{A}}(\omega)$.
- Discretized vector or matrix are denoted by tilde characters, e.g., $\tilde{\mathbf{a}}$ and $\underline{\tilde{\mathbf{a}}}$

Mathematical operations

$\|\|\cdot\|\|$	L^2 Norm or vector norm
$\int_{-\infty}^{t} f(\tau)d\tau$	Integration operator w.r.t. t
$\mathscr{F}$	Time Fourier Transform
$\mathscr{F}_x$	Spatial Fourier Transform
$\partial/\partial t$	Partial derivative w.r.t. t
$\Re[\cdot]$	Real component
∇	Nabla operator (gradient)
$\Delta = \nabla^2$	Laplace operator
$*$	Convolution operator

S_n	Shift operator
A_n	Average operator

Variables and constants

a_1	Dimensionality constant of the velocity update equations
a_2	Dimensionality constant of the pressure update equation
α	Absorption coefficient
B	Volume Elasticity
c	Speed of sound
c_{num}	Numerical speed of sound
f	Frequency
ϕ	Azimuthal angle
k	Wavenumber
λ	Wavelength
$\underline{\mathbf{m}} = (m_1, m_2, m_3, m_4, m_5, m_6)$	Coefficient matrix of general second order PDE
$\underline{\mathscr{M}}$	Mass matrix
n	Discrete time
$\hat{\mathbf{n}}$	Normal direction of the wall
Ω	three-dimensional enclosure
ω	Angular frequency
$p_{\text{tot}}(\mathbf{x},t)$	Total acoustic pressure
$p_0(\mathbf{x},t)$	Unperturbed acoustic pressure
$p(\mathbf{x},t) = p\|^n_{i,j,k}$	Perturbed acoustic pressure
$q_s(t)$	Sound strength function
R	Reflection coefficient
ρ_0	Density of the air
$\rho_{\text{tot}}(\mathbf{x},t)$	Total density of the air
$\rho(\mathbf{x},t)$	Perturbed density of the air
S	Courant stability number
$s(t)$	Monopole strength
T_c	Temperature expressed in Celsius scale
t	Continuous time
θ	Polar angle
V	two-dimensional domain
$\mathbf{v}_{\text{tot}}(\mathbf{x},t)$	Total particle velocity
$\mathbf{v_0}(\mathbf{x},t)$	Unperturbed particle velocity
$\mathbf{v}(\mathbf{x},t)$	Perturbed particle velocity
$v_x(\mathbf{x},t) = v_x\|^n_{i,j,k}$	x component of the perturbed particle velocity
$v_y(\mathbf{x},t) = v_y\|^n_{i,j,k}$	y component of the perturbed particle velocity
$v_z(\mathbf{x},t) = v_z\|^n_{i,j,k}$	z component of the perturbed particle velocity
$\mathbf{x} = (x,y,z)$	Continuous cartesian coordinates

$\tilde{\mathbf{x}} = (i, j, k)$	Discrete cartesian coordinates
x_0	x-position at t=0
Ψ	constant of the Parametric algorithm
Z	Acoustic impedance

Chapter 1

Introduction and Scope

1.1 Motivation and Scope of the Thesis

Room acoustics is the science devoted to study sound propagation in enclosures. In closed environments the sound is heard as a combination of a direct sound (straight from a source/sources) and indirect reflections from surfaces and other objects in the enclosure.

The analytical formulation of the sound variables distribution is, in general, extremely hard to obtain in real scenarios. In fact, there only exist solutions of very simple and unrealistic scenarios. Therefore, it is necessary to use computers for predicting proper solutions of the sound distribution [Schroeder (1973)].

Usually, two big groups are considered to classify computer room acoustic simulations [Savioja (1999)]: geometrical and wave-based methods. The first group embraces a set of algorithms based on the assumption that sound wavelengths are significantly smaller than the size of obstacles found in the room. Among these methods, the most popular ones are the ray-tracing based algorithms [Krokstad et al. (1968)], the image-source method [Allen & Berkley (1979)] and the recently proposed beam tracing methods [Funkhouser et al. (2004)], which have been succesfully applied to light simulations. Although these illumination techniques have been used for sound simulations, in order to achieve sense of presence, sound has different features than light which introduce several new and interesting challenges.

For example, one important feature that makes sound more difficult to treat in a computational way than light simulations, is its large audible frequency bandwidth, that goes from 20 to 20000 Hz. Consequently, the range of audible wavelengths is comprised between $0.02m$ and $17m$ which are five to seven orders of magnitude longer than visible range. Diffraction of sound occurs around the obstacles of the same size as the wavelength. So, sound simulations, instead of light simulations, must take into account more details of the enclosures (such as tables or even smaller objects as coffee mugs). Moreover, speed of sound is six

orders of magnitude less than light, and sound propagation delays are perceptible to humans. Thus, acoustic models must compute the exact time/frequency distribution of propagation paths, in contrast of the propagation delay of light that can be ignored in most applications. Furthermore, for sound waves, not only diffraction but interference phenomena must be considered. Finally, it is worth mentioning that the human ear is sensitive to five orders of magnitude difference in sound amplitude.

For those reasons, the second group of wave-based methods arises as a very interesting alternative. These methods are based on numerical solutions of the partial differential equations that govern the sound propagation in rooms. A room is characterized by its geometry and by the materials of the walls, ceiling and floor, which are the boundary conditions of the system. Since to analytically solve a boundary value problem is not straightforward, wave-based methods are the best option to found a solution with a high degree of accuracy. From that point of view, a considerable number of alternatives are commonly applied: from the frequency-based ones, such as Finite Element Methods [Wright (1995); Savioja et al. (1996a)] or Boundary Element Methods; to the time-based ones, such as Finite Difference in the Time Domain (FDTD) [Botteldooren (1994); Savioja et al. (1996b)] or Digital Waveguide Mesh methods (DWM) [Murphy et al. (2007)].

All these wave methods provide different advantages and disadvantages depending on their computational cost and complexity. However, the most prominent difference lies in their applicability: the frequency-based methods provide results for a particular frequency, and thus, for steady-state situations; whereas if the scope of the simulation is to predict the impulse responses of an enclosure, the time-domain methods need just one simulation to obtain the results. For that reason, this last group of simulation methods is widely used in room acoustics, where the computation of impulse responses is a central issue.

The most important time-domain (or discrete-time) methods used for this purpose are the previously mentioned FDTD and DWM, together with their more sophisticated variants such as the interpolated [Savioja & Välimäki (2003)] and the triangular/tethraedrical [Fontana & Rocchesso (1998); VanDuyne & Smith (1995); Campos & Howard (2005)] DWM. Recently other alternative methods such as the Transmission Line Matrix [Miklavcic & Ericsson (2004)] (TLM) and Functional Transformation Method (FTM) [Petrausch & Rabenstein (2005)] have been proposed as an alternative methods. The scope of all these methods is to improve the propagation features of simulated waves, since the discretization process provides an inherent dispersion, (i.e. the numerical speed of sound has a frequency/direction dependence).

Over the past decade, many studies in the area of FDTD and DWM modelling of 2D and 3D acoustic systems have focused on reducing and/or compensating the dispersion error. An alternative to the common time-domain methods are the emerging class of spectral algorithms known as Pseudo-Spectral Time Domain (PSTD) methods. The most popular PSTD method is the so-called Fourier spectral method [Liu (1997)] which uses Fourier transforms for computing the

spatial derivatives. Due to the fact that spatial derivatives are evaluated in a Fourier basis, the Fast Fourier Transform algorithm [Cooley & Tukey (1965)] can be used for the efficient computation of the derivatives. A major further advantage over the FDTD method is the low numerical dispersion that is observed [Liu (1997); Taflove (1995); Spa et al. (2009)]. The numerical accuracy of the Fourier spectral method for the determination of phase properties in a given structure is therefore improved with respect to the common FDTD methods. In the last years PSTD have been used in different fields such as the propagation of acoustic waves [Liu (1998)], modelling of piezoelectric transducers [Filoux et al. (2008)] or simulation of photonic devices [Pernice (2008)].

Recently, more attention has been given to another problems such as the formulation of better numerical boundary approximations, in particular the implementation of locally-reacting boundaries. In general terms, realistic boundaries can be efficiently approximated by locally-reacting walls. On the other hand, the sound source generation becomes a difficult task since the emission of a unit impulse signal needs to be approximated for keeping stable the numerical simulation.

Both topics should be carefully treated in order to obtain correct and accurate impulse responses. The different approximations of each method have a considerable influence in the final results, affecting the perception of the spatial sound distribution when this information is used for example, in auralization problems [Kleiner et al. (1990)].

The main scope of this thesis is:
To analyse the generation of proper impulse signals, in order to obtain accurate computational solutions of the acoustic features of the simulated enclosures and, to contribute to boundary conditions modelling in the discrete time methods, which results in allowing one to include locally reacting impedances with a reduced computational cost. These investigations will be applied to Finite Difference and Pseudo-Spectral methods, both in the time domain. Their corresponding results will be validated through comparison to their analytical expressions.

1.2 Disposition of the Subjects

This Thesis is organized as follows:

- Chapter 2: This chapter presents a brief summary of the basic mathematical and physical fundamentals involved in sound propagation in enclosures, giving special attention to the boundary conditions and sound source modelling in room acoustics. These notions are necessary for proper comprehension of this dissertation; however, a reader with some experience in this field, could just overview this chapter.

- Chapter 3: Once defined the mathematical and physical foundations of sound propagation in a room, we present and study various approaches

used in room acoustics. Furthermore, we justify the suitability of the so-called discrete methods for room acoustic simulation focusing on the finite-difference time-domain (FDTD) and pseudo-spectral time-domain (PSTD) methods.

- Chapter 4: In this chapter, we overview the most common FDTD and PSTD algorithms for either the Euler or the Wave equation. One important drawback derived from the discrete formulation of these algorithms is that they cause non-physical dispersion error. This error is analyzed with detail, comparing with numerical data obtained in 2D experiments.

- Chapter 5: This chapter discusses the sound source generation of unit impulse signals in numerical simulations. This subject has never been treated before in the context of room acoustics. Firstly, we present the mathematical formulation of the 2D and 3D Green functions, which gives information of the sound propagation in the free space. Furthermore, we study two different numerical source generation: the so-called the soft and the hard source. Finally, we present numerical results of FDTD and PSTD simulations using both types of sources.

- Chapter 6: One of the most important aspects in room acoustics is the definition of numerical boundary conditions to realistically simulate the effect of sound reflection in a wall. In this chapter, we overview the main formulations of numerical impedance boundary conditions for FDTD. Furthermore, we present, for the first time, the implementation of numerical boundary conditions for PSTD methods. All the formulations done have been validated through 2D experiments in order to test the accuracy of the numerical schemes.

- Chapter 7: Finally, conclusions obtained in this dissertation are presented, including some guidelines for future research.

Additionally, two appendixes are presented for completeness:

- Appendix A: presents different formulation of the absorbing perfectly matched layers (PML). These numerical equations are used in PSTD methods in order to avoid the Gibbs phenomenon produced in the contours of the simulations.

- Appendix B: studies the stability analysis of different FDTD and PSTD impedance boundary conditions presented in Chap. 6.

Chapter 2

Background

2.1 Introduction

We have already seen that sound propagation has several aspects that make it difficult to treat in the low frequency range. In fact, the wave-based methods are the proper manner to solve this problem, since they take into account the wave behavior of the sound phenomena. In this current chapter, we present a brief overview of the basic properties of the sound propagation. Moreover, The partial differential equations (PDE) that govern the sound propagation in the free space are formulated and studied in detail (Sec. 2.2 and 2.2.1). In addition, we overview the main solutions of the wave equation (Sec. 2.2.2) and the mathematical and physical background of source generation is presented in Sec. 2.2.3.

Once defined and studied the motion equations of the sound propagation in the free space, we focus the analysis on the sound propagation in enclosures (Sec. 2.3). We present the analytical expressions that are needed to characterize the acoustic properties of the boundaries. More concretely we focus on the study of locally-reacting boundary conditions since it is a simple and accurate way to model the behavior of the real boundaries (see Sec. 2.3.1). In addition, we present in Sec. 2.3.3 some mathematical concepts concerning to the Fourier transform. Furthermore, we expose the mathematical formulation needed for establishing proper analytical expressions employed for the computation of impulse responses (see Secs. 2.3.2 and 2.3.4). Finally, in Sec. 2.4 we expose the conclusions.

2.2 The Physics of Sound

Waves are a physic phenomenon that is defined as the propagation of energy of a periodic perturbation without any transport of matter [Tipler (2006)]. It is easy to observe this kind of behavior daily: waves on the sea, vibrations on a string, sound waves, TV and radio signals, X-rays, light... There exist two different types

of waves depending on their nature: electromagnetic and mechanical waves.

- Electromagnetic waves exist as a consequence of two effects: a variable magnetic field that yields an electric field or a variable electric field that yields a magnetic field. Electromagnetic waves do not need a medium to propagate and can propagate in vacuum. These waves propagate in a perpendicular direction of both fields, electric and magnetic and travel through vacuum with a velocity equal to the velocity of light.
- Mechanical waves need a medium for their propagation (they can not propagate in vacuum). In this case, the propagation of a perturbation is driven by the particles of the medium (solid, liquid or gas). There are two types of mechanical waves: transverse waves and longitudinal waves. Transverse waves are produced when the particles of the medium move in a perpendicular direction of the traveller waves. Sound waves travelling through air are the paradigmatic example of longitudinal waves. Air particles vibrate producing changes in pressure and density alternating compressions and rarefactions all over the direction of the movement of the wave.

The sound waves are described as compressional oscillatory disturbances that propagate in a fluid [Jacobsen (2007)] or as a result from the time varying perturbation of the dynamic and thermodynamic variables that describe the medium [Pierce (2007)]. Therefore, the classical model of compressible fluid in the free space presumes the existence of some relation between density, ρ, and pressure p,

$$p = p(\rho)\,. \tag{2.1}$$

Moreover, the basic laws for the sound propagation are the law of conservation of mass (the continuity equation) and the Newton's second law of motion (the momentum equation) which both explicit forms read:

$$\frac{\partial \rho_{\text{tot}}(\mathbf{x},t)}{\partial t} + \nabla \cdot (\rho_{\text{tot}}(\mathbf{x},t)\mathbf{v}_{\text{tot}}(\mathbf{x},t)) = 0\,, \tag{2.2}$$

$$\rho_{\text{tot}}(\mathbf{x},t)\left(\frac{\partial \mathbf{v}_{\text{tot}}(\mathbf{x},t)}{\partial t} + \mathbf{v}_{\text{tot}}(\mathbf{x},t)\cdot(\nabla \cdot \mathbf{v}_{\text{tot}}(\mathbf{x},t))\right) = -\nabla p_{\text{tot}}(\mathbf{x},t)\,, \tag{2.3}$$

where $\nabla = (\frac{\partial}{\partial x}, \frac{\partial}{\partial y}, \frac{\partial}{\partial z})$, p_{tot} is the acoustic pressure, ρ_{tot} the total density and $\mathbf{v}_{\text{tot}}$ represents the total particle velocity. Commonly, the two main propagation media are air (aeroacoustics) and water (underwater acoustics). A third important medium, with properties close to those of water, is the human body, i.e. biological media (ultrasonography). The characteristics of these two main fluids, air and water, can also be considered as references for the two states of fluids: the gaseous and the liquid states. These two states, the first characterized by strong compressibility and the second by weak compressibility, have homogeneous

characteristics within a state and characteristics than differ greatly from one state to the other. Generally, sound waves can propagate in any fluid with a velocity that depends on its mechanical properties. Therefore, the speed of sound propagation depends, generally, on the elastic and inertial properties of the medium:

$$c = \sqrt{\frac{B}{\rho}} \quad , \tag{2.4}$$

where B is the volume elastic property and ρ is the density of the medium. Likewise, the speed of sound is related with the temperature of the medium. For sound waves moving through the air, the relation between speed of sound and temperature is given by the simple expression:

$$c = 331\sqrt{1+\frac{T_c}{273}} \quad , \tag{2.5}$$

where 331 m/s is the velocity of sound through air at 273, and T_k is the temperature of the fluid in Celsius. Although the temperature usually depends on the density distribution of the fluid within the enclosure, it is commonly assumed in room acoustic applications that the temperature has an homogeneous distribution along the domain leading to a constant speed of sound propagation. More concretely, characteristics of the air are given at standard pressure and temperature in International system units (SI): $p_0 = 1$ atm $= 10^5$ N m^{-2}, $T_0 = 20^o$ C $= 293$ K. Air behaves like a perfect gas with $\rho_0 \sim 1.21$ Kg m^{-3}, so that $c = 340$ m s^{-1}.

Acoustics is the science devoted to the study of small amplitude disturbances in a fluid. Considering the classical case of infinitesimally small perturbation in velocity and pressure in a stagnant fluid, the total particle velocity in fluid $\mathbf{v}_{\text{tot}}$, total pressure p_{tot} and total density ρ_{tot} can be written:

$$\mathbf{v}_{\text{tot}} = \mathbf{v_0} + \mathbf{v} = \mathbf{v} \quad ; \quad p_{\text{tot}} = p_0 + p \quad ; \quad \rho_{\text{tot}} = \rho_0 + \rho \ , \tag{2.6}$$

where $\mathbf{v_0}$, p_0 and ρ_0 are the velocity, the pressure and density for the unperturbed fluid and $\mathbf{v} = (v_x, v_y, v_z)$, p and ρ are the perturbed quantities. For stagnant fluid, $\mathbf{v_0} = 0$. Substituting Eq. (2.6) into Eqs. (2.2) and (2.3) and expanding in Taylor series, Eq. (2.4), we obtain the following system of equations

$$\frac{\partial}{\partial t}(\rho_0 + \rho(\mathbf{x},t)) = -\nabla \cdot [\rho_0 + \rho(\mathbf{x},t)\mathbf{v}(\mathbf{x},t)] \ , \tag{2.7}$$

$$(\rho_0 + \rho(\mathbf{x},t))\left(\frac{\partial}{\partial t} + \mathbf{v}(\mathbf{x},t)\cdot\nabla\right)\mathbf{v}(\mathbf{x},t) = -\nabla \cdot (p_0 + p(\mathbf{x},t)) \ , \tag{2.8}$$

$$p_0 + p(\mathbf{x},t) = p(\rho_0 + \rho(\mathbf{x},t)) \ . \tag{2.9}$$

The terms of Eqs. (2.7) and (2.8) can be grouped into zero-terms and if Eq. (2.9) is expanded through Taylor series around ρ, a system of coupled PDE so-called

linear Euler equations for $\mathbf{v}$ and p is obtained [Pierce (2007)] that can be written in shorthand notation as:

$$\rho_0 \frac{\partial \mathbf{v}(\mathbf{x},t)}{\partial t} + \nabla p(\mathbf{x},t) = 0 \,, \tag{2.10}$$

$$\frac{\partial p(\mathbf{x},t)}{\partial t} + \rho_0 c^2 \nabla \mathbf{v}(\mathbf{x},t) = 0 \quad , \tag{2.11}$$

Therefore, Eqs. (2.10) and (2.11) are written explicitly,

$$\rho_0 \frac{\partial v_x(\mathbf{x},t)}{\partial t} + \frac{\partial p(\mathbf{x},t)}{\partial x} = 0 \,, \tag{2.12}$$

$$\rho_0 \frac{\partial v_y(\mathbf{x},t)}{\partial t} + \frac{\partial p(\mathbf{x},t)}{\partial y} = 0 \,, \tag{2.13}$$

$$\rho_0 \frac{\partial v_z(\mathbf{x},t)}{\partial t} + \frac{\partial p(\mathbf{x},t)}{\partial z} = 0 \,, \tag{2.14}$$

$$\frac{\partial p(\mathbf{x},t)}{\partial t} + \rho_0 c^2 \left(\frac{\partial v_x(\mathbf{x},t)}{\partial x} + \frac{\partial v_y(\mathbf{x},t)}{\partial y} + \frac{\partial v_z(\mathbf{x},t)}{\partial z} \right) = 0 \quad . \tag{2.15}$$

Note that Eq. (2.10) involves Eqs. (2.12) to (2.14). On the other hand, this PDE system can easily be expressed as a single uncoupled equation. If Eq. (2.10) is multiplied by ∇ and Eq. (2.11) by $\frac{\partial}{\partial t}$ and they are subtracted, we obtain the well-known wave equation:

$$\frac{\partial^2 p(\mathbf{x},t)}{\partial t^2} - c^2 \Delta p(\mathbf{x},t) = 0 \ , \tag{2.16}$$

where $\Delta = \nabla \cdot \nabla = \frac{\partial^2}{\partial x^2} + \frac{\partial^2}{\partial y^2} + \frac{\partial^2}{\partial z^2}$. Equation (2.16) shows that the properties of linearized acoustic field are governed by the wave equation.

2.2.1 Hyperbolic Behavior of the Wave Equation

It is important for the computational scientist to know that there are different classes of PDEs. Just as different solution techniques are called for in the linear versus the nonlinear case, different methods are required for the different classes of PDEs, whether the PDE is linear or nonlinear. The need for this specialization in the approach is rooted in the physics from which the different classes of PDEs arise. By analogy with the conic sections (ellipse, parabola and hyperbola) partial differential equations have been classified as elliptic, parabolic and hyperbolic. Just as an ellipse is a smooth, rounded object, solutions to elliptic equations tend to be quite smooth. Elliptic equations generally arise from a physical problem that involves a diffusion process that has reached equilibrium, a steady state temperature distribution, for example. The hyperbola is the disconnected conic section. By analogy, hyperbolic equations are

able to support solutions with discontinuities, for example a shock wave. Hyperbolic PDEs usually arise in connection with mechanical oscillators, such as a vibrating string, or in convection driven transport problems. Mathematically, parabolic PDEs serve as a transition from the hyperbolic PDEs to the elliptic PDEs. Physically, parabolic PDEs tend to arise in time dependent diffusion problems, such as the transient flow of heat in accordance with Fourier's law of heat conduction.

For illustrative purposes, we study the one dimensional wave equation derived in Eq. (2.16). The explicit form of the PDE reads

$$\frac{\partial^2 p(x,t)}{\partial t^2} - c^2 \frac{\partial^2 p(x,t)}{\partial x^2} = 0 \,. \tag{2.17}$$

In terms of general second order PDE defined by

$$m_1 \frac{\partial^2 f(x,t)}{\partial x^2} + m_2 \frac{\partial^2 f(x,t)}{\partial x \partial t} + m_3 \frac{\partial^2 f(x,t)}{\partial t^2} + m_4 \frac{\partial f(x,t)}{\partial x} + m_5 \frac{\partial f(x,t)}{\partial t} + m_6 = 0 \;, \tag{2.18}$$

where coefficients m_1 to m_3 may depend on x,t,$\partial f(x,t)/\partial x$ and $\partial f(x,t)/\partial t$, the coefficients m_4 to m_6 may depend on x and t. The terminology of elliptic, parabolic and hyperbolic chosen to classify PDEs reflects the analogy between the form of the discriminant, $(m_2)^2 - 4m_1m_3$, for PDEs and the form of the discriminant, $(m_2)^2 - 4m_1m_3$, which classifies the conic sections[Hoffman (1992)]. In Eq. (2.17), $m_1 = 1$, $m_2 = 0$ and $m_3 = -c^2$. The discriminant, $(m_2)^2 - 4m_1m_3$, is

$$(m_2)^2 - 4m_1m_3 = 0 - 4(1)(-c^2) = 4c^2 > 0 \;. \tag{2.19}$$

Consequently, Eq. (2.17) is an hyperbolic equation. Therefore, Eq. (2.16) has the same properties, since they involve the same differential operators (i.e., $\frac{\partial^2}{\partial t^2} = c^2[\frac{\partial^2}{\partial x^2} + \frac{\partial^2}{\partial y^2} + \frac{\partial^2}{\partial z^2}]$). The characteristics associated with Eq. (2.17) are determined by performing a characteristic analysis. One relationship for determining the second derivatives of $p(x,t)$ is given by the partial differential equations itself, Eq. (2.17). Two more relationships are obtained by applying the chain rule to determine the total derivatives, which are themselves functions of x and t. Thus,

$$d\left(\frac{\partial p(x,t)}{\partial x}\right) = \frac{\partial^2 p(x,t)}{\partial x^2} dx + \frac{\partial^2 p(x,t)}{\partial x \partial t} dt \;, \tag{2.20}$$

$$d\left(\frac{\partial p(x,t)}{\partial t}\right) = \frac{\partial^2 p(x,t)}{\partial t \partial x} dx + \frac{\partial^2 p(x,t)}{\partial t^2} dt \;. \tag{2.21}$$

Equations (2.17), (2.20) and (2.21) can be written in matrix form as follows:

$$\begin{pmatrix} 1 & 0 & -c^2 \\ dt & dx & 0 \\ 0 & dt & dx \end{pmatrix} \begin{pmatrix} \frac{\partial^2 p(x,t)}{\partial t^2} \\ \frac{\partial^2 p(x,t)}{\partial x \partial t} \\ \frac{\partial^2 p(x,t)}{\partial x^2} \end{pmatrix} = \begin{pmatrix} 0 \\ d\left(\frac{\partial p(x,t)}{\partial x}\right) \\ d\left(\frac{\partial p(x,t)}{\partial t}\right) \end{pmatrix} \;. \tag{2.22}$$

Eq. (2.22) can be solved by Cramer's rule [Hoffman (1992)] to yield unique finite values of $\frac{\partial^2 p}{\partial t^2}$, $\frac{\partial^2 p}{\partial x \partial t}$ and $\frac{\partial^2 p}{\partial x^2}$, unless the determinant of the coefficient matrix vanishes. In that case, the second derivatives of $p(x,t)$ are either infinite, which is physically meaningless, or they are indeterminate, and thus multivalued or discontinuous. Setting the determinant of the coefficient matrix of Eq. (2.22) equal to zero yields

$$(dx)^2 - c^2(dt)^2 = 0 \ , \tag{2.23}$$

solving for dx/dt gives

$$\frac{dx}{dt} = \pm c^2 \ , \tag{2.24}$$

$$x = x_0 \pm ct \ . \tag{2.25}$$

Eq. (2.24) shows that there are two real distinct roots associated with the characteristic equations, and Eq. (2.25) shows that the characteristic path are straight lines having the slope $1/c$ in the $x-t$ plane, so the speed of propagation of information along these paths is c. Consequently, information propagates at the acoustic speed c along the characteristic paths. The finite speed of propagation of information and the finite domain of dependence and range of influence must be accounted for when solving hyperbolic PDEs.

2.2.2 Solutions of the Wave Equation

One of the basic solutions of the wave equations are the plane waves, which play a key point in many applications. In fact, plane waves are considered as the basic representation of the sound propagation which can be expressed as follows

$$p(\mathbf{x},t) = Pe^{\imath(\mathbf{k}\cdot\mathbf{x}-\omega t)} \ , \tag{2.26}$$

where $P = P(\omega)$ is the pressure amplitude, ω is the angular frequency, $\mathbf{k}$ is the wavenumber and $\imath = \sqrt{-1}$. The angular frequency is related to the frequency f through

$$\omega = 2\pi f \ , \tag{2.27}$$

note that f is measured in Hertz (Hz) and it indicates the number of oscillations in a second. The temporal period T can also be introduced as the inverse of the frequency. On the other hand, the modulus of wavenumber is define as

$$||\mathbf{k}|| = \frac{\omega}{c} \ , \tag{2.28}$$

where each wavenumber component is usually defined as

$$k_x = ||\mathbf{k}|| \cos\phi \sin\theta \ , \tag{2.29}$$

$$k_y = ||\mathbf{k}|| \cos\phi \cos\theta \ , \tag{2.30}$$

$$k_z = ||\mathbf{k}|| \cos\theta \ , \tag{2.31}$$

the polar and the azimuthal angle are represented by θ and ϕ, respectively. At the same time, wavelength λ is defined as an inverse of the wavenumber as the following way

$$\lambda = \frac{2\pi}{||\mathbf{k}||} \ . \tag{2.32}$$

Sound waves are divided into three categories that cover a wide range of frequencies. Sonic waves (20 Hz-20000 Hz), infrasonic waves ($f < 20$ Hz) and ultrasonic waves ($f > 20000$ Hz). Therefore, the range of audible wavelengths of sound are comprised between 0.02 m and 17 m. It implies that wave phenomena such as diffraction or interference occur around the obstacles of the same size as the wavelength. We will see in the chapter 3 that these phenomena make sound propagation difficult to simulate. Although there are many methods based on approximations of sound propagation since they do not assume the wave behavior of the sound, it is important to consider it in room acoustics applications in order to improve the results in the low frequency bandwidth.

2.2.3 Sound Sources

Sources that are some distance from bounding surfaces and that are small compared to a wavelength can frequently be described by source terms. The simplest such source would be one that causes a net amount of mass or fluid to flow out of or into a fixes surface that encases it. This mass passing out per time divided by the density ρ is quantity $q_s(t)$ termed the sound strength function [Rossing (2007)].

If such a source is concentrated to a point $\mathbf{x_0} = (0,0,0)$, then the appropriate inhomogeneous Euler equations take the following form

$$\begin{aligned} \rho_0 \frac{\partial \mathbf{v}(\mathbf{x},t)}{\partial t} + \nabla p(\mathbf{x},t) &= 0 \\ \frac{\partial p(\mathbf{x},t)}{\partial t} + \rho_0 c^2 \nabla \mathbf{v}(\mathbf{x},t) &= \rho q_s(t)\delta(\mathbf{x}) \ . \end{aligned} \tag{2.33}$$

The Dirac delta function, often referred to as the unit impulse function and introduced by the British theoretical physicist Paul Dirac. Dirac delta function can be loosely thought of as a function on the real line which is zero everywhere except at the origin, where it is infinity.

$$\delta(\mathbf{x}) = \begin{cases} \infty & \text{if } \mathbf{x} = 0, \\ 0 & \text{otherwise} \end{cases} \tag{2.34}$$

and which is also constrained to satisfy the identity

$$\int_{-\infty}^{+\infty} \delta(\mathbf{x}) d\Omega dt = 1 \ , \tag{2.35}$$

where Ω is the integration domain. It is very common to consider this type of source since they are used to approximate typical sources such as voices or instruments. Similarly, Eq. (2.33) can be transformed to the wave equation changing the source term as follows,

$$\frac{\partial^2 p(\mathbf{x},t)}{\partial t^2} - c^2 \Delta p(\mathbf{x},t) = -\rho \frac{\partial q_s(t)}{\partial t} \delta(\mathbf{x}) \,, \tag{2.36}$$

The solution of the above inhomogeneous equation for an isolate source at the origin $\mathbf{x_0} = 0$ in an unbounded region is

$$p = \frac{s(t - ||\mathbf{x}||/c)}{||\mathbf{x}||} \,, \tag{2.37}$$

where

$$s(t) = \frac{\rho}{4\pi} \frac{\partial q_s(t)}{\partial t} \tag{2.38}$$

and $s(t)$ is called the monopole strength. If $s(t) = \delta(t)$, the unit impulse signal is defined. This type of sources are used for obtaining the Green's function (i.e. acoustic response) which is one of the aims in room acoustics applications (see Sec 2.3.2).

2.3 Basic Concepts in Room Acoustics

Up to now we have dealt with sound propagation on unbounded medium in every direction. In contrast to this simple situation, room acoustics is concerned with sound propagation in enclosures where the sound conducting medium is bounded on all sides by walls, ceiling and floor. These room boundaries usually reflect a certain fraction of the sound energy impinging on them. Another fraction of the energy is 'absorbed' (i.e. it is extracted from the sound field inside the room, either by conversion into heat or by being transmitted to the outside by the walls). It is just this combination of the numerous reflected components which is responsible for what is known as 'the acoustics of a room' and also for the complexity of the sound field in a room.

Basically, the sound distribution in a room is the consequence of the complex sound wave phenomena appearing due to the geometric distribution and absorbing properties of the room [Kutruff (2000)]. This makes that people can distinguish and perceive different *colors* or modifications of the same sound in different rooms. Furthermore, the particular combination of the acoustic phenomena such as diffraction, frequency-dependent absorption, diffusion... gives a distribution of acoustic variables which strongly depends on position and time.

These wave phenomena contribute to the complexity of the sound field since they commonly appear in typical room acoustics simulations. For example, diffraction phenomenon appears when obstacles are of the same size that the wavelength associated to the signal. In those cases, sound expands over the

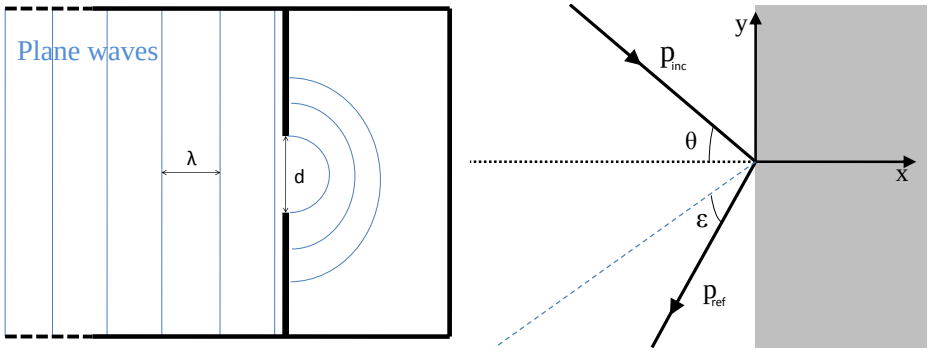

Figure 2.1: (Left) The diffraction phenomenon: Plane waves of wavelength λ travelling throughout a hole of size d similar than λ. Sound expands over the domain next to the opening. (Right) An incident wave with orientation θ strikes on a diffusive material that reflects the sound field with an orientation $\theta + \varepsilon$ different than the specular direction θ.

obstacle and rounds it according to its wave behavior. In Fig. 2.1 (left), we illustrate the diffraction phenomenon: plane waves impacting over a perfectly absorbing wall with a hole of size d which is similar than the wavelength λ. In room acoustics simulations, diffraction usually appears since audible range covers a bandwidth that goes from millimeters to decimeters [Beranek (1954)]. Common obstacles such as tables, chair or doors diffract the low frequency bandwidth of sound field, instead of, for example, light phenomenon which frequency range is fourth orders of magnitude bigger than sound frequency range. Therefore, it seems necessary to consider the linearized Euler equations (or the wave equation) for the low frequency bandwidth, since it is the unique manner to reproduce wave phenomena.

Another important phenomenon is the diffusion of sound due to the rugosity of the materials. Since smooth materials scatter incident waves with orientation θ into reflected waves of the same orientation (see Fig. 2.4), diffusive surfaces have the ability to scatter incident sound into non-specular directions. Diffusion is strongly related to the geometry of walls since rugous materials present different surface orientations which are responsible of the non-specular reflexions. These materials are commonly used in scenarios like auditoriums or theatres for improving their acoustics. In Fig. 2.1 (right) we show a sound wave, p_{inc}, impacting on a diffusive wall giving a reflected wave p_{ref}. Observe that the angle of incident θ differs with respect the angle of reflexion $\theta + \varepsilon$ leading to non-specular direction.

As mentioned, the main scope in room acoustics consits on computing the acoustic information, so-called the impulse response, so useful for either predicting or auralizating. Basically, this information is obtained propagating a

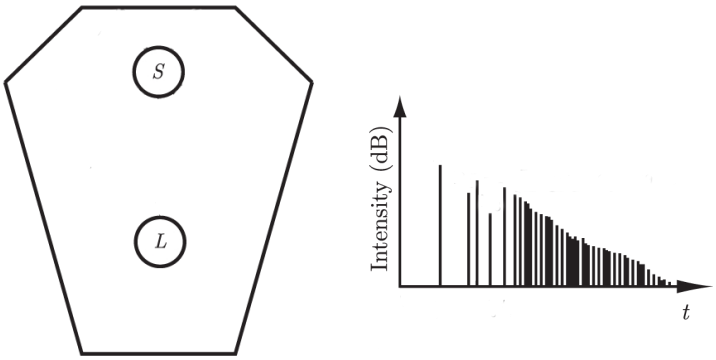

Figure 2.2: (left) A typical room acoustics simulation. S represents the unit impulse signal, the receiver is expressed by L. (right) The impulse response at L due to the sound propagation of the impulse source within the domain Ω.

unit impulse signal through the simulated enclosure. In Sec. 2.3.2, we present the mathematical foundations of the inhomogeneous boundary problem demanded for computing impulse response of enclosures. One peculiarity of this formulation is that the acoustic information obtained with the propagation of unit impulse signals gives the complete information of the acoustic properties of rooms since they have a flat frequency spectrum (i.e. they carry the same amount of energy for each frequency).

For example, one of the common techniques employed to calculate the impulse response in real scenarios consists on recording with microphones the sound produced by a banger since it can be considered as the physics representation of unit impulse source. In Fig. 2.2 (left), it is depicted a common room acoustics situation where the unit impulse signal is located at S and the receiver L is somewhere within the enclosure Ω. In Fig. 2.2 (right) the impulse response for the acoustic intensity in dBs (i.e $||p||^2$) derived from this situation is shown. Observe that the listener perceives different picks distributed along the time axis which intensity decays to 0 for long enough times.

The acoustic response can be splitted in three different regions: a) the direct sound (the first peak), b) the early reflections produced by the first rebounds R_1, R_2, R_3, and R_4 and c) the late reverberations which are obtained after the sound has impacted several times on the walls (see Fig. 2.3). These two last regions are due to the boundaries of the enclosure and are those which contain the acoustic features of the room while the direct sound only depends on the distance between the source and the receiver and the absorption of the air.

In order to understand the works developed in this Thesis, it is essential to introduce the mathematical and physical foundations for room acoustics applications. In fact, we present the analytical formulation of the main problems

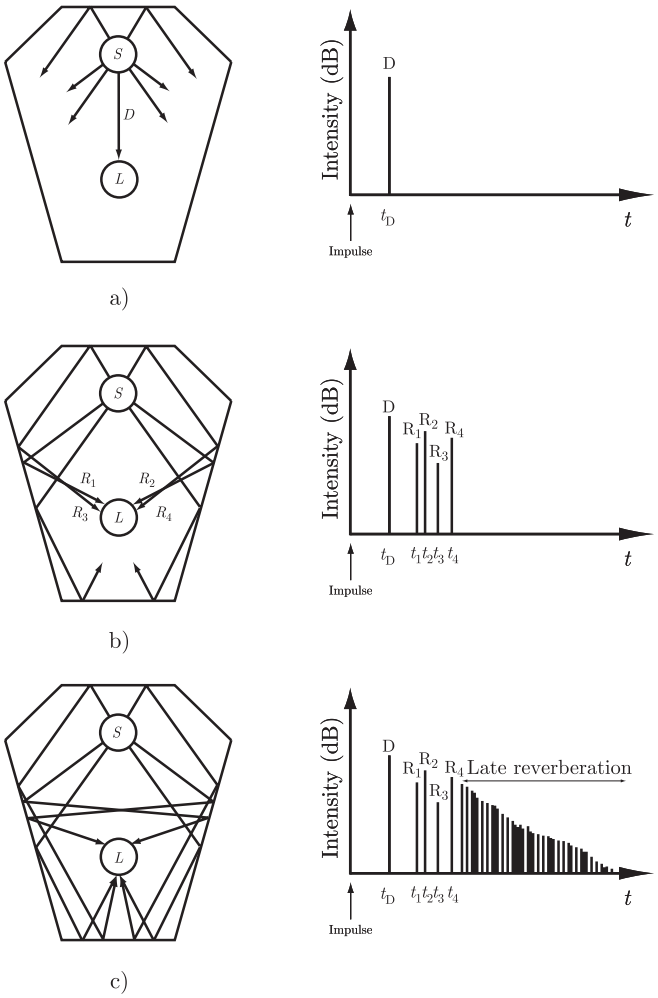

Figure 2.3: An schematic acoustic response splitted in three regions. a) the direct sound D which goes from S to L. b) the early reflections produced by the first rebounds R_1, R_2, R_3, and R_4. c) The late reverberations which are achieved after the sound has impacted several times on the walls.

that involve the acoustic propagation in enclosures, such as rooms, auditoriums or theatres.

Before we discuss the properties of such involved sound fields we shall consider the process which is fundamental for their occurrence: the reflection of a plane sound wave by a single wall or surface. In this context we shall encounter the concepts of wall impedance and absorption coefficient, which

are of special importance in room acoustics.

2.3.1 Impedance Boundary Conditions

Let us consider a plane surface with specific boundary impedance. If a plane wave strikes a plane and uniform wall of infinite extent, in general a part of the sound energy will be reflected from it in the form of a reflected wave originating from the wall, the amplitude and the phase of which differ from those of the incident wave. Both waves interfere with each other and form a 'standing wave', at least partially. The changes in amplitude and phase which take place during the reflection of a wave are expressed by the complex reflection factor

$$R = ||R||e^{(\iota\xi)} \tag{2.39}$$

which is a property of the wall. Its absolute value as well as its phase angle depend on the frequency and on the direction of the incident wave. According to (2.39), the intensity of a plane wave is proportional to the square of the pressure amplitude. Therefore, the intensity of the reflected wave is smaller by a factor $||R||^2$ than that of the incident wave and the fraction $1-||R||^2$ of the incident energy is lost during reflection. This quantity is called the 'absorption coefficient' of the wall:

$$\alpha = 1 - ||R||^2 \tag{2.40}$$

For a wall with zero reflectivity ($R = 0$) the absorption coefficient has its maximum value 1. The wall is said to be totally absorbent or sometimes 'matched to the sound field'. If $R = 1$ (in-phase reflection, $\xi = 0$), the wall is 'rigid' or 'hard'; in the case of $R = -1$ (phase reversal, $\xi = \pi$), we speak of a 'soft' wall. In both cases there is no sound absorption ($\alpha = 0$). The latter case, however, very rarely occurs in room acoustics and only in limited frequency ranges. The acoustical properties of a wall surface, as far as they are of interest in room acoustics, are completely described by the reflection factor for all angles of incidence and for all frequencies.

A specific boundary impedance Z is defined as the ratio of complex amplitude and the normal component of the associated particle velocity $\mathbf{v}$, for a given plane wave. In the particular case of a plane wave travelling in the air, the specific acoustic impedance of that medium is $Z_{\text{air}} = \rho c$, where ρ is the air density and c is the speed of sound.

In general, this impedance presents a particular response depending on the shape of the incident wave. However, there are cases where the material is able to dissipate energy efficiently, i.e. porous sound absorbing materials [Beranek (1940)], or where only reflection phenomenon exists, i.e. ground surfaces [Embleton et al. (1976)]. In these scenarios it is reasonable to assume that there is a *local* linear relation between the normal component of particle velocity and the pressure at a particular point of the surface. Therefore, in many practical situations, a material surface may be characterized in terms of a unique specific boundary impedance. Although real scenarios would consider a frequency

dependent impedance, this Thesis is only focused on constant, or frequency independent, impedances.

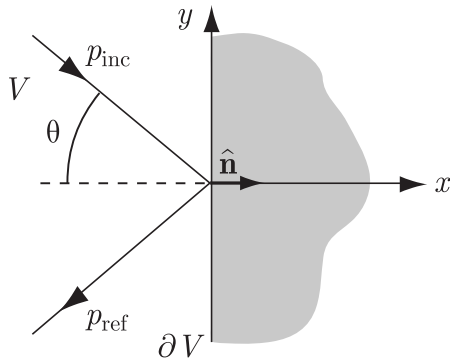

Figure 2.4: Reflection from a plane surface, ∂V, in a two dimensional domain V. $\hat{\mathbf{n}}$ is the normal vector associated to the boundary.

To be more concrete let us define a two dimensional domain V. The acoustic pressure within the region is governed by the wave equation, except for those positions, $\mathbf{y}$, which are located at the boundary, ∂V (see figure 2.4). The time-domain relation between the acoustic pressure and velocity at ∂V is given by

$$p(x,y,t) = Z\mathbf{v}(\mathbf{x},t)\cdot\hat{\mathbf{n}}\,, \tag{2.41}$$

where $\hat{\mathbf{n}}$ is the normalized outward normal vector of the boundary [Kutruff (2000)], and Z is a real positive constant. If a plane wave which is travelling toward a locally reacting impedance surface strikes over it with an incident angle θ, a ratio between the reflected and the incident pressure, p_{ref} and p_{inc} respectively, is defined. This ratio is known as reflection factor R and it is related to the local reacting impedance Z through [Morse & Ingard (1986)]:

$$R(\theta) = \frac{Z\cos\theta - \rho c}{Z\cos\theta + \rho c}\,, \tag{2.42}$$

where θ is the angle represented in figure 2.4. Furthermore, it is assumed that $\mathbf{v}(\mathbf{x},t)$ fulfils the linear conservation mass equation,

$$\frac{\partial\mathbf{v}(\mathbf{x},t)\cdot\hat{\mathbf{n}}}{\partial t} = -\frac{1}{\rho}(\nabla\cdot\hat{\mathbf{n}})p(\mathbf{x},t)\,. \tag{2.43}$$

where ρ represents the air density and $\vec{\nabla}$ is the gradient vector in Cartesian coordinates projected to the outward direction. Although either the Euler equations or the wave equation can be used to represent sound propagation no matter which, the choice leads to different formulations of the BCs. For example, if

the Euler equations are used, the impedance boundary conditions is derived straightforwardly from Eqs. (2.41) and (2.43). Conversely, if the wave equation is demanded, it is necessary to introduce some modifications to (2.41) and (2.43) since this PDE only computes the acoustic pressure. Letting Eq. (2.41) be introduced into the linear conservation mass equation, Eq. (2.43), a BCs expression for the wave equation is obtained reading as follows:

$$\frac{\partial p(\mathbf{x},t)}{\partial t} = -\frac{Z}{\rho}(\nabla \cdot \hat{\mathbf{n}}) p(\mathbf{x},t) \, . \tag{2.44}$$

Observe that Eq. (2.44) only depends on the pressure instead of Eq. (2.43) which relates the acoustic pressure and the normal component of the velocity.

2.3.2 Impulse Response: Mathematical Formulation

In real acoustic systems there exist sound sources (pressure or velocity sources), as we saw, the source generation can be expressed as

$$\frac{\partial^2 p(\mathbf{x},t)}{\partial t^2} - c^2 \Delta p(\mathbf{x},t) = s(\mathbf{x},t) \quad . \tag{2.45}$$

Therefore, if Eq. (2.45) is solved with the appropriate boundary conditions, we would get the propagation information of a sound source defined by $s(\mathbf{x},t)$. It is worth emphasizing that the solution of Eq. (2.45) gives only information of the propagation of the specific source $s(\mathbf{x},t)$. Every time the sound source is changed, one should solve Eq. (2.45) to obtain the acoustic information of the new source. Hence, it is necessary to find the acoustic properties of any room independently of the sound source. This information known as the room acoustic response is obtained studying the propagation of an unit impulse sound source.

One property derived from the Fourier analysis is that delta function has a flat frequency spectrum of Energy. It means that if a Dirac delta function is used as a sound source, $s(t)$, the solution of the inhomogeneous wave equation would give the acoustic information of the closed domain independently of the radiation emitted by the source. Conversely, the most important drawback in the computation of an acoustic response is the generation of the unit impulse signal. More concretely, In numerical methods, the Dirac delta function needs to be approximated since its singularity makes the simulations unstable. In chapter 5, several proposals of unit impulse signal are presented and studied carefully.

The mathematical formulation of this problem is solved by using Green's theory. In this context, we are able to construct an integral equation which combines the effect of sources, propagation, boundary conditions and initial conditions in a simple formula [Barton (1989)]. Let us introduce some basic background in order to understand this method.

We define Green's function,

$$g(\mathbf{x}-\mathbf{x}', t-\tau) = g(\mathbf{x},t|\mathbf{x}',\tau) \ , \tag{2.46}$$

as the impulse response of the PDE,

$$\frac{1}{c^2}\frac{\partial^2 g(\mathbf{x},t|\mathbf{x}',\tau)}{\partial t^2} - \Delta g(\mathbf{x},t|\mathbf{x}',\tau) = \delta(\mathbf{x}-\mathbf{x}')\delta(t-\tau) \ , \tag{2.47}$$

where the product of delta functions: $\delta(\mathbf{x}-\mathbf{x}')\delta(t-\tau)$ represents an impulse of sound pressure. The index $\mathbf{x}=(x,y,z)$ represents the position of the source and $\mathbf{x}'=(x',y',z')$ is the location of the receiver. The definition of $g(\mathbf{x},t|\mathbf{x}',t')$ is further completed by specifying suitable boundary conditions for $\partial\Omega$. Moreover, one usually assumes a causality condition that there is no field other than the one due to δ-source:

$$g(\mathbf{x},t|\mathbf{x}',\tau)=0 \qquad \text{and} \qquad \frac{\partial}{\partial t}g(\mathbf{x},t|\mathbf{x}',\tau)=0 \ , \tag{2.48}$$

for $t<\tau$. It means that the solution of Eq. (2.47) gives information of the unit impulse propagation that carries the same amount of energy at each frequency.

If Eq. (2.45) is multiplied by $g(\mathbf{x},t|\mathbf{x}',t')$ and Eq. (2.47) is multiplied by $p(\mathbf{x},t)$. Then both equations are subtracted and integrated over the domain Ω and τ, obtaining a general expression for the acoustic pressure that reads:

$$\begin{aligned} p(\mathbf{x},t) &= \int_{t_0}^{t}\int_{\Omega} s(\mathbf{x}',\tau)g(\mathbf{x},t|\mathbf{x}',\tau)d\Omega d\tau \\ &- c^2\int_{t_0}^{t}\int_{\delta\Omega}\left[s(\mathbf{x}',\tau)\frac{\partial g(\mathbf{x},t|\mathbf{x}',\tau)}{\partial x_i'} - g(\mathbf{x},t|\mathbf{x}',\tau)\frac{\partial s(\mathbf{x}',\tau)}{\partial x_i'}\right] n d\Omega d\tau \\ &- \left[\int_{\Omega}\left(s(\mathbf{x}',\tau)\frac{\partial g(\mathbf{x},t|\mathbf{x}',\tau)}{\partial \tau} - g(\mathbf{x},t|\mathbf{x}',\tau)\frac{\partial s(\mathbf{x}',\tau)}{\partial \tau}\right)d\Omega\right]_{\tau=t_0} . \end{aligned} \tag{2.49}$$

The first integral represents the effects of the source, the second one is referred to the effects of the boundaries and the third one represents the effects of the initial condition at $\tau=\tau_0$. When the boundary conditions defining the Green's function coincide with those of the physical problem considered the Green's function is called tailored Green's function. For tailored Green's functions the second vanishes to zero and when $\tau=-\infty$, we have the superposition principle over elementary sources which we expect intuitively [Barton (1989)]:

$$p(\mathbf{x},t)=\int_{t_0}^{t}\int_{\Omega} s(\mathbf{x}',\tau)g(\mathbf{x},t|\mathbf{x}',\tau)d\Omega d\tau \quad . \tag{2.50}$$

Note that Green's function gives information of the enclosure, independently of the source. In acoustics, the Green's function is called the acoustic response of the room and it is the main objective in the study of room acoustics.

2.3.3 The Fourier Transform

As it is well-known, it is possible to express any periodic function $p(t)$ as a linear combination of harmonic waves. This combination is called Fourier Series,

mathematically expressed as

$$p(t) = \Re\left[\sum_{n=-\infty}^{+\infty} P(\omega_n) e^{-\imath \omega_n t}\right], \tag{2.51}$$

where $\omega_n = 2\pi n/T$. Therefore, it implies that any function is obtained weighting the harmonics related sinusoidal functions. The coefficients p_n are achieved multiplying Eq. (2.51) by $e^{\imath \omega_n t}$ and integrating over the time interval, T, obtaining

$$P(\omega_n) = \int_{t=0}^{T} p(\tau) e^{-\imath \omega_n \tau} d\tau \,. \tag{2.52}$$

So far, we have only considered periodic functions; nevertheless, non-periodic functions can be achieved assuming an infinite period. In this case, basic functions (complex exponential functions) are not harmonically related, but also all frequencies appear. Let us define the continuous Fourier transform as follows

$$\mathscr{F}[p(t)] = P(\omega) = \int_{-\infty}^{+\infty} p(t) e^{\imath \omega t} dt \,, \tag{2.53}$$

where, for a given angular frequency $\omega = \omega_0$, the complex value $P(\omega_0)$ indicates the complex amplitude of the corresponding complex sinusoidal function, Eq (2.26). The linear operator $\mathscr{F}[\cdot]$ is used as a definition of the Fourier transform. Similarly, it also defined the inverse Fourier Transform as

$$\mathscr{F}^{-1}[P(\omega)] = p(t) = \frac{1}{2\pi} \int_{-\infty}^{+\infty} P(\omega) e^{\imath \omega t} d\omega \,, \tag{2.54}$$

where it represents the linear operation which finds the time-domain representation from a frequency domain signal.

The Fourier transform has a set of interesting mathematical properties [Proakis & Manolakis (1998)] and some of them are summarized as follows:

- $\mathscr{F}[af(t) + bg(t)] = aF(\omega) + bG(\omega)$.
- $\mathscr{F}[f(t) \cdot g(t)] = \frac{1}{2\pi} F(\omega) * G(\omega)$.
- $\mathscr{F}[f(t) * g(t)] = F(\omega) \cdot G(\omega)$.
- $\mathscr{F}\left[\frac{\partial p}{\partial t}\right] = -\imath \omega P(\omega)$.

where the operator $*$ denotes the convolution function explained in Sec. 2.3.4 .

2.3.4 A Discrete Formulation for Computational Problems

Many different applications can be developed with the appropriate use of the Green's theory. For example, in room acoustics, once obtained the acoustic response, we can predict how any source would be heard within the domain

approximating the analytical equation (2.50). Commonly, in room acoustics applications we approximate sound sources such as instruments or human voices through spatial punctual source [Kutruff (2000)]. Thus, according to one of the properties of the Dirac delta function, Eq. (2.50) can be simplified as follows

$$p(\mathbf{x},t) = \int_{t_0}^{t} s(\tau) g(\mathbf{x},t|\tau) d\tau \quad . \tag{2.55}$$

We can write Eq. (2.55) in short-hand notation by defining the mathematical operation $*$ as the convolution of two functions

$$p(\mathbf{x},t) = s(t) * g(\mathbf{x},t) \quad . \tag{2.56}$$

As we presented in Sec. 2.3.3, one of the properties of the Fourier Transform is that converts the convolution into a linear product. Therefore, Eq. (2.55) can be expressed in the frequency domain as follows,

$$p(\mathbf{x},\omega) = S(\omega) G(\mathbf{x},\omega) \quad . \tag{2.57}$$

It is worth mentioning that room acoustics simulations need to discretise the required domain since they are based on different computational techniques. The use of computers for predicting the acoustic features of rooms forces to discretize the solutions in space and time.

Consider that $\Delta t = t_{\text{tot}}/T$ is used as the cell size where t_{tot} is the total time of the simulations and T is the number of temporal grid points. The physical quantities $s(t)$ and $g(\mathbf{x},t|\tau)$ are discretized through the discrete variables (i,j,k) and $(n|l)$ that represent the spatial and temporal steps. Hence, $s(t)$ and $g(x,y,z,t)$ transform to the discrete space as

$$s(t) = s(n\Delta t) = s|^n \,, \tag{2.58}$$

$$g(\mathbf{x},t|\tau) = g|^{n-l}_{i,j,k} \,, \tag{2.59}$$

note that subindex and superindex refer to spatial and temporal coordinates, respectively. The discrete representation of the convolution, which is needed for obtaining the acoustic pressure distribution due to punctual sound source propagation, is defined as

$$p|^n_{i,j,k} = \sum_{l=0}^{T} s|^l g|^{n-l}_{i,j,k} \,. \tag{2.60}$$

Observe the analogy between equations (2.55) and (2.60), since they represent the continuous and discrete formulation of the convolution.

At this point, we need to redefine the Fourier transform of a periodic function, Eq. (2.52), in order to convert the convolution into a linear operation. Let us assume that $s|^n$ is a periodic function of period T. The discrete Fourier

transform of the sequence $\{s|^1,...,s|^T|\}$ is the new sequence $\{S|^1,...,S|^{\omega_T}\}$ which is defined by

$$\mathscr{F}(s|^{:}) = S|^k = \sum_{n=1}^{T} s|^n e^{-\imath\omega_k n\Delta t} \qquad \text{for} \quad 1 \leq n \leq T \quad , \tag{2.61}$$

where the : symbol denotes all x-coordinates. Conversely, it can be defined the discrete inverse Fourier Transform which explicit form is

$$\mathscr{F}^{-1}(S|^{:}) = s|^n = \frac{1}{T}\sum_{k=1}^{\omega_T} S|^k e^{\imath\omega_k n\Delta t} \qquad \text{for} \quad 1 \leq k \leq \omega_T \quad , \tag{2.62}$$

note that both transformations fulfill the properties presented in Sec. 2.3.3.

Finally, as for the continuum case, we can convert the convolution into a simple product applying the Fourier transform to s and g obtaining the the resulting frequency equation,

$$P|^l_{i,j,k} = S|^l G|^l_{i,j,k} \quad . \tag{2.63}$$

Once again, we transform the convolution operation following the properties of the Fourier transform.

2.4 Conclusions

In this chapter, some of the mathematical and physical concepts regarding the sound phenomenon have been presented. More concretely, we presented the basic expressions commonly used in room acoustics. As has been previously mentioned, an inhomogeneous boundary value problem is the starting point to predict and analyze a particular sound field in an enclosure. However, with the exception of some particular (and very simple) cases, these inhomogeneous boundary value problems are unsolvable analytically. For that reason, the room acoustic prediction requires obtaining an approximation of the sound field through several physical simplifications and to define computer algorithms for solving the problem in a reasonable computing time [Schroeder (1973)]. Depending on what possible simplifications are carried out, some of the different room acoustic simulation techniques arises.

Chapter 3

Room Acoustics Simulation Techniques

3.1 Introduction

In this chapter, some of the main computer simulation techniques for room acoustic simulation are revisited, with particular emphasis on the ability to incorporate source modelling and boundary conditions. Room acoustics simulations techniques are usually divided in two groups: the geometrical and the wave-based methods. In turn, Wave-based methods are also subdivided in two large groups: the frequency and time domain methods (the latter, also known as *discrete-time modelling or methods*). Savioja [Savioja (1999)] also included statistical methods, but since they do not model the temporal behaviour of the sound field, they are far from the aim of this thesis.

It is the purpose of this chapter not to provide a deep overview of the current state-of-the-art in room acoustic modelling, but also to give some of the advantages and disadvantages of the most representative techniques, with the aim of justifying the use of the discrete-time methods.

The current chapter is organised as follows: Sec. 3.2 presents some of the most important geometrical methods, focused on a brief overview of the ray-tracing and image-source method. The next two sections deal with wave-based methods. The first one concerns frequency-based wave methods with a generic sight over the two most used methods for room acoustic simulation: finite and boundary element methods. In section 3.4, as this thesis is mainly focused on time-based wave methods (or discrete-time methods), a deeper overview of the state-of-the-art is introduced. Finally, we present the motivations for giving efforts to formulate the Pseudo-Spectral Time-Domain methods for room acoustic simulations.

3.2 Geometrical Methods

Geometrical acoustic simulations make the assumption that sound wavelengths are significantly smaller than the size of the objects in the scene. Hence, the starting point of these methods consists on assuming that sound propagates as a ray. This simplification can considerably improve the computational cost since a PDE problem is directly transformed into an algebraic and/or geometric problem. Therefore, these algorithms currently provide the most practical and accurate method for modelling the early part of an impulse response for high frequency sounds. Nevertheless, sound propagation phenomena at low frequencies, such as diffraction, are not considered under these assumptions. Hence, one important drawback of these methods is the inability to include phenomena such as interference, diffusion and diffraction, since they appear when wavelengths are similar to the size of obstacles.

On the other hand, the implementation of realistic boundary conditions is obtained assuming specular or diffusive reflections, see Sec. 2.3. It could also include the absorption issue in a frequency-dependent manner according to the impedance/absorbing factor of the wall (see Sec. 2.3.1).

Two main algorithms have emerged from the geometrical method's assumptions: the ray-tracing and the image-source method. From this moment on, many variations of these methods have been formulated in order to improve their computational cost, flexibility or to include some of the sound propagation properties properties, such as diffraction and diffusion [Cox et al. (2006)]. Although being far from the scope of this thesis, it is worth mentioning that recently a unified integral equation generalising those methods in an unique formulation has been proposed [Siltanen et al. (2007)]. In the next subsections, these algorithms are overviewed.

3.2.1 Ray-Tracing Method

The ray-tracing method (RTM) is a general technique from geometrical optics that arises from optical physics [Lipson et al. (1995)], with important applications in the computer graphics field [Whitted (1980); Glassner (1989)] and communications [McJown & Hamilton (1991); Cátedra et al. (1998); Coleman (1998); Ji et al. (2001)]. The first attempt to use the RTM for room acoustic simulation was presented by Krokstad et al [Krokstad et al. (1968)].

Basically, these methods find propagation paths between a source and a receiver by generating rays emitted from the source position and following their trajectories through the enclosure until the rays have reached the receiver. Therefore, the delays and attenuation of direct sound and early reflections are straightforwardly computed.

As mentioned above, the initial tendency of this algorithm is to consider only specular reflections, where in each incidence, the incident ray is absorbed by the impedance wall, and reflected with the same angle of incidence [Kulowski (1985)]. Thus, it could be considered that ray-tracing allows simulation of locally

reacting impedances (see in Sec. 2.3.1). However, several improvements of the algorithm have included diffusive surfaces [Lam (1996); Embrechts (2000)] and edge diffraction [Svensson et al. (1999)].

Moreover, RTM applies the Monte Carlo simulation technique to sample these reflection paths leading to statistical results [Halton (1970)]. Monte Carlo path tracing methods consider randomly generated paths from the source to the receiver. In the basic algorithm, sound rays emitted by the sound source are reflected at the surfaces according to certain rules. A specular reflection is the most common reflection rule. By this technique higher order reflections can be searched for, though there are no guarantees that all the paths will be found.

Conversely, the way sound rays are emitted can be either randomised or predefined as a function of the directional properties of the source [Savioja (1999)]. Therefore, it must be ensured that their generation is almost uniform on the surface of a spherical source [Farina (1995)]. The simple assumption of three random generators for the three components of the vector direction of the ray is not completely correct, as that produces a "cube of rays" instead of a sphere. It is possible to cut away the corners of the cube, discarding each vector with a modulus greater than one [Farina (1995)]. If each ray is weighted by an angle dependent function, it is possible to include directivity properties to the source with no increase of computational cost.

The listener positions cannot be considered as a point, since an infinitely small point cannot detect an infinite small ray. For this reason, listeners are typically modelled as volumetric objects, like spheres or cubes, but the listener may also be planar. In practice, a sphere is in most cases the best choice, as it provides an omnidirectional sensitivity pattern and it is easy to implement.

A primary advantage of these methods is their simplicity. They depend only on ray-surface intersection calculations, which are relatively easy to implement and have computational complexity that grows sub linearly with the number of surfaces in the model. Another advantage is generality. As each ray-surface intersection is found, path of specular reflections, diffuse reflection, diffraction and rarefactions can be sampled, thereby modelling arbitrary types of indirect reverberation.

Some examples of its application and comparison with measurements can be found in [Hodgson (1989); Tsingos et al. (2002)]. A software example of the use of the ray-tracing method is CATT-Acoustic [1]. CATT is an acronym for Computer Aided Theater lighting and decor CAD programs were the first CATT product in 1986. Since 1988, however, CATT has concentrated on software for acoustic prediction/auralization (CATT-Acoustic) and more recently, frequency impulse response reverberation tools (The FIReverb Suite).

[1] URL: http://www.catt.se.

3.2.2 Image-Source Method

The image source method (ISM) is one of the most common ray-based modelling method. The concept of image sources has been applied to various field problems in electromagnetic [Balanis (1997)] and acoustic wave propagation, [Allen & Berkley (1979)] extended to arbitrary geometries with plane walls [Borish (1984)].

The concept is based on the principle that a specular reflection can be represented as a sound source (outside the physical boundary) that radiates in free space. It computes specular reflections paths by considering virtual sources generated by mirroring the location of the audio source, over each boundary surface of the environment.

The primary advantage of image source methods is their robustness. They guarantee that all specular paths up to a given order are found. Moreover, the listener can be modelled as a punctual source inspite of Ray-Tracing that must create volumetric listeners.

However, ISM models only specular reflections, their computational complexity grows exponentially with the number of reflections. Thus, an important goal is to try to reduce this complexity. One possible solution is derived from the formulation of the beam tracing methods. These methods have evolved from the ray tracing. As in the ray tracing, a number of rays are emitted from the source, but now these rays are treated as beams. Briefly, for each beam, polygons in the environment are considered for intersection of the beam in front-to-back visibility order. As intersecting polygons are detected, the original beam is clipped to remove the shadow region, a reflection beam is constructed matching the shadow region by mirroring the transmission beam over the polygon's beam[Funkhouser et al. (1998)]. As compared to ISM, the advantage of beam tracing is that fewer virtual sources must be considered for environments of arbitrary geometries [Rindel (1995)].

This method has been implemented in commercial softwares such as CARA (Computer Aided Room Acoustics) [2].

3.2.3 Hybrid and Alternative Geometrical Methods

A possible improvement of those models is to create hybrid models. These methods combine the image source method and ray tracing. The hybrid methods are based on an arrangement where the first reflections are computed with image sources whereas the late reflections are handled by the ray tracing. Such an approach guarantees that the accuracy of the image source method is exploited for early part of a response whereas at the same time exponential growth of the number of image source is avoided.

An example of this method is the ODEON software [3] [Naylor (1993)], initially developed in the Technical University of Denmark. The first version of ODEON

[2] URL: http://www.cara.de.
[3] URL: http://www.odeon.dk

program was targeted at solving acoustic problems in concert and opera halls, today versions are available which allow prediction of auditorium acoustics as well as the acoustics in industrial environments. These software solutions can only be used for large and single enclosures due to the fact that they use geometric-based algorithms for acoustic rendering.

Due to the highly elevated computational cost and other implementation problems of these geometrical methods, an increasing number of alternative methods have appeared in the last years, being more or less inspired by the previous ones. However, it should be mentioned that all of them share the same problematic regarding to the low frequencies approaches as in RTM and ISM. Some of the most important methods are commented in this section.

An alternative method is the well-known beam tracing method [Funkhouser et al. (2004)]. It arises as an improvement to the ray tracing, since rays have no thickness, and it uses beams. Beams are shaped like unbounded pyramids and each beam represents an infinite number of potential ray paths emanating from the source location. It does not suffer from the sampling artifacts of ray tracing [Lehnert (1993)], nor the overlap problems of cone tracing [Vian & van Maercke (1986)]. Another alternative is the pyramid tracing, suited to room acoustics and outdoor calculations [Farina (1995)]. The main advantage of Pyramid Tracing over other diverging beam tracers is the fact that pyramids perfectly cover the surface of a spherical source, while cones cause overlapping or uncovered zones. This method has been produced the first publicly available software for acoustical simulations based on this method, RAMSETE [4]

For a long time, computer graphics, heat and light radiation have used radiosity methods for their simulations. Applications of this method for room acoustics have been described in several contributions [Dalenbäck (1996); Hodgson & Nosal (1996); Nosal et al. (2004)]. The radiosity methods are based on geometrical room acoustics. More concretely, the radiosity method is closely related to ray tracing. However, at some points, radiosity differs from conventional ray-based methods and can be classified to another category. For example, instead of launching a large number of rays and letting them sample boundary surfaces, the radiosity method divides boundaries into smaller elements. After this subdivision the rays are sent between these predefined surface elements. Contribution strengths, which are called form factors, are computed for each element-to-element combination. This method is based on the assumption of Lambertian diffuse surface. This assumption introduces diffusion in the simulated walls.

Finally, acoustic sonel mapping [Kapralos (2006)] is an application of the photon mapping algorithm used in computer graphics for room acoustic simulation. Acoustic sonel mapping is a two-pass particle-based, probabilistic global method developed in order to determine the sound field at any point in a scenario. In the first pass, “sonel” (the analogue to photons, the basic quantity of light, when considering the visual photon mapping method) are emitted

[4] URL: http://www.ramsete.com.

from each sound source and traced through the scene until they interact with a surface. When sonel encounter a diffuse surface, they are stored in a structure called a sonel map. In the second stage, the scene is rendered using the information provided by the previously collected sonel map to provide a quick estimate of the diffuse reflected sound field. A distribution of ray tracing is employed to model specular effects. Sonel mapping is independent of the scene geometry, thereby allowing for the sound field simulation of arbitrary complex scenes to be computed. In addition, it can handle complex interactions between sound and a surface, including pure specular, pure diffuse and glossy reflections and any combination of them.

3.3 Wave Methods in the Frequency Domain

Finite Element Method (FEM) and Boundary Element Method (BEM) are two of the most important frequency-domain wave-based algorithms. These methods have been successfully applied to different areas such as structural mechanics [Courant (1943); Dominguez (1993)] and electromagnetism [Jin (2002); Chen & Zhou (1992)]. In the acoustic literature, there are several applications of both methods focused on the analysis of resonance of acoustic systems [Ihlenburg (1998); Wrobel & Aliabadi (2002)]. Basically, in these algorithms the frequency range is discretized, in order to give results of the steady-state sound pressure distribution.

These algorithms are not appropriate for room acoustic simulation since the solutions are achieved in the frequency range. Moreover, the use of FEM or BEM in room acoustics problems is so far limited to a frequency range that is considerably smaller than the range used for room acoustical purposes. The limiting factor for these methods is the required discretization of the volume or surface in elements of a size small enough to reconstruct the wave in magnitude and phase at every point of the discretization domain.Nevertheless, using these techniques, the eigenvalue analysis of enclosures can be calculate leading to remarkable accuracies.

3.3.1 Finite Element Method

In the room acoustics field, several analysis of rectangular rooms through FEM have been provided by Wright [Wright (1995)] and Savioja et al. [Savioja et al. (1996a)]. On the other hand, more realistic rooms have recently been analyzed giving a fair agreement among simulation and measurements in small [Pietrzyk & Kleiner (1997)] and large [Ahnert et al. (2006)] rooms.

The main advantage of FEM lies in the flexibility of handling problems with complex geometries and inhomogeneous media. This flexibility appears owing to the fact that it can be implemented through non-uniform meshes. Therefore, the systematic generality of the method leads to build proper computer programs. The basic formulation of FEM assumes a general solution in the whole simulated domain. The PDE system is derived for a typical element and then, it

is assembled for all elements of the domain using a set of basis functions. Each of these elements only interacts with the elements directly adjacent to it and these basis usually conform a tessellation of the whole space. This representation by elements creates matrices that are large but sparsely filled [Taflove (1995)].

The most important drawback of FEM is that the computation of the acoustic field is achieved in the frequency range. Therefore, it implies that we would need to carry out a different simulation for each frequency since the acoustic properties depends strongly on this value, increasing considerably the computational cost of the algorithms. Moreover, due to stability reasons, FEM takes an extremely small element size for modelling in the entire frequency bandwidth. Over seven elements per wavelength are required as sufficient sampling rate [van der Geest & McChulloch (1998); Murphy (2000)]. For example, if an element is 0.5 m long, with $c = 343ms^{-1}$, the maximum frequency that can be calculated with any reasonable accuracy is approximately 114 Hz. In a 3-D simulation, doubling the frequency the number of elements are multiplied by eight [Murphy (2000)].

3.3.2 Boundary Element Method

In the room acoustics literature some contributions of BEM methods have been applied for the analysis of large hall effects [Bai (1992); Osa et al. (2006)].

Since FEM is fairly a very computational expensive method, BEM arises as an alternative method which considerably reduces the computational cost of the problem. In these methods, only boundaries are discretized, more concretely, they are divided into surface elements which are typically smaller than approximately $1/8$ of the characteristic wavelength.

The methodology of BEM methods consists on fitting boundary values into Kirchoff-Helmholtz integral formulation. What we obtain is an integral equation that can then be used again to calculate numerically the solution directly at any desired point in the interior of the solution domain. It allows a simple and accurate modelling of problems involving infinite and semi-infinite domains. The matrix implementation of the method gives a full matrix, i.e. every element of the matrix is non-zero [Kirkup (1998)].

3.4 Wave Methods in the Time Domain

Until now, we reviewed different methods employed for computing a room impulse response. Depending on the physics treatment of sound, we can split the room acoustics methods into three different groups. On the one hand, geometrical methods provide simple and accurate algorithms which are valid only for high frequencies; on the other hand, wave methods solve numerically the wave equations, giving more accurate results than geometrical methods in the low frequency range since the wave equations model all sound propagation

phenomena, except air absorption. For example, the frequency-domain wave-based methods based on the wave equation analyse the steady-state of a room leading to high accuracies in their results. Conversely, one important drawback of these methods is the impossibility of being formulate in transitory analysis (i.e. in the time domain). For this reason, the wave-based in the time domain is an appropriate alternative methods, since they are based on physic foundations of sound propagation leading fairly goor accuracies in the low frequency bandwidth; furthermore, the mesh generation of the simulated domains is simpler to define than FEM or BEM, since a constantly regular mesh of polyhedron (in a 3D simulation) is demanded for their implementation. The flexibility and simpler conceptually such as geometrical methods, but with a higher accuracy at low frequencies, is a main aim for room acoustic simulations.

3.4.1 Finite Difference Methods

All these methods lie on a common assumption: the mathematical expressions of sound propagation are discretised not only in space, but also in time, giving a recursive algebraic expression which is updated in each time step for every grid point of the mesh. More specifically, two time-domain methods have specially arisen for room acoustic applications: the Digital Waveguide Mesh (DWM) and the finite-difference time-domain method (FDTD).

On the one hand, DWM was formulated for the first time in room acoustics applications by Van Dyune and Smith [Duyne & Smith (1993); VanDuyne & Smith (1995)]. Many of the advances on this topic have been inherited as an extension of the membranes and plate, being a 2D problem, to enclosures as a 3D problem [Savioja et al. (1995); Campos (2003)]. The DWM could also be seen as a particular class of finite difference method [Savioja et al. (1999)], with the particularity that it uses a decomposition of the sound pressure waves based on incoming and outgoing components [Duyne & Smith (1993); Campos & Howard (2005)]. This method has a similar formulation to the Transmission Line Matrix (TLM) method [Elmasri et al. (1998); Christopoulos (1995)], although finally it was demonstrated the equivalence between both methods [Johns (1987); Krumpholz et al. (1995); Bilbao (2001)]. On the other hand, the first contributions of FDTD in the room acoustic field were presented in the middle of the nineties by Botteldooren [Botteldooren (1995)] and Savioja [Savioja et al. (1994)] leading to an increasing number of publications and works related in this topic in order to improve the suitability of these methods.

This Thesis is focused on analysing and contributing to time-domain methods, more concretely, the FDTD methods. A review of several propagation algorithms, the implementation of aproppriate boundary conditions and the analysis of different sound source generation are studied with detail since the main objective in room acoustics applications is the computation of acoustic impulse response.

3.5 Pseudo-Spectral Time-Domain Methods

In this chapter, an overview of the modelling techniques for room acoustic simulation has been presented. Since solving directly the particular inhomogeneous boundary value problem which represent the room under analysis is an extremely complex task, simplified models should be used to obtain approximated but accurate solutions.

A proper alternative for computing the impulse acoustic response of a enclosure is the use of wave-based methods in the time domain or discrete-time methods. They are based on approaching partial differential equations that govern the sound wave propagation through time and space discretization, creating a recursive algorithm which provides an acoustic variables distribution in all discretized space positions in every discrete time step. With these methods, impulsive analysis are obtained with an unique recursive algorithm, simplifying considerably the computational cost. The most popular discrete-time methods for room acoustic simulation are FDTD method and the DWM method. Although the efforts of this Thesis are restricted to the FDTD algorithms, both methods have been successfully applied into room acoustics applications.

The advantages of these methods can be found such as the simplicity of the algorithm formulation as the accuracy of the results achieved at low frequency-bandth. Even though it seems that these algorithms are the proper alternative for this type of acoustic problems, There are different negative aspects that, at least, should be commented.

For example, one of the most important drawbacks of FDTD algorithms is that they introduce a non-physical dispersion error due to the spatial discretization of the simulated domain. It means that the numerical speed of sound differs respect the theorical one depending strongly on the orientation of the travelling waves [Taflove (1995); Spa et al. (2009)]. Furthermore, the computational cost of these algorithms is an important limitation since typical scenarios, such as auditoriums or theatres, require either memory resources or computational times which are excessively long to consider these methods suitable for room acoustics applications.

Due to these facts, it seems reasonable to dedicate efforts in improving these negative characteristics derived from their assumptions. More concretely, in this Thesis we present for the first time in room acoustics the formulation of the Fourier Pseudo-Spectral Time-Domain (PSTD) methods which improves either the dispersion error or the computational cost of the algorithms compared with those previously commented. This method is based on the Fourier transform since the spatial derivatives of the PDE system are computed using the spectral derivatives [Fornberg (1996)]. Conversely, as for FDTD methods, the temporal derivatives of the dynamic system are given by finite difference operators. the fact of employing these algorithms leads to less dispersive numerical simulations and reduces the computational cost of the acoustic problems. In this section, neither technical nor mathematical foundations are presented.

The first contribution of Fourier PSTD methods was presented by Liu [Liu

(1997)] for electromagnetism problems and it was further developed for acoustics propagation [Liu (1998)], modelling of piezoelectric transducers [Filoux et al. (2008)] or simulation of photonic devices [Pernice (2008)]. Nevertheless, this method has never been applied to room acoustics applications since the definition of suitable impedance boundary conditions for the characterisation of real walls has not been done yet.

The following chapters are grouped in three different parts (wave propagation, source generation and locally-reacting boundary conditions) according to the main problems that one finds in the computation of an acoustics impulse response. We carefully review the most common formulations of FDTD and PSTD for either the Euler or the wave discretized equations incorporating several formulations of impedance boundary conditions which are properly studied. We should remark that the formulation of numerical boundary conditions for PSTD methods is a novel contribution into room acoustics simulations. We will see during the course of the explanations that PSTD is capable to build appopriate algorithms for room acoustics simulations even improving in some cases the accuracy of the results respect to those obtained with FDTD algorithms.

3.6 Conclusion

In this chapter, we presented an overview of the most common numerical techniques applied to room acoustics. Basically, the numerical methods are divided in two big groups deppending on the considerations used to approximate the the sound phenomenon. On the one hand, the geometrical methods treat the sound propagation as rays travelling through the space. This assumpition allows to build efficient algorithms, since the computational resources required for these algorithms make possible to create real time applications so important in computer graphics. Nevertheless, one important drawback is that phenomena such as diffraction or diffusion, commonly observed in room acoustics, is not obtained, since the unique manner to simulate these phenomena is using the PDE which, in the case of sound propagation, is the wave equation. The most representative ray-based methods are the RT, the beam-tracying and the ISM.

On the other hand, the second group of room acoustics simulations are the wave methods in either the frquency and the time-domain. Both subgroups are based on the PDE that defines the physical problem, in order to obtain computational solutions of the acoustic pressure. Firstly, we presented the wave-methods in the frequency-domain where the most important techniques are the FEM and BEM. Both methods give accurate solutions in the steady-state of the acoustic pressure in the frequency space. The main disadvantage of this methods is that it is needed to carry out one different simulation by each frequency.

For this reason, the wave-based methods in the time-domain have emerged as a proper solution for simulating the sound propagation in the low frequency range. These methods approximate the PDE into a simple set of update equa-

tions that allows to obtain the acoustic propagation in enclosures with only one simulations. In fact, we focus on the analysis of the FDTD and PSTD methods. The first methods have been succesfully applied in room acoustics, whereas the PSTD methods have recently emerged in this area. As titled in this Thesis, we deal with the sound propagation, the source genertion and the locally reacting boundary conditions which are the main problems in these type of simulations. In Chapter 4, we formulate the most important formulations of FDTD and PSTD algorithms. Moreover, we study the accuracy of the methods with numerical experiments. Secondly, we present a complete analysis of the main source generations that exist for FDTD and PSTD methods observing different behavior deppending on the source approximation used in the simulations (see Chapter 5). Finally, in Chapter 6 we overview the most important numerical boundary conditions based on the local impedance concept. Furthermore, we present for the first time in the acoustics, numerical boundary conditions for either the Euler or the wave equation suportted by numerical data of remarkable accuracy.

Chapter 4

Wave Propagation Algorithms

4.1 Introduction

As we explained in Chap. 3, there are different techniques to compute an acoustic response in a virtual environment. We carefully overviewed either the geometrical (see Sec. 3.2) or the wave-based methods in the frequency and in the time domain (see Sec. 3.3 and 3.4, respectively), observing the main features of those methods. All the efforts in this Thesis are focused on the study of the main problems (*wave progation, source generation and locally reacting boundary conditions*) in the computation of an impulse response using the time-domain numerical methods.

In this chapter, we formulate and analyze the main features of the finite-difference in the time-domain (FDTD) (see from Sec. 4.3 to Sec. 4.5), which has been successfully applied in acoustics [Botteldooren (1994),Wagner & Schneider (2005),Maloney & Cummings (1995)] and the new recently emergent Fourier pseudo-spectral time-domain methods (PSTD) [Liu (1997)] which is properly presented in Secs. 4.6 and 4.7. Moreover, in Sec. 4.8, we present a novel numerical analysis of the dispersion error which provides high accuracies even for isotropic algorithms. Finally, we expose the conclusions by giving a comparisson analysis between these methods.

4.2 Problem Overview

The starting point of both methods is the PDEs that govern the dynamical system, which in this case is the sound propagation phenomenon. This phenomenon can be completely described by using the linearized Euler equations, Eqs (2.10)-(2.11), that are explained with detail in Sec. 2.2. Moreover, we observed that the wave equation can be derived straightforwardly from this PDE, leading to an uncoupled differential equation called the wave equation Eq. (2.16).

To numerically solve either the Euler equations or the wave equation, the

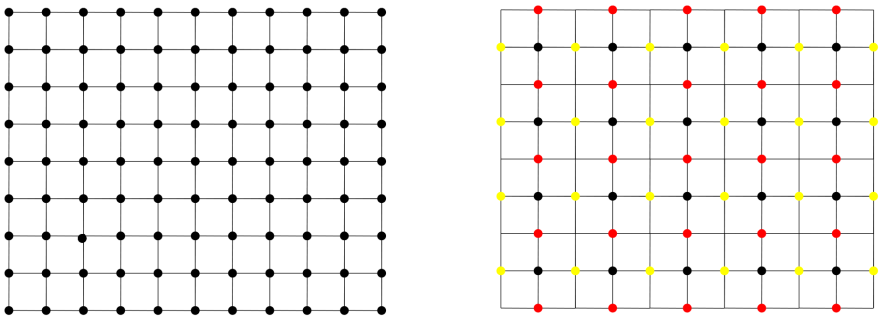

Figure 4.1: (Left) A 2D centered mesh: All the acoustic quantities are computes at each node. (Right) a 2D staggered mesh: the yellow nodes and the red nodes are the x and y component of the velocity respectively and pressure is computed at the black nodes.

space and time of the simulated domain should be discretized. Therefore, the acoustic pressure and velocity components are evaluated at discrete positions and times. In the Eulerian simulations, we have used two different types of meshes: the centered meshes; and the staggered meshes. For the centered meshes, each grid point represents a position in the space where the acoustic pressure and velocity are computed (see Fig. 4.1 (left)). On the other hand, in staggered meshes, there are grid points that have information only of the pressure and others of the velocity. In Fig. 4.1 (right), a 2D staggered mesh is shown. there are three types of grid points (each type with a different color) that represent the three different quantities measured. Yellow and red points carry information about v_x and v_y, respectively, and black dots compute p. Conversely, for the simulations based on the wave equation, centered meshes are required since it is only computed the information of the acoustic pressure.

Once discretized the space and time, the partial derivatives of Eqs. (2.10)-(2.11) and Eq. (2.16) can be easily approximated. In this section we present the basic concepts in FD and Fourier PS methods, in order to understand the formulation of several algorithms discussed in this chapter.

Finite Difference Methods

Finite Differences Methods (FDM) are the most common numerical methods for solving PDE systems. There are many fields where FDM have been successfully applied: Computer Graphics, Electromagnetism, Seismology, Solid State Physics (Elasticity Theory) and also in Meteorologic predictions. In all these fields, FDM have provided very good and useful results. We believe that for new multimedia applications, FDM will play an important role, mostly in the low frequency domain.

The basic idea of FDM is simple: derivatives in differential equations are written in terms of discrete quantities of dependent and independent variables, resulting in simultaneous algebraic equations with all unknowns prescribed at discrete mesh points for the entire domain. To illustrate this, let us consider a generic function $u(x)$ and its derivative at point x:

$$\frac{\partial u(x)}{\partial x} = \lim_{\Delta x \to 0} \frac{u(x+\Delta x) - u(x)}{\Delta x} \quad , \tag{4.1}$$

if $u(x+\Delta x)$ is expanded in Taylor series about $u(x)$ [Hoffman (1992)], we obtain:

$$u(x+\Delta x) = u(x) + \Delta x \frac{\partial u(x)}{\partial x} + \frac{(\Delta x)^2}{2} \frac{\partial^2 u(x)}{\partial x^2} + \frac{(\Delta x)^3}{3!} \frac{\partial^3 u(x)}{\partial x^3} + \ldots \tag{4.2}$$

Substituting Eq. (4.2) in Eq. (4.1):

$$\frac{\partial u(x)}{\partial x} = \lim_{\Delta x \to 0} \left(\frac{\partial u(x)}{\partial x} + \frac{\Delta x}{2} \frac{\partial^2 u(x)}{\partial x^2} + \ldots \right) \quad , \tag{4.3}$$

and from Eq. (4.2) it can be written:

$$\frac{u(x+\Delta x) - u(x)}{\Delta x} = \frac{\partial u(x)}{\partial x} + \frac{\Delta x}{2} \frac{\partial^2 u(x)}{\partial x^2} + \ldots = \frac{\partial u(x)}{\partial x} + \mathcal{O}(\Delta x) \quad . \tag{4.4}$$

The derivative, Eq. (4.4), is of first order in Δx, showing that the truncation error $\mathcal{O}(\Delta x)$ goes to zero with the first power in Δx. This finite difference approximation exposed is just the first order accuracy of finite differences method.

Considering Fig. 4.2, we can relate the value of the function u at the grid points $i+1$ and $i-1$ with the value of u and its derivatives at the grid point i using the Taylor expansion:

$$u_{i+1} = u_i + \Delta x \left(\frac{\partial u}{\partial x} \right)_i + \frac{(\Delta x)^2}{2} \left(\frac{\partial^2 u}{\partial x^2} \right)_i + \frac{(\Delta x)^3}{3!} \left(\frac{\partial^3 u}{\partial x^3} \right)_i + \ldots \tag{4.5}$$

$$u_{i-1} = u_i - \Delta x \left(\frac{\partial u}{\partial x} \right)_i + \frac{(\Delta x)^2}{2} \left(\frac{\partial^2 u}{\partial x^2} \right)_i - \frac{(\Delta x)^3}{3!} \left(\frac{\partial^3 u}{\partial x^3} \right)_i + \ldots \tag{4.6}$$

Rewriting Eq. (4.5), we obtain the forward difference relation (first order in accuracy):

$$\left(\frac{\partial u}{\partial x} \right)_i = \frac{u_{i+1} - u_i}{\Delta x} + \mathcal{O}(\Delta x) \quad . \tag{4.7}$$

It corresponds to number 1 in Fig. 4.2. Likewise, from Eq. (4.6), the backward difference relation (first order in accuracy) is obtained:

$$\left(\frac{\partial u}{\partial x} \right)_i = \frac{u_i - u_{i+1}}{\Delta x} + \mathcal{O}(\Delta x) \quad , \tag{4.8}$$

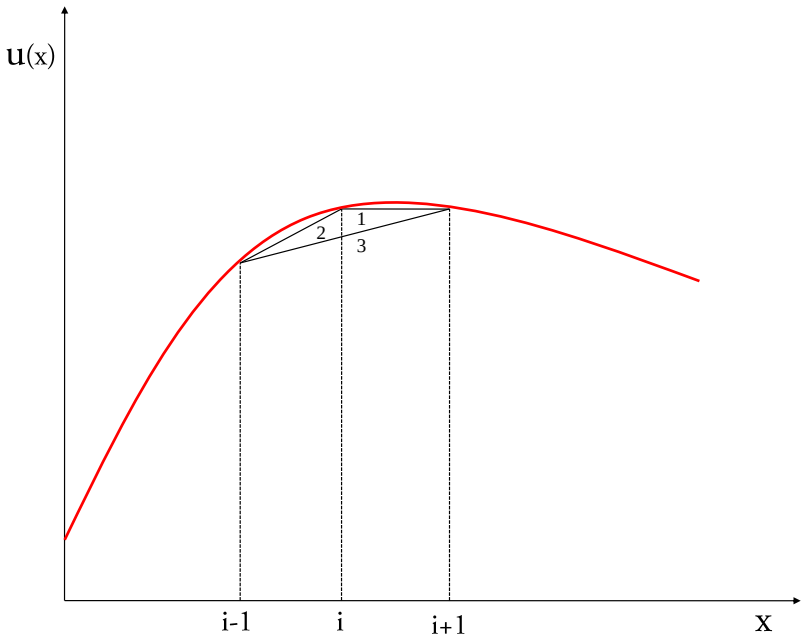

Figure 4.2: Finite difference approximation. 1 represents the forward difference; 2 represents the backward difference; and, finally, 3 represents the central difference.

it corresponds to number 2 in Fig. 4.2. A central difference relation arises from subtracting Eq. (4.6) from Eq. (4.5) (number 3 in Fig. 4.2):

$$\left(\frac{\partial u}{\partial x}\right)_i = \frac{u_{i+1} - u_{i-1}}{2\Delta x} + \mathscr{O}(\Delta x^2) \quad . \tag{4.9}$$

Central difference give a second order of truncation error, instead of forward and backward difference that gives a first order of truncation error. Finally, adding Eqs. (4.5) and (4.6), we obtain:

$$\frac{u_{i+1} - 2u_i + u_{i-1}}{\Delta x^2} = \left(\frac{\partial^2 u}{\partial x^2}\right)_i + \frac{(\Delta x)^2}{12}\left(\frac{\partial^4 u}{\partial x^4}\right)_i + \ldots \tag{4.10}$$

This leads to the finite difference formula for the second derivative with second order accuracy,

$$\left(\frac{\partial^2 u}{\partial x^2}\right)_i = \frac{u_{i+1} - 2u_i + u_{i-1}}{\Delta x^2} + \mathscr{O}(\Delta x^2) \ . \tag{4.11}$$

Fourier Psuedo-Spectral Methods

The difference between the common FDTD methods and the Fourier Pseudo-Spectral Time-Domain methods lies in the treatment of the spatial derivatives which in the case of PSTD are computed by using the discrete Fourier transforms Eqs. (2.61) and (2.62) defined in Sec. 2.3.4. In this case, we apply the Fourier transform over the spatial coordinates, instead of those presented in Sec. 2.3.4 that were computed over the time axis. To illustrate this, let us consider a one dimensional domain of size L and an evolving physical quantity $u(x,t)$. Consider that $\Delta x = L/N_x$ is used as the cell size and N_x is the number of grid points. Then, according to the fourth property of the Fourier transform presented in Sec. 2.3.3, the approximation of the spatial derivative can be written as:

$$\frac{\partial u(x,t)}{\partial x} \approx \mathscr{F}_x^{-1}\left[\imath \frac{2\pi n_x}{N_x \Delta x} \mathscr{F}_x[u\,|_{:}^{n}]\right] \quad , \tag{4.12}$$

where $\mathscr{F}_x$ and $\mathscr{F}_x^{-1}$ denote the Fourier transform over the x-axis and its inverse respectively; n_x is the index of the Fourier transform. More concretely, the spatial derivative at the locations $x = i\Delta x$, $i = 0, 1, ..., N_x - 1$, is given by:

$$\left(\frac{\partial u(x,t)}{\partial x}\right)_{x=i\Delta x} = \frac{1}{L} \sum_{m=-N_x/2}^{N_x/2-1} \imath k_m U|_m^n e^{\imath k_m i \Delta x} \quad , \tag{4.13}$$

where $k_m = 2\pi m/L$, and $U(m)$ is the Fourier series

$$U|_m^n = \Delta x \sum_{i=0}^{N_x-1} u|_i^n e^{-\imath k_m i \Delta x} \quad . \tag{4.14}$$

Interestingly, the discrete Fourier transforms in Eqs. (4.13) and (4.14) can be obtained efficiently by using a FFT algorithm [Cooley & Tukey (1965)], with a number of operations of the order of $(N_x \log_2 N_x)$. It is worth mentioning the fact that from the Nyquist sampling theorem, the derivative in Eq. (4.13) is exact for $\Delta x \leq \lambda/2$ (λ being the wavelength) which implies that even with two cells per wavelength, the PSTD method does not produce phase error due to the spatial discretization. This makes the PSTD method far better than the more common FDTD methods for the numerical study of high-frequency problems or if long-time solutions are needed [Li et al. (2000)].

4.3 The Classical Leap-Frog Scheme

The most important basic formulation of the Yee algorithm [Yee (1966)] applied to acoustics was presented in 1994 [Botteldooren (1994)], and further developed for room acoustics in 1995 [Botteldooren (1995)].

The finite differences in the time domain approximation uses a Cartesian staggered grid as in the original paper by [Yee (1966)] (see Fig. 4.1 (right)) with pressure and particle velocity components as unknown quantities. The acoustic

pressure is located at $\tilde{\mathbf{x}} = (i\Delta x, j\Delta y, k\Delta z)$ at a discrete time $\tilde{t} = n\Delta t$, where Δx, Δy and Δz are the spatial discretization and Δt is the time discretization. The indexes i, j and k mark the positions into the mesh; and finally, the index n refers to the time step. Conversely, the three components of the particle velocity are determined at positions,

$$\begin{aligned} v_x(x,y,z,t) &= v_x\left((i+1/2)\Delta x, j\Delta y, k\Delta z\right) \quad , \\ v_y(x,y,z,t) &= v_y\left(i\Delta x, (j+1/2)\Delta y, k\Delta z\right) \quad , \\ v_z(x,y,z,t) &= v_z\left(i\Delta x, j\Delta y, (k+1/2)\Delta z\right) \quad , \end{aligned} \tag{4.15}$$

at intermediate times $t = (n+1/2)\Delta t$. Once the numerical domain is defined, the derivatives of the Euler equations can be approximated by finite difference techniques. On the one hand, the temporal derivatives of the velocity are approximated with the backward difference (see Eq. (4.6)) and the temporal derivative for the pressure employs the forward difference (see Eq. (4.5)). On the other hand, the spatial derivatives of the velocity and the pressure are also obtained with the backward and the forward difference, respectively. With these assumptions, the FDTD scheme for the Euler equations of acoustics become:

$$\begin{aligned} v_x|^{n+1/2}_{i+1/2,j,k} &= v_x|^{n-1/2}_{i+1/2,j,k} - a_1(p|^n_{i+1,j,k} - p|^n_{i,j,k}) \, , \\ v_y|^{n+1/2}_{i,j+1/2,k} &= v_y|^{n-1/2}_{i,j+1/2,k} - a_1(p|^n_{i,j+1,k} - p|^n_{i,j,k}) \, , \\ v_z|^{n+1/2}_{i,j,k+1/2} &= v_z|^{n-1/2}_{i,j,k+1/2} - a_1(p|^n_{i,j,k+1} - p|^n_{i,j,k}) \, , \\ p|^{n+1}_{i,j,k} = & \quad p|^n_{i,j,k} - a_2(v_x|^{n+1/2}_{i+1/2,j,k} - v_x|^{n+1/2}_{i-1/2,j,k} + v_y|^{n+1/2}_{i,j+1/2,k} - v_y|^{n+1/2}_{i,j-1/2,k} \\ & + \quad v_z|^{n+1/2}_{i,,j,k+1/2} - v_z|^{n+1/2}_{i,j,k-1/2}) \quad , \end{aligned} \tag{4.16}$$

where $a_1 = \frac{\Delta t}{\rho\delta}$ and $a_2 = \rho c^2 \frac{\Delta t}{\delta}$ are the stability constants of our problem. Observe that we have considered (as in the paper by Botteldooren) that $\Delta x = \Delta y = \Delta z = \delta$. Finally, note that this algorithm is second order accuracy in time and space.

One important issue common to all FDTD-based algorithms is that they cause a nonphysical dispersion of the simulated waves [Trefethen (1982)]. This error affects the numerical speed of sound, c_{num}, which is different than the sound velocity, c. The dispersion error can be derived from the standard Von-Neumann analysis [Hoffman (1992)], which assumes numerical planar waves of the form

$$p|^n_{i,j,k} = p_0 e^{\imath(\mathbf{k}\cdot\tilde{\mathbf{x}} - \omega\tilde{t})} \tag{4.17}$$

$$\mathbf{v}|^n_{i,j,k} = \mathbf{v_0} e^{\imath(\mathbf{k}\cdot\tilde{\mathbf{x}} - \omega\tilde{t})} \, , \tag{4.18}$$

where $\mathbf{k}$ is the wave number defined in Sec. 2.2.2. These equations are introduced in the numerical scheme Eq. (4.16) obtaining an homogeneous algebraic

system

$$\underline{\mathscr{M}} \begin{pmatrix} \mathbf{v_0} \\ p_0 \end{pmatrix} = 0 \,, \tag{4.19}$$

that has solution if and only if the determinant of $\underline{\mathscr{M}}$ (i.e. the mass matrix) is equal to 0. It arises an expression which can be written in terms of the Courant stability number, S, the number of cells per wavelength $N_{\lambda=\frac{\lambda}{\delta}}$, and the orientation of the solid angle. In this case, the dispersion relation reads as follows,

$$\begin{aligned} S^{-2}\sin^2\left(\frac{\pi S}{N_\lambda}\right) &= \sin^2\left(\frac{\pi c}{N_\lambda c_{\text{num}}}\cos\theta\sin\phi\right)+\sin^2\left(\frac{\pi c}{N_\lambda c_{\text{num}}}\sin\theta\sin\phi\right) \\ &\quad +\sin^2\left(\frac{\pi c}{N_\lambda c_{\text{num}}}\cos\phi\right) . \end{aligned} \tag{4.20}$$

Note that θ and ϕ are the angles derived from the spherical coordinates. A straightforward analysis of Eq. (4.20) reveals a number of interesting properties: c/c_{num} tends to 1 in the continuum limit ($N_\lambda \to \infty$); the scheme is second order accurate in terms of isotropy;[Wagner & Schneider (2005)] finally, letting $S = \frac{1}{\sqrt{2}}$, which is the maximum value of S for this algorithm to be stable,[Botteldooren (1994)] there is no dispersion error at $\theta = 45^\circ$.

Observe that, for this numerical algorithm, the dispersion relation depends strongly in the frequency and the orientation of the planar waves. It means that c_{num} has a different behavior than c, the real sound velocity, which is isotropic and independent of the frequency. These variations of the numerical sound velocity introduce an inherent error in the computation of any acoustic response, even getting critical for long reverberation times or large enclosures.

Due to the discretization, any numerical algorithm is stable only for certain values of δ and Δt. More concretely, the stability criterium is fixed by the Courant stability number,

$$S = c\frac{\Delta t}{\delta} \leq \frac{1}{\sqrt{D}} \,, \tag{4.21}$$

where D represents the dimension which in this case is 3.

One of the main problems of this algorithm is that it requires staggered meshes for its formulation. In fact, when the geometry of the numerical domain is sufficiently complex, the definition of impedance walls is strongly constrained since they can only be defined at velocity nodes. Therefore, it is important to re-define the staggered leap-frog scheme in order to get a more flexible algorithms in terms of the mesh generation. More concretely, Liu [Liu (1996)] presents a methodology to convert staggered FDTD algorithms into their centered version. These new algorithms keep exactly the same dispersion relation, Eq. (4.20), Courant stability number, (Eq. 4.21), and the accuracy than the staggered ones but, in this case, they are defined by using a centered cubic mesh where the pressure and the velocity components are located at (i, j, k) at a time step n.

More specifically, to obtain the same dispersion and accuracy properties than for the staggered algorithms, it is combined the forward and the backward finite differences leading to the following numerical scheme:

$$\begin{aligned}
v_x|^{n+1}_{i,j,k} &= v_x|^{n}_{i,j,k} - a_1(p|^{n}_{i+1,j,k} - p|^{n}_{i,j,k}) \,, \\
v_y|^{n+1}_{i,j,k} &= v_y|^{n}_{i,j,k} - a_1(p|^{n}_{i,j+1,k} - p|^{n}_{i,j,k}) \,, \\
v_z|^{n+1}_{i,j,k} &= v_z|^{n}_{i,j,k} - a_1(p|^{n}_{i,j,k+1} - p|^{n}_{i,j,k}) \,, \\
p|^{n+1}_{i,j,k} &= p|^{n}_{i,j,k} - a_2\Big(v_x|^{n+1}_{i,j,k} - v_x|^{n+1}_{i-1,j,k} + v_y|^{n+1}_{i,j,k} - v_y|^{n+1}_{i,j-1,k} \\
&+ v_z|^{n+1}_{i,,j,k} - v_z|^{n+1}_{i,j,k-1} \Big) \,. \qquad (4.22)
\end{aligned}$$

It is important to highlight the relevance of this analogous formulation, since it is demanded for the definition of the locally reacting boundary conditions explained in Sec. 6.5.2. Finally, we should note that for room acoustics applications it is more appropriate to create numerical algorithms based on the wave equation since, in the computation of impulse responses, we only need the information of the acoustic pressure. A similar formulation of the finite differences algorithm based on the wave equation is obtained using a centered mesh where the second order space and time derivatives of the PDE are approximated with second order finite derivatives Eq. (4.11) leading to the following scheme

$$\begin{aligned}
p|^{n+1}_{i,j,k} &= 2p|^{n}_{i,j,k} - p|^{n-1}_{i,j,k} - c^2\frac{\Delta^2 t}{\delta^2}\Big(p|^{n}_{i+1,j,k} + p|^{n}_{i-1,j,k} + p|^{n}_{i,j+1,k} + p|^{n}_{i,j-1,k} \\
&+ p|^{n}_{i,j,k+1} + p|^{n}_{i,j,k-1} - 6p^{n}_{i,j,k} \Big) \,. \qquad (4.23)
\end{aligned}$$

Note that this algorithm has exactly the same dispersion relation and Courant stability number than the numerical formulations of the Euler equations presented in both, staggered and centered meshes.

4.4 A Parametric FDTD Algorithm

In this section, we present a family of algorithms [Wagner & Schneider (2005)] which are an extension of the leap-frog scheme and improve the accuracy of the dispersion error in terms of isotropy. The algorithm is also defined in a staggered cubic mesh with the velocity and the acoustic pressure computed at interleaved positions and times. In this case, the velocity update equation takes the same form than for the leap-frog scheme. On the other hand, the spatial derivatives of the pressure update equation are approximated with a combination of the forward difference and a next-to-nearest neighbors difference,

$$\nabla_{\text{tot}} = (1-\Psi)\nabla + \Psi\nabla^{\text{iso}} \,. \qquad (4.24)$$

Both operators are weighed by an adimensional constant Ψ defined in the range of $[0,1/2]$.

In order to specify presicely a finite-difference operator $\nabla^{\rm iso}$, it is convenient to define the following discrete operators. We inherently assume a Cartesian grid of nodes at which samples of the fields are available. The shift operator $S_n(a)$ acting on a field $f(x,y,z,t)$ shifts the variables n on f by $a\delta_n$, that is the grid sparcing in the n direction. Thus, for example, $S_n(a)f(x,y,z,t) = f(x+a\delta_x,y,z,t)$. With the shift operator the central finite difference are

$$D_n = \frac{S_n(\frac{1}{2}) - S_n(-\frac{1}{2})}{\delta_n} \ , \quad n \in (x,y,z,t) \ . \tag{4.25}$$

For the present algorithm the following averaging operators are also needed

$$A_n = \frac{S_n(1) + S_n(-1)}{2} \ , \quad n \in (x,y,z,t) \ . \tag{4.26}$$

For example, the x component of the next-to-nerarest neightbour difference operator, $\nabla^{\rm iso}$, averages four nodes by taking the finite difference of the average of the opposite face,

$$\nabla^{\rm iso}_x = D_x \frac{A_y + A_z}{2} = \frac{(S_x(\frac{1}{2}) - S_x(-\frac{1}{2}))(S_y(1) + S_y(-1) + S_z(1) + S_z(-1))}{4\delta} \ . \tag{4.27}$$

In three dimensions, the explicit form of this family of algorithms reads as follows,

$$\begin{aligned}
v_x|^{n+1/2}_{i+1/2,j,k} &= v_x|^{n-1/2}_{i+1/2,j,k} - a_1(p|^n_{i+1,j,k} - p|^n_{i,j,k}) \ , \\
v_y|^{n+1/2}_{i,j+1/2,k} &= v_y|^{n-1/2}_{i,j+1/2,k} - a_1(p|^n_{i,j+1,k} - p|^n_{i,j,k}) \ , \\
v_z|^{n+1/2}_{i,j,k+1/2} &= v_z|^{n-1/2}_{i,j,k+1/2} - a_1(p|^n_{i,j,k+1} - p|^n_{i,j,k}) \ ,
\end{aligned}$$

$$\begin{aligned}
p|^{n+1}_{i,j,k} = \quad & p|^n_{i,j,k} - (1-\Psi)a_2\Big(v_x|^{n+1/2}_{i+1/2,j,k} - v_x|^{n+1/2}_{i-1/2,j,k} + v_y|^{n+1/2}_{i,j+1/2,k} \\
- \quad & v_y|^{n+1/2}_{i,j-1/2,k} + v_z|^{n+1/2}_{i,,j,k+1/2} - v_z|^{n+1/2}_{i,j,k-1/2} \Big) - \Psi\frac{a_2}{4}\Big(v_x|^{n+1/2}_{i+1/2,j+1,k} \\
+ \quad & v_x|^{n+1/2}_{i+1/2,j-1,k} - v_x|^{n+1/2}_{i-1/2,j+1,k} - v_x|^{n+1/2}_{i-1/2,j-1,k} + v_x|^{n+1/2}_{i+1/2,j,k+1} \\
+ \quad & v_x|^{n+1/2}_{i+1/2,j,k-1} - v_x|^{n+1/2}_{i-1/2,j,k+1} - v_x|^{n+1/2}_{i-1/2,j,k-1} + v_y|^{n+1/2}_{i+1,j+1/2,k} \\
+ \quad & v_y|^{n+1/2}_{i-1,j+1/2,k} - v_y|^{n+1/2}_{i+1,j-1/2,k} - v_y|^{n+1/2}_{i-1,j-1/2,k} + v_y|^{n+1/2}_{i,j+1/2,k+1} \\
+ \quad & v_y|^{n+1/2}_{i,j+1/2,k-1} - v_y|^{n+1/2}_{i,j-1/2,k+1} - v_y|^{n+1/2}_{i,j-1/2,k-1} + v_z|^{n+1/2}_{i+1,j,k+1/2} \\
+ \quad & v_z|^{n+1/2}_{i-1,j,k+1/2} - v_z|^{n+1/2}_{i+1,j,k-1/2} - v_z|^{n+1/2}_{i-1,j,k-1/2} + v_z|^{n+1/2}_{i,j+1,k+1/2} \\
+ \quad & v_z|^{n+1/2}_{i,j-1,k+1/2} - v_z|^{n+1/2}_{i,j+1,k-1/2} - v_z|^{n+1/2}_{i,j-1,k-1/2} \Big) \ .
\end{aligned} \tag{4.28}$$

First, note that the leap-frog algorithm (4.16), is recovered when $\Psi = 0$. Also, observe that this algorithm requires more operations per iteration than the classical leap-frog. Moreover, the dispersion relation is obtained similarly than for the leap-frog scheme. In three dimensions, the dispersion relation reads,

$$\begin{aligned} S^{-2}\sin^2\left(\frac{\pi S}{N_\lambda}\right) &= \left[1-\Psi+\frac{\Psi}{2}\left(\cos\left(\frac{2\pi c\sin\theta\sin\phi}{N_\lambda c_{\text{num}}}\right)+\cos\left(\frac{2\pi c\cos\phi}{N_\lambda c_{\text{num}}}\right)\right)\right] \\ &\times\sin^2\left(\frac{\pi c\cos\theta\sin\phi}{N_\lambda c_{\text{num}}}\right)+\left[1-\Psi+\frac{\Psi}{2}\left(\cos\left(\frac{2\pi c\cos\theta\sin\phi}{N_\lambda c_{\text{num}}}\right)\right.\right. \\ &\left.\left.+\cos\left(\frac{2\pi c\cos\phi}{N_\lambda c_{\text{num}}}\right)\right)\right]\sin^2\left(\frac{\pi c\sin\theta\sin\phi}{N_\lambda c_{\text{num}}}\right)+\left[1+\Psi\right. \\ &\left.+\frac{\Psi}{2}\left(\cos\left(\frac{2\pi c\sin\theta\sin\phi}{N_\lambda c_{\text{num}}}\right)+\cos\left(\frac{2\pi c\cos\theta\sin\phi}{N_\lambda c_{\text{num}}}\right)\right)\right] \\ &\times\sin^2\left(\frac{\pi c\cos\phi}{N_\lambda c_{\text{num}}}\right). \end{aligned} \tag{4.29}$$

Observe that these algorithms depend on S, N_λ, the orientation of the plane waves and, moreover, the adimensional parameter Ψ. When $\Psi = 1/3$ it arise an algorithm which leads an accuracy of second order in the derivatives and fourth order in isotropy; more specifically, $c_{\text{num}} = c + \mathcal{O}(\Delta x^6, \Delta t^6)$. It means that, under these assumptions, c_{num} has almost an isotropic behavior and, therefore, the acoustic responses computed with this algorithm exihibit a numerical dispersion error that only depends on the frequency of the plane waves. This error can be easily corrected from the acoustic response instead of the one obtained with the classical leap-frog scheme. On the other hand, the computation of the next-to-nearest difference increases the Courant stability number which can be found by using complex frequency analysis leading to the following expression:

$$S = \begin{cases} \frac{1}{\sqrt{3}} & \text{for } \Psi = 0, \text{ the leap-frog scheme,} \\ \frac{1}{\sqrt{3(1-2\Psi)}} & \text{for } 0 \le \Psi \le \frac{1}{4}, \\ \frac{1}{\sqrt{2(1-\Psi)}} & \text{for } \frac{1}{4} \le \Psi \le \frac{1}{2}. \end{cases} \tag{4.30}$$

In order to obtain a centered version of the family of algorithms, Eq. (4.28), it is essential to define the acoustic quantities in a time and space centered mesh. In this case, all the acoustic information is evaluated either the same time and position and the spatial and temporal derivatives are approximated through first order finite difference operators taking the following form:

$$
\begin{aligned}
v_x|^{n+1}_{i,j,k} &= v_x|^{n}_{i,j,k} - a_1(p|^{n}_{i+1,j,k} - p|^{n}_{i,j,k}) \,, \\
v_y|^{n+1}_{i,j,k} &= v_y|^{n}_{i,j,k} - a_1(p|^{n}_{i,j+1,k} - p|^{n}_{i,j,k}) \,, \\
v_z|^{n+1}_{i,j,k} &= v_z|^{n}_{i,j,k} - a_1(p|^{n}_{i,j,k+1} - p|^{n}_{i,j,k}) \,, \\
p|^{n+1}_{i,j,k} &= p|^{n}_{i,j,k} - (1-\Psi)a_2\Big(v_x|^{n+1}_{i,j,k} - v_x|^{n+1}_{i-1,j,k} + v_y|^{n+1}_{i,j,k} - v_y|^{n+1}_{i,j-1,k} \\
&+ v_z|^{n+1}_{i,,j,k} - v_z|^{n+1}_{i,j,k-1} \Big) - \Psi\frac{a_2}{4}\Big(v_x|^{n+1}_{i,j+1,k} + v_x|^{n+1}_{i,j-1,k} - v_x|^{n+1}_{i-1,j+1,k} \\
&- v_x|^{n+1}_{i-1,j-1,k} + v_x|^{n+1}_{i,j,k+1} + v_x|^{n+1}_{i,j,k-1} - v_x|^{n+1}_{i-1,j,k+1} - v_x|^{n+1}_{i-1,j,k-1} + v_y|^{n+1}_{i+1,j,k} \\
&+ v_y|^{n+1}_{i-1,j,k} - v_y|^{n+1}_{i+1,j-1,k} - v_y|^{n+1}_{i-1,j-1,k} + v_y|^{n+1}_{i,j,k+1} + v_y|^{n+1}_{i,j,k-1} - v_y|^{n+1}_{i,j-1,k+1} \\
&- v_y|^{n+1}_{i,j-1,k-1} + v_z|^{n+1}_{i+1,j,k} + v_z|^{n+1}_{i-1,j,k} - v_z|^{n+1}_{i+1,j,k-1} - v_z|^{n+1}_{i-1,j,k-1} + v_z|^{n+1}_{i,j+1,k} \\
&+ v_z|^{n+1}_{i,j-1,k} - v_z|^{n+1}_{i,j+1,k-1} - v_z|^{n+1}_{i,j-1,k-1} \Big) \,. \qquad (4.31)
\end{aligned}
$$

Observe that the velocity update equations employ the forward difference for the temporal and spatial derivatives and conversely, the pressure update equation uses the backward difference for both derivatives. Moreover, note that for $\Psi = 0$, the centered leap-frog scheme is recovered. Finally, remark that this family of centered algorithms achieves the same Courant stability number, Eq. (4.30), and the dispersion relation, Eq. (4.29), than for the staggered version.

4.5 The MacCormarck Algorithm

In this section, we present the MacCormack algorithm, which is a two-step explicit method.[Hoffman (1992)] We have chosen this scheme for different reasons: on the one hand, this is a very popular scheme for dealing with Navier-Stokes equations and its performance for acoustic simulations have been only recently investigated; on the other hand, unlike the algorithms studied in the preceding sections, it uses a centered mesh (i.e. pressure and velocities are computed at the same points of the mesh).

Consider that the space is discretized on a centered cubic mesh. The nodes of the grid i, j, k at a time n are characterized by the following four quantities: velocity $\mathbf{v}|^{n}_{i,j,k} = (v_x, v_y, v_z)|^{n}_{i,j,k}$ and pressure $p|^{n}_{i,j,k}$. The MacCormack method consist on integrating the equations of motion in two steps. The first step is given by:

$$
\begin{aligned}
\widehat{v_x}|^{n+1}_{i,j,k} &= v_x|^n_{i,j,k} - a_1(p|^n_{i+1,j,k} - p|^n_{i,j,k}) \,, \\
\widehat{v_y}|^{n+1}_{i,j,k} &= v_y|^n_{i,j,k} - a_1(p|^n_{i,j+1,k} - p|^n_{i,j,k}) \,, \\
\widehat{v_z}|^{n+1}_{i,j,k} &= v_z|^n_{i,j,k} - a_1(p|^n_{i,j,k+1} - p|^n_{i,j,k}) \,, \\
\widehat{p}|^{n+1}_{i,j,k} &= p|^n_{i,j,k} - a_2\left(v_x|^n_{i+1,j,k} - v_x|^n_{i,j,k} + v_y|^n_{i,j+1,k} - v_y|^n_{i,j,k} + v_z|^n_{i,j,k+1} - v_z|^n_{i,j,k}\right) \,,
\end{aligned}
\tag{4.32}
$$

Note that $(\widehat{v_x}, \widehat{v_y}, \widehat{v_z}, \widehat{p})$ are auxiliary quantities which are used in the next step that reads,

$$
\begin{aligned}
v_x|^{n+1}_{i,j,k} &= \frac{1}{2}\left(v_x|^n_{i,j,k} + \widehat{v_x}|^{n+1}_{i,j,k}\right) - \frac{a_1}{2}\left(\widehat{p}|^{n+1}_{i,j,k} - \widehat{p}|^{n+1}_{i-1,j,k}\right) \,, \\
v_y|^{n+1}_{i,j,k} &= \frac{1}{2}\left(v_y|^n_{i,j,k} + \widehat{v_y}|^{n+1}_{i,j,k}\right) - \frac{a_1}{2}\left(\widehat{p}|^{n+1}_{i,j,k} - \widehat{p}|^{n+1}_{i,j-1,k}\right) \,, \\
v_z|^{n+1}_{i,j,k} &= \frac{1}{2}\left(v_z|^n_{i,j,k} + \widehat{v_z}|^{n+1}_{i,j,k}\right) - \frac{a_1}{2}\left(\widehat{p}|^{n+1}_{i,j,k} - \widehat{p}|^{n+1}_{i,j,k-1}\right) \,, \\
p|^{n+1}_{i,j,k} &= \frac{1}{2}\left(p|^n_{i,j,k} + \widehat{p}|^{n+1}_{i,j,k}\right) - \frac{a_2}{2}\Big(\widehat{v_x}|^{n+1}_{i,j,k} - \widehat{v_x}|^{n+1}_{i-1,j,k} + \widehat{v_y}|^{n+1}_{i,j,k} - \widehat{v_y}|^{n+1}_{i,j-1,k} + \widehat{v_z}|^{n+1}_{i,j,k} \\
&- \widehat{v_z}|^{n+1}_{i,j,k-1}\Big) \,.
\end{aligned}
\tag{4.33}
$$

The algorithm (4.32)-(4.33) is proposed as a numerical integration scheme of the linear equations of the acoustic field. Such a scheme has never been analyzed in full detail in this context. The dispersion relation in three dimensions is sufficiently complex to render it almost unusable. For illustrative purposes, the two dimensional MacCormack algorithm is analyzed. From the standard Von-Newmann analysis, we obtain to the following dispersion relation:

$$
\begin{aligned}
0 = & -\frac{1}{4}e^{-\imath k\Delta(\cos\theta+\sin\theta)}(-1+e^{\imath k\Delta x\cos\theta})^2(-1+e^{\imath k\Delta x\sin\theta})^2 S^4 \\
+ & \left(1-e^{-\imath\omega\Delta t}S^2[-1+\cos(k\Delta x\cos\theta)]\right)\left(1-e^{-\imath\omega\Delta t}+S^2[-1\right. \\
+ & \left.\cos(k\Delta x\sin\theta)]\right)\left(1-e^{-\imath\omega\Delta t}S^2[-2\cos(k\Delta x\cos\theta)+\cos(k\Delta x\sin\theta)]\right) \\
+ & S^2\sin^2(k\Delta x\cos\theta)\Big[[1-e^{-\imath\omega\Delta t}S^2(-1+\cos(k\Delta x\sin\theta))]\sin(k\Delta x\cos\theta) \\
- & \frac{1}{2}e^{\imath k\Delta x\cos\theta}(-1+e^{\imath k\Delta x\cos\theta})(-1+e^{\imath k\Delta x\sin\theta})S^2\sin(k\Delta x\sin\theta)\Big] \\
- & \frac{1}{2}S^2\sin(k\Delta x\sin\theta)\Big(S^2\sin(k\Delta x\cos\theta)[-1+e^{\imath k\Delta x\cos\theta}][-1+e^{\imath k\Delta x\sin\theta}] \\
- & 2\left[-1+e^{-\imath\omega\Delta t}+S^2-S^2\cos(k\Delta x\cos\theta)\right]\sin(k\Delta x\sin\theta)\Big),
\end{aligned}
\tag{4.34}
$$

The equality of Eq. (4.34) can only be satisfied for complex values of $k = \alpha + \imath\beta$. The velocity of propagation of the simulated wave is then related to the real part of k via $c_{num} = \frac{2\pi\nu}{\alpha}$. On the other hand, the imaginary part of k corresponds to a (mild) exponential damping of the plane waves along their propagation in the mesh. Its non-zero value is due to the fact that the MacCormack scheme is not perfectly conservative. Note that Eq. (4.34) is a rather complicated implicit equation for c_{num}. Finally, the Courant stability number of the MacCormack scheme is obtained through a conventional analysis leading to exactly the same relation than for the leap-frog scheme, Eq. (4.21).

4.6 The PSTD Algorithm

Although the Fourier spectral PSTD method introduced by Liu [Liu (1997)] was originally formulated for the numerical solution of Maxwell's equations, it can be easily adapted to acoustic wave propagation [Liu (1998)]. The basic formulation of the algorithm used a centered cubic mesh where velocity and pressure are located at nodes (i,j,k). Conversely, both quantities are computed at interleaved time steps, so the velocities are computed at a time step $n+1/2$ and the pressure at n. The spatial derivatives of the partial differential equations are approximated using the pseudo-spectral techniques explained in Sec. 4.2 and the temporal derivatives use the first order finite difference operators. In three dimensions, the explicit form of the PSTD scheme for the linear Euler equations is given by:

$$
\begin{aligned}
v_x|_{i,j,k}^{n+1/2} &= v_x|_{i,j,k}^{n-1/2} - \frac{\Delta t}{\rho}\mathscr{F}_x^{-1}\left[\imath\frac{2\pi n_x}{N_x\Delta x}\mathscr{F}_x[p|_{:,j,k}^{n}]\right] , \\
v_y|_{i,j,k}^{n+1/2} &= v_y|_{i,j,k}^{n-1/2} - \frac{\Delta t}{\rho}\mathscr{F}_y^{-1}\left[\imath\frac{2\pi n_y}{N_y\Delta y}\mathscr{F}_y[p|_{i,:,k}^{n}]\right] , \\
v_z|_{i,j,k}^{n+1/2} &= v_z|_{i,j,k}^{n-1/2} - \frac{\Delta t}{\rho}\mathscr{F}_z^{-1}\left[\imath\frac{2\pi n_z}{N_z\Delta z}\mathscr{F}_z[p|_{i,j,:}^{n}]\right] , \\
p|_{i,j,k}^{n+1} &= p|_{i,j,k}^{n} - \rho c^2\Delta t\,\mathscr{F}_x^{-1}\left[\imath\frac{2\pi n_x}{N_x\Delta x}\mathscr{F}_x[v_x|_{:,j,k}^{n+1/2}]\right] \\
&\quad -\rho c^2\Delta t\,\mathscr{F}_y^{-1}\left[\imath\frac{2\pi n_y}{N_y\Delta y}\mathscr{F}_y[v_y|_{i,:,k}^{n+1/2}]\right] \\
&\quad -\rho c^2\Delta t\,\mathscr{F}_z^{-1}\left[\imath\frac{2\pi n_z}{N_z\Delta z}\mathscr{F}_z[v_y|_{i,k,:}^{n+1/2}]\right] ,
\end{aligned}
\tag{4.35}
$$

where $\mathscr{F}_\mu$ and $\mathscr{F}_\mu^{-1}$ denote the Fourier transform over the μ-axis and its inverse respectively; n_x, n_y and n_z are the index of the Fourier transforms, and the : symbol denotes all μ-coordinate along the straightline cut through the space lattice. Finally, N_μ are the total grid points over the μ-axis.

A direct consequence of Eq. (4.35) is that the stability criterium does not depend on N_λ, which may be set to a value as low as 2. Similarly, from a dispersion

error point of view, PSTD methods exhibit a perfectly isotropic relation, *i.e.* the ratio c/c_{num} does not depend on the propagation angle θ. More specifically, for large enough numerical domains:

$$\frac{c_{\text{num}}}{c} = \frac{\pi}{N_T \sin\left(\frac{\pi}{N_T}\right)}, \qquad N_T := \frac{T}{\Delta t}, \tag{4.36}$$

where T is the period of the wave and N_T controls the time discretization. A standard Von Neumann analysis [Hoffman (1992)] yields the following Stability Courant number, S, for the PSTD method,

$$S = c\frac{\Delta t}{\delta} \leq \frac{2}{\pi\sqrt{D}}, \tag{4.37}$$

where D represents the dimension (in the case of Eq. (4.35) is 3). Note that S in PSTD method is smaller than in any algorithm based on FDTD methods, which means that PSTD is stable for larger cell sizes than FDTD (with the same time discretization step).

As we show before, this algorithm is defined in a spatial centered cubic mesh where the pressure and the velocity components are computed at interleaved time steps. To build the centered version of this algorithm, it is necessary to define the acoustic quantities also at the same time step. Hence, As for the centered version of FDTD algorithms, the temporal derivatives are approximated similarly with the combination of the forward and the backward finite difference operators, obtaining the following analogous algorithm:

$$\begin{aligned}
v_x|^{n+1}_{i,j,k} &= v_x|^{n}_{i,j,k} - \frac{\Delta t}{\rho}\mathscr{F}_x^{-1}\left[\imath\frac{2\pi n_x}{N_x\Delta x}\mathscr{F}_x[p|^n_{:,j,k}]\right], \\
v_y|^{n+1}_{i,j,k} &= v_y|^{n}_{i,j,k} - \frac{\Delta t}{\rho}\mathscr{F}_y^{-1}\left[\imath\frac{2\pi n_y}{N_y\Delta y}\mathscr{F}_y[p|^n_{i,:,k}]\right], \\
v_z|^{n+1}_{i,j,k} &= v_z|^{n}_{i,j,k} - \frac{\Delta t}{\rho}\mathscr{F}_z^{-1}\left[\imath\frac{2\pi n_z}{N_z\Delta z}\mathscr{F}_z[p|^n_{i,j,:}]\right], \\
p|^{n+1}_{i,j,k} &= p|^{n}_{i,j,k} - \rho c^2\Delta t\mathscr{F}_x^{-1}\left[\imath\frac{2\pi n_x}{N_x\Delta x}\mathscr{F}_x[v_x|^{n+1}_{:,j,k}]\right] \\
&\quad -\rho c^2\Delta t\mathscr{F}_y^{-1}\left[\imath\frac{2\pi n_y}{N_y\Delta y}\mathscr{F}_y[v_y|^{n+1}_{i,:,k}]\right] - \rho c^2\Delta t\mathscr{F}_z^{-1}\left[\imath\frac{2\pi n_z}{N_z\Delta z}\mathscr{F}_z[v_y|^{n+1}_{i,k,:}]\right]
\end{aligned}, \tag{4.38}$$

observe that the velocity update equations use the forward difference and the pressure update equation employs the backward difference to approximate the temporal derivatives of the Euler equations. Once again, this numerical algorithm presents exactly the same Courant stability number and the dispersion error than the time staggered algorithm presented by Liu. [Liu (1997)]

Finally, as for the FDTD leap-frog scheme, we present the formulation of the PSTD algorithm based on the wave equation since it is more convenient in room acoustics applications

$$\begin{aligned} p|_{i,j,k}^{n+1} &= -p|_{i,j,k}^{n-1} + 2p|_{i,j,k}^{n} + (c\Delta t)^2 \left(\mathscr{F}_x^{-1} \left[\left(\iota \frac{2\pi n_x}{N_x \Delta x} \right)^2 \mathscr{F}_x [p|_{:,j,k}^{n}] \right] \right. \\ &+ \left. \mathscr{F}_y^{-1} \left[\left(\iota \frac{2\pi n_y}{N_y \Delta y} \right)^2 \mathscr{F}_y [p|_{i,:,k}^{n}] \right] + \mathscr{F}_z^{-1} \left[\left(\iota \frac{2\pi n_z}{N_z \Delta z} \right)^2 \mathscr{F}_z [p|_{i,j,:}^{n}] \right] \right) , \end{aligned} \tag{4.39}$$

Note that this numerical scheme leads to the same dispersion error and Courant stability number than the PSTD algorithms based on the Euler equations.

4.7 Additional Remarks

However, one important drawback of PSTD methods is that the computation of the spectral derivative assumes a periodic distribution of the acoustic quantities over the numerical domain. If the distribution is non periodic, the accuracy of the spectral derivative is affected by an error called the Gibbs phenomenon. This error becomes critical in any numerical simulation even for space and time discretizations fitted by the Courant stability number, Eq. (4.37).

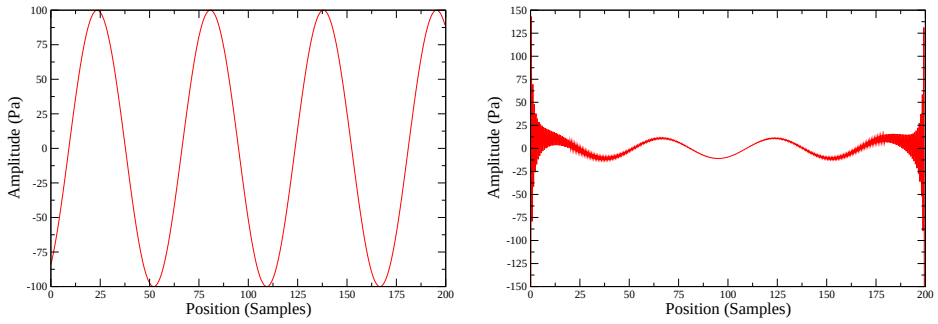

Figure 4.3: A non periodic sinusoidal function $f(x)$ (the left one) and its derivative computed with spectral analysis(the right one). Observe that the Gibbs phenomenon appears at the edges of the derivated function.

In Fig. 4.3 a pedagogical example is shown: A non periodic sinusoidal distribution $f(x)$ is derived by using the Fourier techniques. The resultant derivative is plotted in Fig. 4.3 (right). Observe that the Gibbs phenomenon appears at the edges of the derivated function since $f(x)$ is defined as a non periodic function. Therefore, numerical simulations based on Fourier techniques can

only be stable if some periodic boundary conditions are defined at the edges of the numerical domain (i.e. $p = v = 0$).

However, some applications, such as room acoustic modelling and aeroacoustic, require to define partially absorbing boundary conditions through an impedance. The performance of these reflecting boundary conditions in PSTD methods has not been done yet, since to define it as a problem with different domains causes serious difficulties in their implementation [Fornberg (1996)].

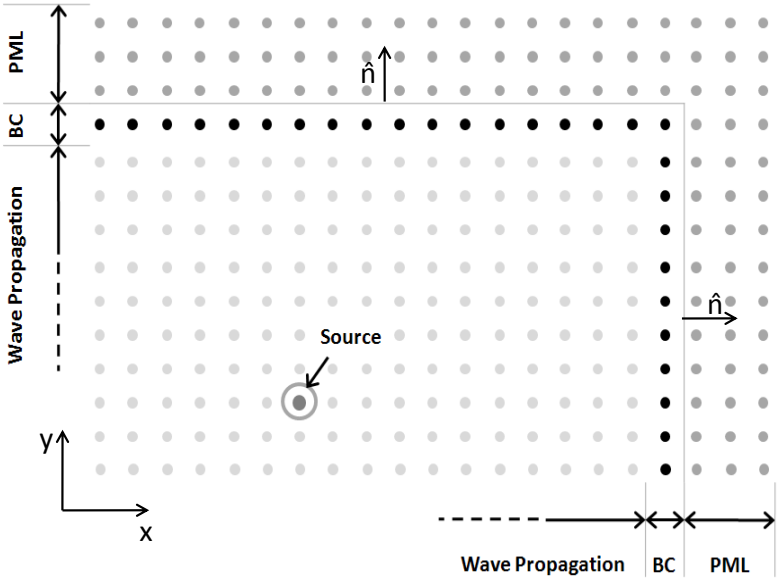

Figure 4.4: Representation of a typical room acoustics simulation. In PSTD methods, PML nodes are added next to the BC nodes in order to avoid the Gibbs phenomenon absorbing the transmitted field in the outward direction $\hat{\mathbf{n}}$.

This can be mostly avoided through the definition of some extra nodes beyond the contours of the discretised domain. These nodes are governed by absorbing boundary conditions such as the Perfectly Matched Layer (PML). Basically, the PML equations absorb smoothly the transmitted energy by keeping to 0 the pressure (and the velocity) of the new edges, and consequently getting a periodic distribution of the acoustic quantities. In Fig. 4.4, it is illustrated a typical PSTD numerical simulation in room acoustics. Commonly, a punctual source is located somewhere within the nodes governed by the propagation algorithm. Moreover, the walls of the numerical enclosure are characterized by another update equation which takes into account the geometry of the walls and the acoustic properties of the materials (i.e. numerical BCs). Therefore, In PSTD methods, it should be added beyond the impedance boundary layers

some extra PML nodes, in order to obtain a periodic distribution of the acoustic quantities at the edges of the simulated domain. As mentioned, PML nodes absorb the acoustic field transmitted in the outward direction $\hat{\mathbf{n}}$ by the impedance boundary layer.

The first formulation of the PML for the Euler equations was presented in the context of electromagnetism [Berenger (1996)]. The Perfectly Matched Layer method for the Yee algorithm was presented also in 1995 [Maloney & Cummings (1995)] for acoustic and elastic modelling. It was further developed for the acoustics using either FDTD methods [Hu (1996)] or PSTD algorithm [Liu (1999)]. Conversely, using the wave equation, PML have only been presented for FDTD methods [Zhou & Huang (2001)] since their formulation is considerably more difficult than the Eulerian PML equations. Although these extra nodes increase the computational cost of the algorithm, It is reported in the literature, [Zhou & Huang (2001); Liu (1999)] that only of the order of 16 nodes are required to absorb completely all the acoustic field. If big enclosures are considered, such as concert halls or theatres, the increase of the computational cost due to the PMLs can be considered irrelevant. We left in the appendix A the numerical algorithms for different formulations.

4.8 Numerical Validation in 2D Algorithms

In this section we present a general numerical methodology for computing c/c_{num} via simulations of any FDTD algorithm in 2D. In the method presented, a numerical plane wave is employed to validate dispersion relations as originally proposed by Zhao and Mäkinen [Zhao & Mäkinen (2004)]. In this paper, the authors show that a plane wave is more suitable than the commonly used point source [Namiki & Ito (2000); Sun & Trueman (2003)], for the purpose of verifying dispersion relations numerically. Our proposal allow for a statistical determination of the numerical speed of sound and is suitable for any FDTD scheme and for reasonable low values of the number of cells per wavelength.

We apply our methodology to qualitatively different types of FDTD schemes: the original algorithm by Yee [Yee (1966)] and its recent extensions;[Wagner & Schneider (2005)] the acoustic version of the MacCormack scheme;[Garriga et al. (2005)] and the recently developed pseudospectral techniques (PSTD) [Liu (1997)].

The results obtained prove that the methodology provides very accurate computations of c/c_{num} even for low cells per wavelength. This, together with the fact that it is easily generalizable to 3D, makes it a suitable technique to faithfully research on numerical dispersion errors in the implementation of FDTD algorithms in acoustic problems.

In this section, we present a general methodology for computing the numerical speed of sound in two-dimensional FDTD schemes. The method consists on creating plane waves travelling in different orientations and following their propagation throughout the mesh. The plane waves are created by exciting a set of

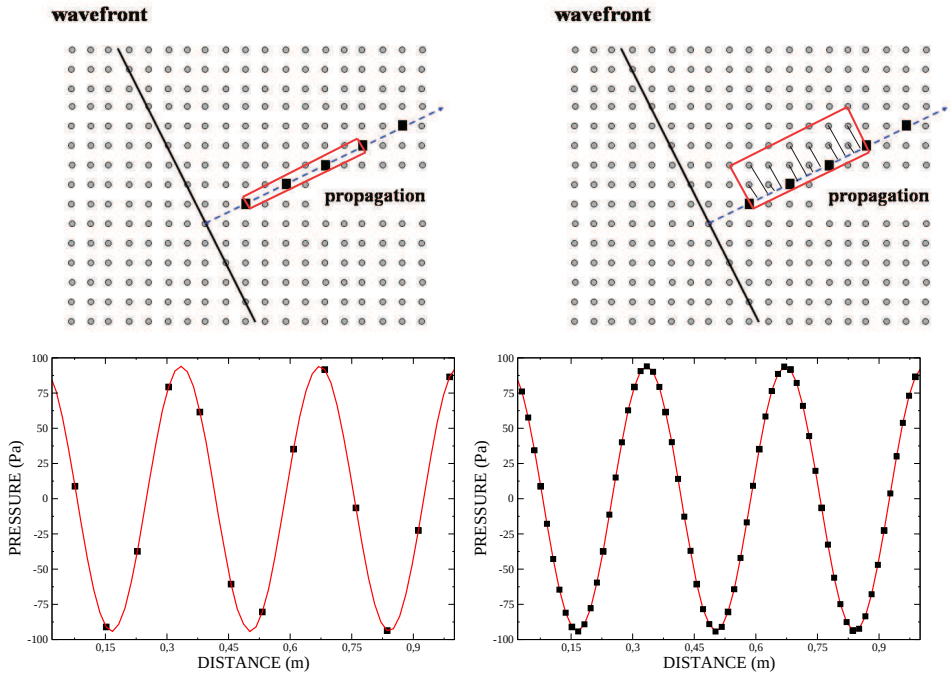

Figure 4.5: Upper row: schematic representation of wavefronts propagating within the mesh, at a 26 degrees angle with respect to the axes. Lower row: the result of sampling the pressure field along a line parallel to the propagation direction. Left column: only points directly over such line are considered, leading to a small density of sampling points (square dots). Right column: all other mesh points are projected, leading to a larger sampling density.

mesh points with a time-varying sinusoidal pressure signal $p|_{i,j}^{n} = p_0 \sin(2\pi\nu n\Delta t)$. Here, Δt is the time discretization interval, n is the time step, (i, j) are the two-dimensional spacial coordinates and ν the frequency of the plane wave. We always set $p_0 = 100$ Pa for illustrative purposes. The orientation of the plane waves, *i.e.* the angle θ between the wavefront and the x-axis, is fixed by selecting the excited points to be those for which $\tan\theta = \frac{j}{i}$. This, in turn, implies that the wavefront propagates with velocity parallel to the vector $(j, -i)$.

In order to avoid numerical reflections and to obtain accurate results, we have considered huge lattices [1], with large Perfectly Matched Layers [Berenger (1996)] (PML) at the boundaries. We have chosen PML absorbing boundary conditions not only for their good performance [Yuan et al. (1997)] but also for preserving the numerical stability of the algorithms. Finally, we measure

[1] Each dimension is about one hundred times the wavelength

the pressure in a region [2] near the center of the mesh at a time sufficiently short to ensure stationarity. Considering only the pressure at a set of points along the direction of propagation $(j,-i)$ as shown in Fig. 4.5 (upper-left hand corner) we obtain a snapshot like the one in Fig. 4.5 (lower-left hand corner). However, it is worth emphasizing that for most angles, the number of points per wavelength obtained by the previous procedure is very small. One simple way to greatly improve the accuracy is to project the pressure information of other mesh points to the line $(j,-i)$ perpendicular to the wave front, Fig. 4.5 (upper-right hand corner). This leads to a substantial increase on the density of points per wavelength, as observed in Fig. 4.5 (lower-right hand corner), and, therefore, to a reduction of the error in c_{num} associated to the fit.

Finally, by fitting a simple sinusoidal function

$$p = p_0 \sin(k_{\text{num}} x + \phi)\,, \tag{4.40}$$

we can easily obtain the numerical wavelength, and therefore the numerical speed of sound,

$$c_{\text{num}} = \frac{2\pi\nu}{k_{\text{num}}}\,. \tag{4.41}$$

4.8.1 The Yee Algorithm

The scheme is defined on a Cartesian staggered grid with pressure and particle velocity components located at interleaved positions. Spatial and temporal derivatives of the governing partial differential equations are approximated by central-differences leading to second-order accuracy in time and space. As we mentioned, the analysis of the dispersion error is obtained with the 2D algorithm of the leap-frog scheme that can be straightforwardly derived from Eq. (4.16).

In order to test our methodology, we compared the values of c/c_{num} obtained from our simulations to those expected from the analytic equation (4.20) by fixing $\phi = 0$. Fig. 4.6 shows the comparison in two cases with equal $S = 1/\sqrt{2}$, but different N_λ. The continuous lines are obtained from the analytic result, Eq. (4.20), whereas dots and error bars were obtained with our methodology after averaging over 15 different different times (snapshots). As it can be seen, the results of the numerical simulations are excellent and the magnitude of error is of order $1/1000$ even for $N_\lambda = 10$ cpw.

[2] The length is about five times the wavelength

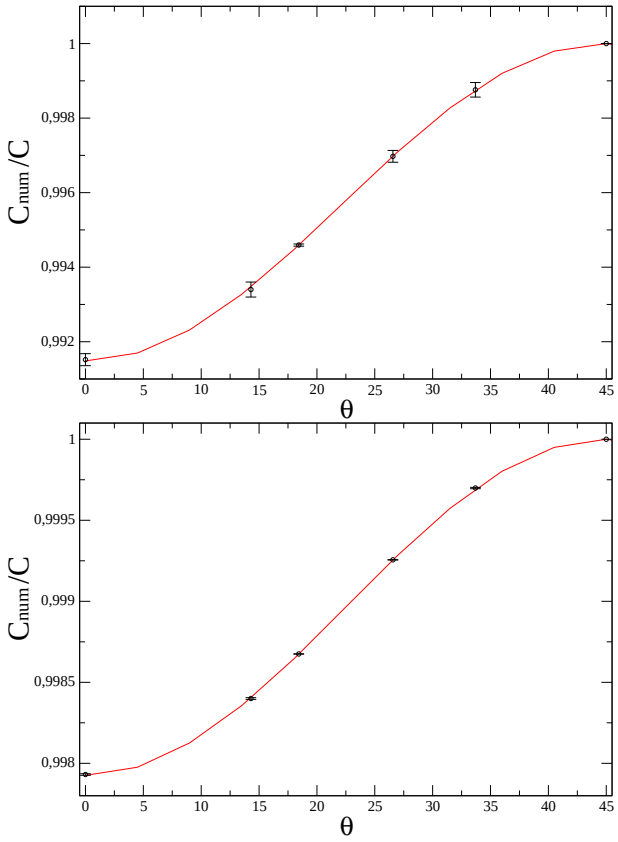

Figure 4.6: Analytical (continuous line) and numerical (dots) results for different angles of propagation in Yee's algorithm. (up), $N_\lambda = 10$ cpw; (down), $N_\lambda = 20$ cpw. In both cases $S = 1/\sqrt{2}$.

4.8.2 A Parametric FDTD Algorithm

In this section, we discuss a family extensions of Yee's algorithm that improves its accuracy in terms of isotropy. The spatial derivatives employ a combination of differences between nearest neighbors and a next-to-nearest neighbors, Eq. (4.28). Following Wagner et al. conventions, [Wagner & Schneider (2005)] this family of algorithms is parameterized by a constant, Ψ, within the range $[0, 1/2]$ (see Sec. 4.4). In two dimensions, it turns out that for the particular value $\Psi = 1/6$, the scheme leads to fourth order accuracy in isotropy. Moreover, the original scheme by Yee is recovered simply by setting $\Psi = 0$.

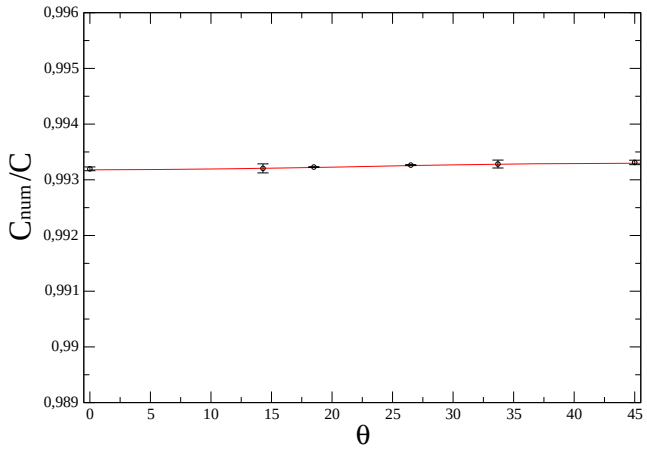

Figure 4.7: Analytical (continuous line) and numerical (dots) results for the family of Yee's extensions at the maximum allowed value of S, $N_\lambda = 10$cpw and $\Psi = 1/6$.

The dispersion relation following from a Von-Newmann analysis reads

$$\begin{aligned} S^{-2}\sin^2\left(\frac{\pi S}{N_\lambda}\right) &= \left[1-\Psi+\Psi\cos\left(\frac{2\pi c\sin\theta}{N_\lambda c_{\text{num}}}\right)\right]\sin^2\left(\frac{\pi c\cos\theta}{N_\lambda c_{\text{num}}}\right) \\ &+ \left[1-\Psi+\Psi\cos\left(\frac{2\pi c\cos\theta}{N_\lambda c_{\text{num}}}\right)\right]\sin^2\left(\frac{\pi c\sin\theta}{N_\lambda c_{\text{num}}}\right) . \quad (4.42) \end{aligned}$$

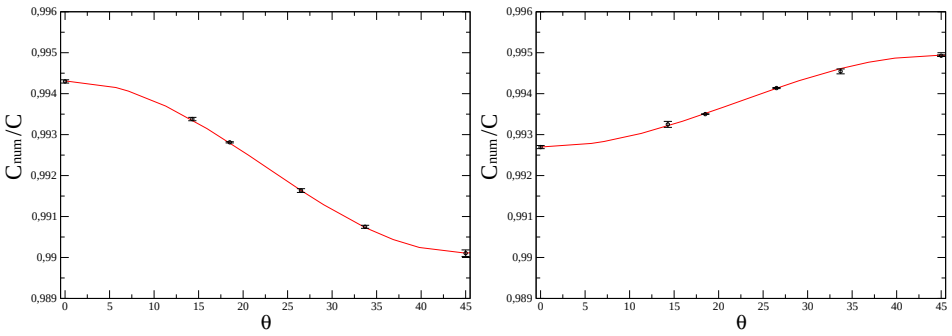

Figure 4.8: Analytical (continuous line) and numerical (dots) results for the family of Yee's extensions at the maximum allowed value of S, $N_\lambda = 10$cpw and $\Psi = 1/4$ (left) and $\Psi = 1/8$ (right).

Finally, we present the values of c/c_{num} obtained applying our method to

this family of algorithms in Figs. 4.8 and 4.7. Again, the continuous lines are derived from the analytic result, whereas dots and error bars were obtained with our methodology after averaging over 15 different times. The results obtained have the same accuracy than for the Yee algorithm in all cases tested.

4.8.3 The MacCormack Algorithm

The numerical scheme is obtained by integrating the equations of motion in two steps. The 2D algorithm can be obtained straightforwardly from Eqs. (4.32) and (4.33). Moreover, in Sec. 4.5 we present the analytic expression of the dispersion error observing a rather complicated equation that its analytic dispersion relation is complex enough to render it almost unusable. In cases like this, our methodology presents a simpler and more straightforward way to study the dispersion error.

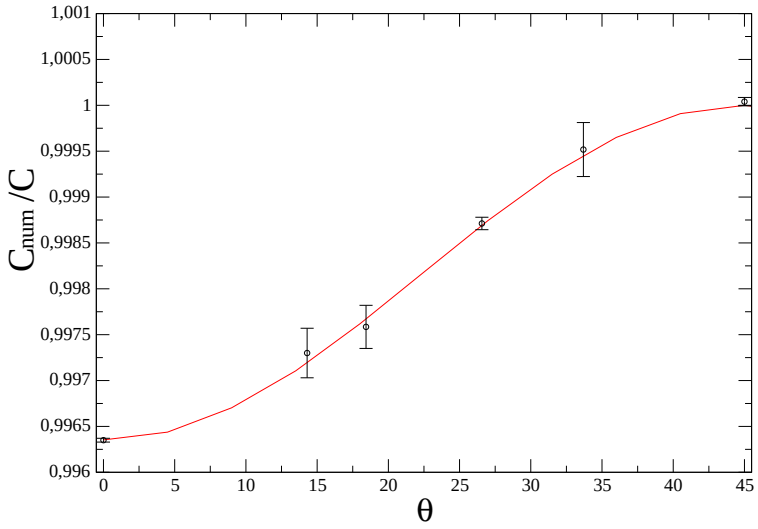

Figure 4.9: Comparison of analytical (continuous line) and numerical (dots) results for MacCormack's algorithm, with $N_\lambda = 30$ cpw and $S = 1/\sqrt{2}$.

The comparison with our methodology is presented in Fig 4.9, where excellent agreement is observed again. As can be shown in Fig. 4.9 we have obtained again accuracies of the order of 1/1000 averaging only over 15 snapshots.

4.8.4 PSTD Method

The FDTD methods are a simple, robust and powerful technique to simulate transient acoustic phenomena. However, the standard lore indicates that a spa-

tial sampling density above $10-15$ cells per wave-length is needed to produce accurate results. This problem becomes even more critical in large acoustic problems (such as rooms with long reverberation times), making it necessary to increase the spatial sampling rate beyond this range to reduce the cumulative numerical dispersion error.[Taflove (1995)] PSTD methods improve this situation significantly by using more refined approximations for spatial derivatives. For example, those PSTD methods based on Fourier transforms essentially use all the points in a given row of the mesh to approximate the partial derivative along the row direction.

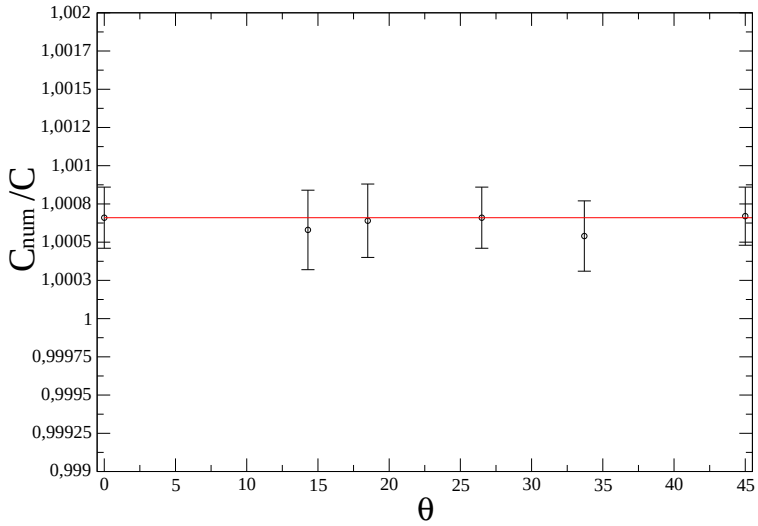

Figure 4.10: Dispersion error versus angle at fixed $N_\lambda = 10$cpw, $N_T = 50$. Note the almost perfect isotropy.

The results of our methodology applied to the Fourier transform PSTD scheme are compared to the analytical ones derived from Eqs. (4.36) and they are shown in Figs. 4.10 and 4.11. Once more, the agreement proves to be excellent in all the situations studied. Finally, we remark that this methodology is capable to mesaure the non-dependence in the variation of the spatial discretizations (i.e. N_λ) showing accurate results even for low cells per wavelength.

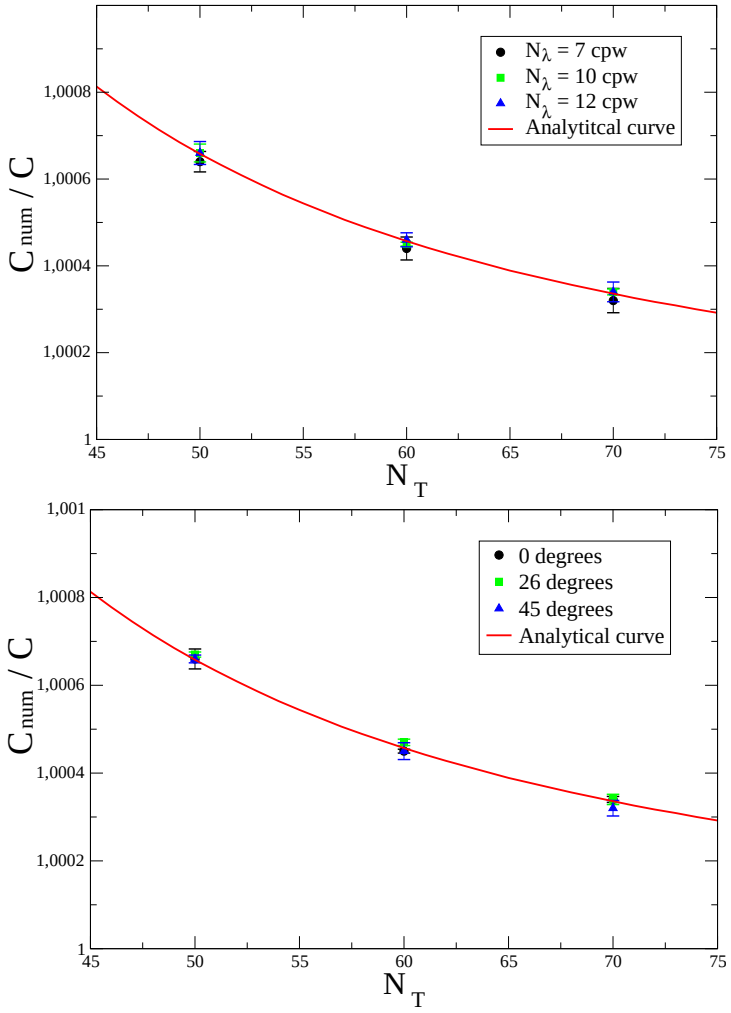

Figure 4.11: Analytical curve (continuous line) compared to numerical simulations (dots). Up: dispersion error versus time discretization N_T for different N_λ, at a fixed angle $\theta = 0$. Note the remarkable independence of the results of N_λ. Down: dispersion error versus N_T for different angles, at fixed $N_\lambda = 10$ cpw.

4.9 Conclusions and Remarks

In the previous section we have presented a general statistical methodology for studying and validating the dispersion error of generic FDTD algorithms by direct computation of the numerical speed of sound. The procedure is simple

but powerful, as it easily generates enough data to obtain computationally accuracies of the order of $1/1000$. We have shown that it applies equally well to a wide variety of qualitatively different schemes in 2D: FDTD in staggered and non-staggered meshes, isotropic extensions of FDTD, and pseudospectral techniques in time domain. We also have shown that the methodology works excellently even at low values of the number of cells per wavelength.

Finally, the methodology extends rather straightforwardly to 3D cubic meshes. To create plane waves, all that is needed is to excite a whole plane of the 3D mesh. The normal to the plane corresponds to the propagation direction, which can be used to sample the pressure field as described in Sec. 4.8, fit a sinusoidal function, and easily obtain the behavior of c/c_{num}.

As observed, one of the most important disadvantage of the FDTD methods for room acoustic applications is the inherent dispersion error [Taflove (1995); Hoffman (1992)]. As an example, we consider the dispersion relation for the classical leapfrog scheme in two dimensions [Yee (1966)]:

$$S^{-2}\sin^2\left(\frac{\pi S}{N_\lambda}\right) = \sin^2\left(\frac{\pi c}{N_\lambda c_{num}}\cos\theta\right) + \sin^2\left(\frac{\pi c}{N_\lambda c_{\text{num}}}\sin\theta\right) . \tag{4.43}$$

From Eq. (4.43) it can be seen that the numerical speed of sound, c_{num}, depends strongly not only on the Courant stability number, S, and the number of cells per wavelength, N_λ, but also on the direction of wave propagation across the two dimensional domain, θ.

One remarkable property of the PSTD method is the isotropy of the numerical speed of propagation instead of the FDTD techniques. More specifically, for large enough numerical domains a simple dispersion relation can be obtained, Eq. (4.36). Note that the dispersion error does not depend on the spatial discretization N_λ either. This fact allows to easily correct the dispersion error (at each frequency) avoiding erroneous results in the computation of acoustic impulse responses.

In the last years, some research has been devoted to the improvement of dispersion errors in FDTD/DWM methods [Savioja & Välimäki (2003); Fontana & Rocchesso (1998); Wagner & Schneider (2005)]. These algorithms improve the isotropy of the numerical sound propagation at the expense of computational cost. Figure 4.12 plots the dispersion error as a function of the angle of propagation (with respect the x-axis) using the minimum value of S allowed for each algorithm and for different N_λ.

Observe that the dispersion error in the leapfrog FDTD scheme depends strongly on the angle instead of PSTD method. Moreover, it is worth mentioning that PSTD gives less severe values of c_{num} at each N_λ. Therefore, from the dispersion error point of view, the PSTD method is clearly more suitable for room acoustic applications.

Another important feature of the PSTD method in comparison with FDTD methods is the reduction in computational cost. On the one hand, PSTD simulations require the computation of Fourier transforms which can be computed

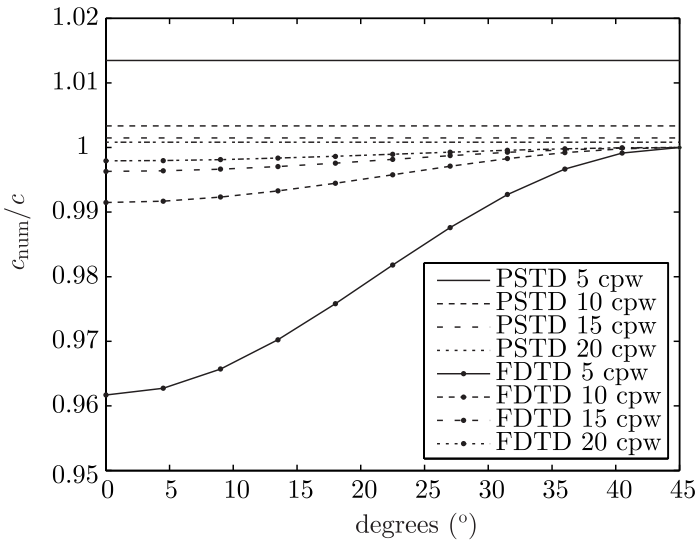

Figure 4.12: Dispersion Error for the PSTD algorithm in two dimensions with $S = 2/(\pi\sqrt{2})$ and $N_\lambda = 5, 10, 15, 20$ cpw and for the classical leapfrog method with $S = 1/\sqrt{2}$ and $N_\lambda = 5, 10, 15, 20$ cpw.

very efficiently through the Fast Fourier Transform algorithms [Cooley & Tukey (1965)]; on the other hand - and probably the most compelling feature - PSTD do not produce phase error even for two cells per wavelength, i.e $N_\lambda = 2$. This last property allows for a simulation of large spaces and computation of very long acoustic impulse responses.

Chapter 5

Source Generation in Numerical Methods

5.1 Introduction

During the previous chapter, some aspects concerning to the wave propagation have been considered. We presented either formulations based on FDTD methods (see from Sec. 4.3 to Sec. 4.5) or Fourier PSTD methods (See Secs. 4.6 and 4.7). In Sec. 4.8, an already propagating wave was assumed and no issues concerning to the wave generation has been addressed. This chapter is focused on the different ways to include sources and which are the possible consequences when a particular kind of source is selected. So far, technical literature has not highlighted some phenomena that appear as a consequence of the scenario dimension and how this would affect to the spectra of a propagated wave. For that reason, this chapter contributes with a deep analysis of the different source models and the effects derived from their use, even as a function of the scenario dimension.

In Sec. 5.3 we present the mathematical formulation derived from the Green's theory of the 2D and 3D sound propagation in the free space. Moreover, the numerical approximations of the source generation are overviewed in Sec. 5.4. In addition, we present a numerical experiment capable to measure the error produced by the numerical approximations (see in Sec. 5.5). Finally, Sec. 5.6 expose the conclusions derived from the analytical and numerical analysis.

5.2 Background

In time-domain numerical room acoustics, the source generation and nearly related topics have been barely pointed out. Currently, the way to excite a time-domain algorithm has been taken from the numerical electromagnetism basis. In that field, sources have been always assumed to be soft or hard [Taflove (1995)] (more details will be done at Secs. 5.4.1 and 5.4.2, respectively), and

same theoretical background has been adopted for numerical acoustics. The effect of both kind of sources have been analyzed from the point of view of how they might produce undesirable scattering effects, specially hard sources, but no deep analysis about their propagation characteristic has been found neither in time-domain numerical acoustics nor in room-acoustics topic.

From a deep review of the technical literature, few attempts to carry out some research concerning to source modeling have been made, which it might be classified in two big groups:

- In order to overcome the scattering effects produced by these kind of source implementations, Schneider et al. propose a new type of source called *transparent* sources [Schneider et al. (1998)]. That implementation was provided to be working with FDTD using Euler equations, and although reported results demonstrate the accuracy of that method, it requires a considerable increasing of memory and the room acoustic relevant publications do not use that kind of sources, giving a considerable success to soft sources or interrupted hard sources. Apart from that publication, this challenging topic has not been addressed in more works related to architectural acoustics.

- In sound source modeling, the directivity is a fundamental feature to a final simulation result. Unfortunately, there have only been a few attempts to solve this problem for such particular discrete-time methods, as they can only consider sources as monopoles. [H. Hacıhabiboğlu & Kondoz (2007)] proposes a method for a *Wave Digital Waveguide Mesh* (W-DWM) [Murphy et al. (2007)], achieving source modeling with a frequency -independent directivity and for those directivity diagrams which have dipole or quadrupole shapes. However, this is not a generalized method that can be used in other discrete-time methods, since W-DWM works with characteristic (*wave*) variables [Murphy et al. (2007)]. Furthermore, the same authors proposed an alternative method, also for a W-DWM, which was inspired from a well-known antenna theory principle [H. Hacıhabiboğlu & Kondoz (2008)]; this method provides very interesting and accurate results which are also frequency-dependent. However, in the results, they do not explore gradual transitions between the different directivity diagrams at consecutive frequencies and the impact of the mesh dispersion.

  At about the same time, an alternative method was proposed [Escolano et al. (2007)], based on a weighted combination of monopoles, in which the far-field pressure distribution is equal to that of a defined directivity. One of the main advantages of this method relies on the fact that, since it works with monopoles, it can be easily implemented in any discrete-time method, such as FDTD and PSTD. However, this method is limited to sinusoidal sources. More recently, that method has been extended

incorporating broadband directive sources with a frequency-dependent directivity [Escolano et al. (2009)].

5.3 Theoretical Analysis

As mentioned, there is a poor contribution in the literature according to the analysis of the punctual source generation. In this section we derive the Green's functions for the wave equation, both in 2 and 3 spatial dimensions. The Green's function is an essential building block in the simulation of sound propagation because, due to the linearity of the wave equation, the propagation of an arbitrary sound source can be simply expressed as a linear combination of suitably weighted and time-delayed Green's functions, the convolution operation (see in Secs. 2.3.2 and 2.3.4).

We will study only the direct sound, and therefore consider simple boundary conditions whereby the acoustic field vanishes at infinity. This will suffice to illustrate that, in 2D, a pulse emitted at one point propagates, not only over a spherical shell (whose radius increases with time), but it actually creates non-null values of the pressure field inside the shell.

In Sec. 2.3.2 we presented the 1D formulation of the Green's function for the wave equation. The Green's function g_D for the wave equation in D dimensions is, by definition, the unique solution of:

$$\left(-\frac{1}{c^2}\frac{\partial^2}{\partial t^2}-\nabla^2_{(D)}\right) g_D(\mathbf{x},t;\mathbf{x}_0,t_0) = \delta(t-t_0)\delta^{(D)}(\mathbf{x}-\mathbf{x}_0)\,, \tag{5.1}$$

$$g_D(\mathbf{x},t;\mathbf{x}_0,t_0) = 0 \quad \text{for } t<t_0\,, \tag{5.2}$$

$$g_D(\mathbf{x},t;\mathbf{x}_0,t_0) \to 0 \quad \text{as } |\mathbf{x}|\to\infty\,, \tag{5.3}$$

where

$$\nabla_{(D)} = \left(\frac{\partial}{\partial x_1},\ldots,\frac{\partial}{\partial x_D}\right) \qquad \delta^{(D)}(\mathbf{x}-\mathbf{x}_0) = \delta(x_1)\ldots\delta(x_D)\,, \tag{5.4}$$

are the D-dimensional gradient operator and delta function, respectively. The source is located at $\mathbf{x}=\mathbf{x}_0$, and it is active only at $t=t_0$. Note that the second condition in Eq. (5.1) is just the causality condition, whereas the third one is just a requirement that there are no sound sources at infinity (i.e. that all sources are located in a bounded region of space). It is straightforward to show that the Green's function depends only on the relative distance to the source $r=|\mathbf{r}|=|\mathbf{x}-\mathbf{x}_0|$ and the time difference $\tau=t-t_0$, which we will use to simplify notation and write $g_D(r,\tau)$.

A convenient expression to start the study of 2D and 3D Green's functions follows from performing a variables separation in the wave equation, going to the Fourier domain, and expressing the Green's function as a linear combination of normal-modes:

$$g_D(r,\tau) = u(\tau)\,\frac{c}{(2\pi)^D}\int d^D k \frac{\sin(|\mathbf{k}|c\tau)}{|\mathbf{k}|}e^{i\mathbf{k}\cdot\mathbf{r}}\,, \tag{5.5}$$

where $d^D k = dk_1 \ldots dk_D$ is the D-dimensional volume element, and $u(\tau)$ is the unit step function. From this expression, which is valid for any dimension[1], we will now obtain the explicit results in 2D and 3D.

5.3.1 Green's Function in 2D, Afterglow

In two dimensions, the integrals appearing in Eq. (5.5) can be performed using cylindrical coordinates:

$$\begin{aligned} g_2(r,\tau) &= \frac{u(\tau)c}{(2\pi)^2}\int_0^\infty d|\mathbf{k}||\mathbf{k}|\int_0^{2\pi} d\theta\,\frac{\sin(|\mathbf{k}|c\tau)}{|\mathbf{k}|}e^{i|\mathbf{k}||\mathbf{r}|\cos\theta} \\ &= \frac{u(\tau)c}{2\pi}\int_0^\infty d|\mathbf{k}|\sin(|\mathbf{k}|c\tau)J_0(|\mathbf{k}|r) = \frac{c}{2\pi}\frac{u(c\tau-r)}{\sqrt{c^2\tau^2-r^2}}\,. \end{aligned} \tag{5.6}$$

The integral involving the zero order Bessel function J_0 is rather standard (see, for example, [Barton (1989)]. It is convenient to rewrite Eq. (5.6) in terms of the time of arrival of the first wavefront, $t_a = R/c$,

$$g_2(r,\tau) = \frac{1}{2\pi}\frac{u(\tau-t_a)}{\sqrt{\tau^2-t_a^2}}\,. \tag{5.7}$$

The result of Eq. (5.7) has one main difference with respect to the 3D counterpart, Eq. (5.10): as soon as the impulse is created, the acoustic field (pressure and velocity) is non-null in the whole interior of a shell, the radius of which grows at the speed of sound. In other words, *a ideal microphone located at a fixed distance R from the source will record non-zero pressure values for an infinitely long time after the arrival of the first wavefront.*

Let us analyze with detail what such a microphone would record. The arrival of the first wavefront would produce an initial divergent signal (just as in 3D, being a consequence of the delta-source idealization). After that moment, the intensity of the signal would decrease monotonically. For times much larger than the time of arrival of the first front, $t \gg r/c$, the measured pressure signal would decrease a t^{-1}, implying a 6 dB decrease every time $t \to 2t$.

This particular feature of the 2D propagation is known as afterglow phenomenon and has also important consequences in the Fourier domain. The microphone located at a fixed distance r, instead of measuring a signal which is flat in the frequency domain and with linear phase, would measure the Fourier Transform of Eq. (5.6), which is

$$\begin{aligned} G_2(\omega t_a) &= \frac{1}{\sqrt{2\pi}}\int_{-\infty}^{\infty} d\tau\, e^{i\omega\tau}G_2(r,\tau) = \frac{1}{\sqrt{8\pi}}\times \\ &\times \left[J_0(\omega t_a)\left[2\log 2 - 2\log(\omega t_a) + i\pi\right] - 2H_0^{(1,0)}\left[1, -\frac{1}{4}(\omega t_a)^2\right]\right] \end{aligned} \tag{5.8}$$

[1] In particular, it can be used to show that afterglow is a phenomenon present in all cases where D is even, and absent where D is odd.

where J_0 is the $0th$ order Bessel Function,

$$H_0^{(1,0)}[1,z] := \frac{\partial H_0[\alpha,z]}{\partial \alpha}\Big|_{\alpha=1}, \tag{5.9}$$

and $H_0[\alpha,z]$ is the *regularized confluent hypergeometric function*. Note that the Green's function in the frequency domain Eq. (5.8) depends on the frequency, position of the listener, and sound speed, only via the combination ωt_a. We observe that the amplitude of G_2 decreases abruptly for $\omega t_a \ll 1$, and in an almost linear fashion in the opposite regime $\omega t_a \gg 1$. On the other hand, the phase of G_2 is linear in a very good approximation; it shows indeed a slight sub-linear dependency.

It is remarkable that G_2 is, to a very good approximation, a minimum-phase function. Although we do not have an analytic proof, it can be obtained a plot of $g_2(t)$ and the associated minimum-phase function (computed numerically via homomorphic methods [Proakis & Manolakis (1998))]. In control theory and signal processing, a linear, time-invariant system is said to be minimum-phase if the system and its inverse are causal and stable [Smith (2007)]. As remarked in the introduction, this is a very important property which implies that the inverse of g_2 can be computed safely. This in turn implies that, if desired, it is possible to perform 2D simulations and *equalize* them by convolving with the inverse of g_2. This would erase the afterglow phenomenon, making microphones in 2D record signals that look like passing delta-functions, in the same way that happens in 3D.

5.3.2 Green's Function in 3D

Although the results in 3D are very well-known, as a matter of check, let us rederive them from Eq. (5.5). Using spherical coordinates with respect to axes aligned with $\mathbf{r}$, the integral Eq. (5.5) becomes:

$$\begin{aligned} g_3(r,\tau) &= \frac{u(\tau)c}{(2\pi)^3}\int_0^\infty d|\mathbf{k}|\,|\mathbf{k}|^2\int_0^{2\pi}d\phi\int_0^\pi d\theta\,\sin\theta\,\frac{\sin(|\mathbf{k}|c\tau)}{|\mathbf{k}|}e^{i|\mathbf{k}||\mathbf{r}|\cos\theta} \\ &= \frac{u(\tau)c}{2\pi^2|\mathbf{r}|}\int_0^\infty d|\mathbf{k}|\,\sin(|\mathbf{k}|c\tau)\sin(kr) \\ &= c\,u(\tau)\,\frac{\delta(c\tau-r)}{4\pi r}. \end{aligned} \tag{5.10}$$

The details of the integration steps can be found, for example, in Barton [Barton (1989)]. This is the very well-known result that an impulsive delta-source creates a sound field where the energy is concentrated in an infinitely thin shell the radius of which increases at the speed of sound; pressure and velocity is zero outside the shell.

5.4 Numerical Source Generation

Sound propagation in enclosures is a very complex phenomenon since the definition of boundary conditions complicates the formulation of the problem. The solution of the boundary value problem is not possible to be analytically achieved, therefore, numerical simulations arises as an alternative for sound predictions. One of the common methods in room acoustic applications are the wave-methods in the time domain since these methods are based on the motion equations that, in the case of sound propagation in enclosures, are the wave equation (see Sec. 2.2 for more details).

As mentioned in Sec. 2.3, the computation of the acoustic response in closed scenarios becomes one of the main topics in room acoustics. The mathematical foundations derived from this specific physical problem define a set of PDE that control the effects of the sources, the wave propagation and the boundaries of the enclosure. To computationally solve any PDE, it is necessary to discretise the simulated domain, consequently, the PDE system turns into an algebraic system of update equations that can be easily solved. Numerical simulations are commonly used in the low frequency range since in room simulations the wave behavior, such as diffraction, is only observed in a small acoustic range of wavelengths that typically goes from $0.1-1$ m. The accuracy of these methods is strongly related to the size of the mesh cells. For example, in FDTD it is demanded at least $N_\lambda = 10$ cpw (i.e 10 cells per maximum wavelength simulated) for obtaining acceptable results. Due to the discretization, it is essential to give some approximation to the Dirac delta source while it is defined as a singularity in the space and/or time making the numerical simulations completely unstable. Any approximation, no matter which, must keep a flat spectrum in the low frequency range as well as Dirac delta function.

For example, the Gaussian pulse which is commonly used in numerical simulations, fixes the amplitude with a parameter γ. In the time domain, the amplitude of the waveform is given by

$$s(t) = \delta(t-t_0) \sim Ae^{-[(n-n_0)\Delta t]^2/2\gamma}\,, \tag{5.11}$$

where $A = 1$ is the maximum amplitude, and γ is the pulse half-duration at the time $1/e$. One important property of these type of sources is that they transform into Fourier space keeping the same form than the temporal signal Eq. (5.11) but with a pulse half-duration of $1/\gamma$. Consequently, if we generate a Gaussian pulse with a short half-duration time, it would have a long decay to zero in the Fourier space. Therefore, it could be interesting to consider this type of pulses as a proper approximation of the Dirac delta source, since the amplitude of the spectrum in the low frequency range would be almost constant.

In figure 5.1 (left), we illustrate in the temporal domain either a Dirac delta source (up) or a numerical Gaussian pulse with $\gamma = 200$ (down). We fixed $\gamma = 200$, $n_0 = 80$ and $\Delta t = 1/16000$ and the numerical δ was obtained converting $t \to n\Delta t$. With these assumptions, we generated a thin Gaussian pulse (see in Fig. 5.1

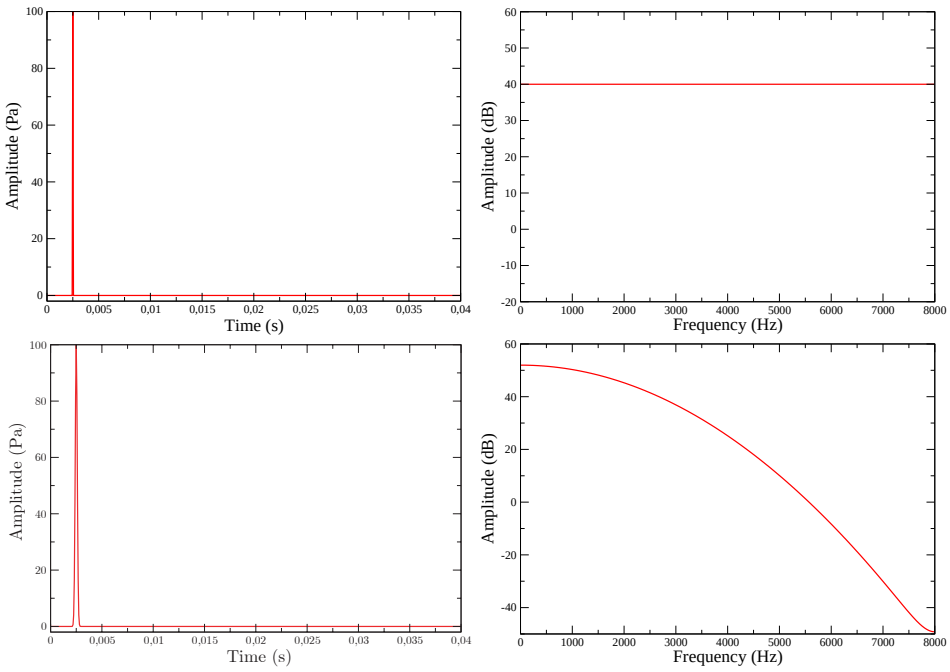

Figure 5.1: (Left) Numerical implementations of different unit impulse signals in the time domain. The x-axis represents the discrete time step n and the y-axis plots the normalized amplitude. (Right) Frequency spectrum of the signals where the x-axis represents the frequency and the y-axis is the modulus between the real and the imaginary part of the transformed pulse. In all the cases, we fix $\Delta t = 1/16000$ s and $n_0 = 80$: (Up) Dirac delta source; (Down) Gaussian pulse with $\gamma = 200$

down and left) observing that the Fourier spectrum of the signal transform into a thick Gaussian that can be considered almost flat from 0 to 2000 Hz (see in Fig. 5.1 down and right). Therefore, the computation of impulse responses of the acoustic field in the low frequency bandwidth is guaranteed while Gaussian pulses are chosen to approximate the Dirac delta function. Conversely, the amplitude plotted from $f > 2000$ Hz exhibits a linear decay that goes from 40 to 5 dB and appears in the range of frequencies $2000 < f < 5000$ Hz (see in figure 5.1 right and down). This behavior is far from the flat spectrum of the transformed delta function plotted in Fig. 5.1 (right and up). In fact, the most important drawback of Gaussian pulses is that parameter γ is not directly related to the frequency, f, difficulting the control of the total amount of energy emmited by the source.

In order to improve this situation, we present the numerical analysis of

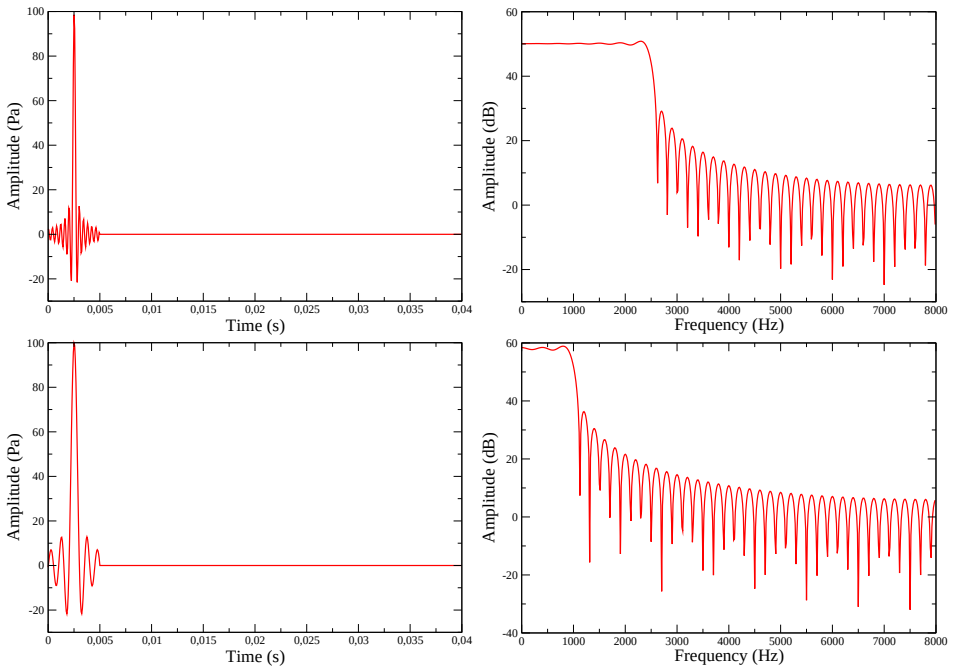

Figure 5.2: (Left) Numerical implementations of a *sinc*-function in the time domain. The x-axis represents the time step n and the y-axis plots the normalized amplitude. (Right) Frequency spectrum of the signals where the x-axis represents the frequency and the y-axis is the modulus between the real and the imaginary part of the transformed pulse. In all the cases, we fix $\Delta t = 1/16000$ s and $n_0 = 80$: (Up) *sinc*-function with $f = 2500$ Hz; (Down) *sinc*-function with $f = 1000$ Hz.

another representation of the unit impulse signal which is the *sinc*-function, and its explicit form is

$$s(t) = \delta(t - t_0) \sim \frac{\sin(2\pi f(n - n_0)\Delta t)}{2\pi f(n - n_0)\Delta t} \,. \tag{5.12}$$

For infinite signals, function (5.12) has a perfectly flat frequency spectrum since it transform in the Fourier space to the step function. The size of the step is fixed by the frequency f. Therefore, we would ideally control the total amount of energy through the physical parameter, f. Nevertheless, in real simulations the radiation of the unit impulse signal is limitated in the time introducing changes in the Fourier transform.

In Fig. 5.2, we illustrate two low-frequency approximations of a windowed *sinc*-function. All the sources are represented in both, the temporal (left) and the frequency (right) domain. As in the other pulses, $\Delta t = 1/16000$ s, $n_0 = 40$.

Moreover, we study two different values of the frequency, $f = 2500$ Hz (up) and $f = 1000$ Hz (down). In these cases, we constrain the source only radiating during a certain time, $n_t = 80$.

The effects of windowing the *sinc*-function are observed in Figs. 5.12 (right). Note that although it appears a residual energy for frequencies greater than f, the decay of the energy in both cases, is faster than in the Gaussian spectrum. Observe that this function has a perfectly flat frequency spectrum, instead of the Gaussian pulse which spectrum is approximately flat. Another remarkable fact is the flexibility of Eq. (5.12) since the amplitude frequency bandwidth is easily fixed through the frequency, f.

5.4.1 Soft Sources

Once approximated the Dirac Delta function, we are ready to study the different manners to introduce a source in FDTD or PSTD schemes. Typically, there exist three different types of sources: the hard, the soft and the transparent sources. In this section the two first types of sources are analyzed in detail, whereas the transparent source has not been considered for two reasons: firstly, they are defined in staggered meshes and, in this chapter, the source propagation analysis has been treated with non-staggered algorithms. Secondly, their formulation is rather complicated while it needs to store auxiliary quantities increasing considerably the computational cost of the algorithms.

On the one hand, the soft sources are one of the most common alternatives implemented in numerical simulations. There are many references that use soft sources in different fields such as electromagnetisms, acoustics, aeroacoustics or room acoustics applications. In this case, the impulse generation is obtained by introducing an additional term in the PDE system. In Sec. 2.2.3, we presented the analytical formulation of the sound sources generation for either the wave equation (2.36) or the Euler equations (2.33). For both formulations, the discrete pressure update equation (PUE) of a source node is given by

$$p|^{n+1}_{source} = \mathrm{PUE} + s|^n \ , \tag{5.13}$$

where PUE is obtained from any PSTD or FDTD algorithm (see Chap. 4) and $s|^n$ is defined as a multivalued discrete functions which form strongly depends on the PDE used in the simulation. For example, Eulerian algorithms straightforwardly define $s|^n$ from the analytical equation (2.33) reading as

$$s|^n = \begin{cases} \displaystyle\sum_{i=0}^{n} 100 \left[\frac{\sin(2\pi f(i-n_0)\Delta t)}{2\pi f(i-n_0)\Delta t} \right] \Delta t & \text{if } n \leq n_t, \\ s|^{n_t} & \text{if } n > n_t. \end{cases} \tag{5.14}$$

Observe that $s|^n$ is the low-frequency discrete representation of Eq. (2.33) , where $s(t)$ was represented with the temporal integral of the Dirac delta function. Moreover, in order to control the energy of the source generation, it is

convenient to limitate the radiation of the unit impulse signal by emitting only during a finite time $n_t > n_0$. Similarly, the discrete formulation of these type of sources applied to the wave equation are directly derived from the analytical equation (2.36). Therefore, the soft-source update equation is obtained from the PUE, adding the source term $s|^n$ as follows

$$s|^n = \begin{cases} 100\left[\frac{\sin(2\pi f(i-n_0)\Delta t)}{2\pi f(i-n_0)\Delta t}\right] & \text{if } n \leq n_t, \\ 0 & \text{if } n > n_t. \end{cases} \tag{5.15}$$

It is worth mentioning the fact that this source generation is based on the physical assumptions explained in Sec. 2.2.3. We will see in the next section, that this is the main difference between hard and soft sources, since the first ones use a completely different update equation. Finally, we note that the soft-source node does not influence in the medium since travelling sound waves pass through the source node without being diffracted due to the impulse radiation.

5.4.2 Hard Sources

On the other hand, the hard source is defined independently of the algorithms used for the propagation nodes. It means that the numerical representation of the impulse signal needs a pressure update equation completely different than the propagation scheme. In fact, this is one of the main difference between the hard and the soft sources since the last ones are introduced in the numerical motion equations. The explicit form of a node which is represented by a punctual hard source reads as follows:

$$p|^n_{source} = 100\left[\frac{\sin(2\pi f(n-n_0)\Delta t)}{2\pi f(n-n_0)\Delta t}\right] \quad \text{if } n \leq n_t \ , \tag{5.16}$$

In the Euler equations, note that only the pressure update equation is replaced by Eq. (5.16) since the update equations for the velocity keep employing the discrete mass equations of the Euler formulation, Eqs. (2.12)-(2.14). Likewise, the source generation during a finite time, n_t, is obtained by replacing the impulse emission by $p|^n_{source} = 0$ when $n \geq n_t$, ensuring that $p|^{n_t-1}_{source}$ is close to 0 just to get an smooth transition between the different assignations of the source node. We should note that once we use a hard source to represent a unit impulse signal in Eulerian simulations, there is no possibility to replace Eq. (5.16) by the PUE of any algorithm, even for perfectly continuous transitions at the critical time step n_t (i.e. $p|^{n_t}_{source} = 0$). Hence, the source node of the Eulerian simulation always updates its pressure value, $p|^{n+1}$ using different expressions than those derived from FDTD or PSTD methods. Therefore, for $n \geq n_t$, the punctual source acts as a periodic boundary node diffracting whole the acoustic field that strikes on it.

Conversely, if the discrete wave equation is used, the hard source node can be replaced at $n = n_t$ by the propagation algorithm keeping the simulation perfectly

stable and accurate. This fact gives an advantage to the wave equation, since once the source node has emmited all the input signal, it can be transformed into a propagation node avoiding the discontinuity produced due to hard source implementation.

5.5 Numerical Implementations

We have seen that there are different manners to generate proper unit impulse signals, depending on the PDE chosen to numerically solve the room impulse response. In this Thesis, the analysis of the numerical source propagation has been done by using FDTD (see in Sec. 4.3) and PSTD (see in Sec. 4.6) methods. Furthermore, we also compare the sound source propagation by using either the formulations of the Eulerian or wave algorithms.

On the one hand, In Chap. 4 we rewrote the original staggered FDTD and PSTD Eulerian algorithms by converting into their centered extension with exactly the same accuracy, stability and dispersion error than the staggered ones. The acoustic quantities, $(p, \mathbf{v})$, were defined at the same time, n, and position (i, j, k). In FDTD, the partial derivatives of the PDE were obtained by combining the forward and the backward finite difference operators leading to a second order accuracy scheme in time and space. Remark that the numerical scheme, Eq. (4.22) preserves either the Courant stability number, Eq. (4.21), or the dispersion relation, Eq. (4.20), obtained with the classical leap-frog scheme, Eq. (4.16). Similarly, the PSTD algorithm, Eq. (4.38), can be directly obtained applying to the temporal derivative the same methodology used in FDTD algorithms, while the spatial derivatives were computed with the spectral derivative, Eq. (4.14) (see Sec. 4.2 for more details). It is worth emphasysing the convenience of the non-staggered formulations for the numerical Eulerian algorithms since they are less restrictive in the mesh generation than the staggered ones.

On the other hand, algorithms based on the wave equation are originally defined in centered meshes since they only compute the acoustic pressure. In Sec. 4.3, we presented the explicit form of the FDTD 3D algorithm Eq. (4.23), which stability Courant number and dispersion error are exactly the same than for the leap-frog scheme. Similarly, the PSTD 3D algorithm for the discrete wave equation, Eq. (4.39), is presented in Sec. 4.6, also showing that they preserve the stability and accuracy than the Eulerian PSTD formulations.

Once defined the non-staggered algorithms, we are ready to study the 2D and 3D propagation of the approximated unit impulse signal chosen to simulate computationally the Dirac delta function. As we said before, the Dirac delta function must be approximated for stability reasons. One of the proper possibilities is the *sinc*-function, since it represents the best choice to characterize the Dirac delta source at low frequencies. Furthermore, the way of introducing the input signal in the numerical simulation generates different possibilities that would affect the sound propagation within the room.

5.5.1 2D Results

In this section, we show a comparative analysis of the numerical source propagation using 2D FDTD and PSTD algorithms. In both methods, we present experimental data of the impulse-signal propagation obtained in numerical experiments. In all the simulations done, the experimental setup is defined in a 2D centered mesh of 2500×2500 nodes and the time discretization is fixed to $\Delta t = 1/16000$ s, no matter which method is used. Independently of the type of source, we use a *sinc*-function with $f = 2500$ Hz, $n_0 = 40$ and $n_t = 80$ at node $(1750, 1750)$. Moreover, we locate receivers at $R_1 = 1$, $R_2 = 3$ and $R_3 = 5$ m from the source measured along the axis and the diagonal. The numerical data are compared to the expected propagation of a analytical *sinc*-function derived from Eqs. (5.6) and (5.8).

FDTD Algorithms

For these experiments, we use the 2D extension of the non-staggered leap-frog scheme, Eq. (4.22), that computes all the acoustic quantities, p and $\mathbf{v} = (v_x, v_y)$, and the discrete-pressure wave equation (4.23) that only calculates the pressure. In both algorithms, the spatial discretization δ is fixed through Δt and the Courant stability number, which in this case is $S = 1/\sqrt{2}$. With these assumptions, the receiver locations R_1, R_2 and R_3 m correspond to 33, 98 and 163 nodes of distance since $\delta = 0.030052$ m.

On the one hand, in Fig. 5.3, a), b) and e), f), we show the results obtained with the soft source generation, Eq. (5.13), using the two different representations of the source term, $s(t)$, defined in Eqs. (5.14) and (5.15). The solid lines correspond to R_1, the dashed ones, R_2 and dotted lines, R_3 along the axis or the diagonal. Moreover, the grey and black lines represent the analytical and numerical results, respectively.

In both algorithms, the accuracy of the results is remarkable in the whole frequency range of the signal. Observe that the numerical results fit perfectly with the analytical curve from 0 to approximately 1500 Hz. For the rest of the frequency range, the accuracy decreases leading to numerical errors that can also be considered more than acceptable. Another remarkable consequence is observed when the results obtained along the axis are compared to those measured in the diagonal. As expected, the last ones exhibit slightly better accuracies at high frequencies due to the fact that there is no dispersion error at this orientation.

On the other hand, in Fig. 5.3 (c) and d), g) and h)) we illustrate the results obtained by using the hard source generation with either the Euler or the Wave algorithms. In this case, the numerical curves differ from the analytical ones in almost all the frequency range, since this manner to generate the impulse is not derived from the analytical formulation of the source generation.

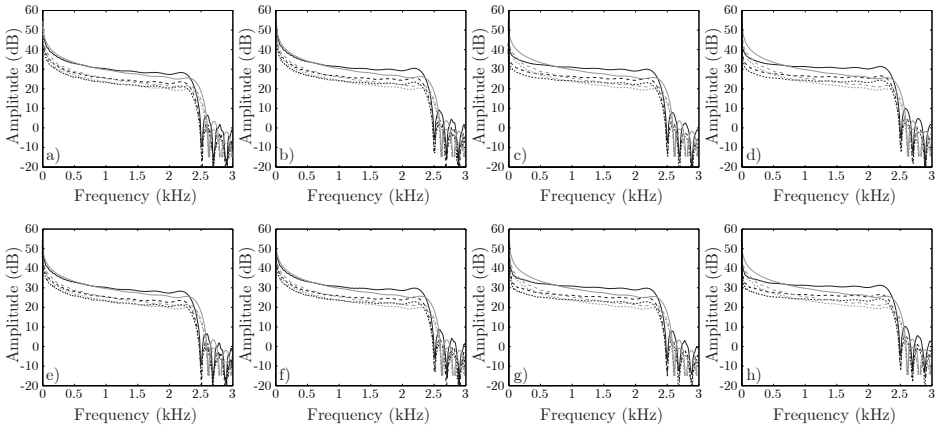

Figure 5.3: Numerical results in 2D FDTD experiments. Black lines represents the numerical results, whereas grey lines are the analytical data. R_1, R_2 and R_3 is represented by solid, dashed and dotted lines, respectively. (Up) Simulations done with the Eulerian algorithm, Eq. (4.22). Figures a) and b) plot the results along the axis and the diagonal respectively, using the soft source generation. Figures c) to d) show the results obtained with the hard source representation. (Down) In this case, the simulations use the discrete wave equation (4.23) for the propagation nodes. From e) to f), the results of the soft source along the axis and the diagonal are represented. Finally, from g) to h) we show the results obtained with the hard source generation.

PSTD Algorithms

Likewise, we present a complete analysis of the numerical sound source propagation using PSTD methods that, in the case of the discrete wave equation, it is analyzed for the first time in the acoustics. As well as FDTD methods, we use both, the Eulerian and the Wave algorithms, Eqs. (4.38) and (4.39) respectively. For both formulations, we use the maximum Courant stability number allowed by PSTD methods which is $S = \frac{2}{\pi\sqrt{2}}$ fixing the spatial discretization to $\delta = 0.047056$ m. For this method, the nodal distance of the receivers R_1, R_2 and R_3 are 21, 64 and 106. Note that we need less nodes than in FDTD algorithms since δ_{PSTD} is $\pi/2$ greater than δ_{FDTD}.

In general, the results obtained in PSTD methods are similar than FDTD (see Fig. 5.3). As mentioned, the soft source generation gives better results than hard source generation since the soft ones are based on the mathematical and physical foundations of the source generation (see in Sec. 2.2.3). On the other hand, there is no difference between the results obtained along the axis and the diagonal, since the dispersion error in PSTD method is non-angular dependent. Furthermore, it is worth mentioning that in PSTD simulation, a non-physical

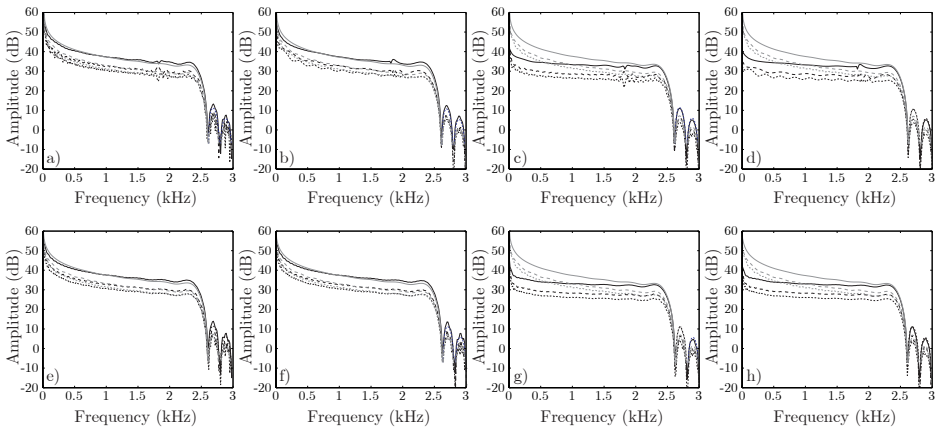

Figure 5.4: Numerical results in 2D PSTD experiments. Black lines represents the numerical results, whereas grey lines are the analytical data. R_1, R_2 and R_3 is represented by solid, dashed and dotted lines, respectively. (Up) Simulations done with the Eulerian algorithm, Eq. (4.38). Figures a) and b) plot the results along the axis and the diagonal respectively, using the soft source generation. Figures c) to d) show the results obtained with the hard source representation. (Down) In this case, the simulations use the discrete wave equation (4.39) for the propagation nodes. From e) to f), the results of the soft source along the axis and the diagonal are represented. Finally, from g) to h) we show the results obtained with the hard source generation.

artifact appears at $f = 1900$ Hz that is produced due to the use the punctual sources. We will see in 3D results that this error becomes critical suggesting to change the manner of generating the impulse. Nevertheless, in 2D this error can be considered negligible since the accuracy in PSTD is sensibly improved in the measures done using soft sources. Similarly, the numerical results of the hard source propagation in PSTD do not correspond to the analytical behavior since its formulation is not based in any physical assumptions.

5.5.2 3D Results

In what follows, we present the numerical results of the 3D experimental setup defined independently of the numerical method employed. As for 2D setup, we fix $\Delta t = 1/16000$ s and a *sinc*-function with $f = 2500$ Hz, $n_0 = 40$ and $n_t = 80$. For these simulations, a 3D mesh of $(150 \times 150 \times 150)$ nodes is required locating the receivers R_1, R_2 and R_3 at 1, 2 and 3 m. Finally, the numerical data is compared with the Green's function of a *sinc*-function straightforwardly derived from Eq. (5.10).

FDTD Algorithms

For these simulations we fixed $S = 1/\sqrt{3}$ and $\delta = 0.0368$. Consequently, R_1, R_2 and R_3 are located at nodal distance of 27, 54 and 81 from the source. In Fig. 5.5 we show the remarkable accuracies obtained with both types of sound generation. In this case, the spectrum of energy is almost flat in all the simulated range preserving high accuracies at frequencies greater than 2000 Hz.

Surprisingly, the results obtained with the hard source generation show that it can be used for computing the impulse response of enclosures, however its formulation is not based in any physical representation.

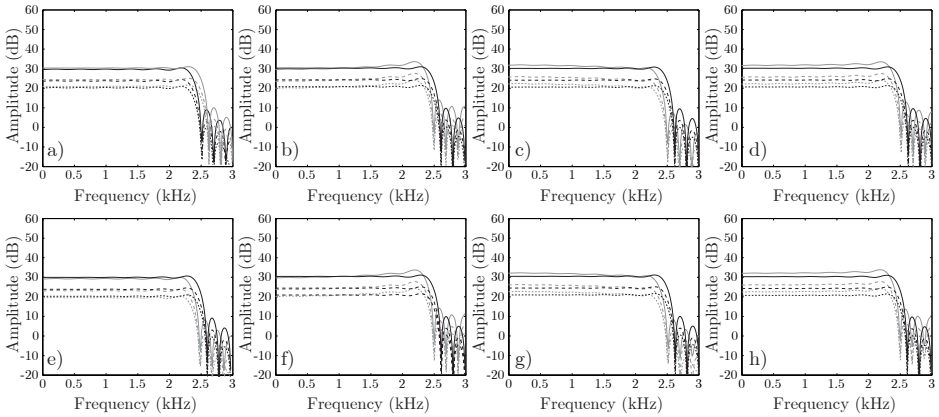

Figure 5.5: Numerical results in 3D FDTD experiments. Black lines represents the numerical results, whereas grey lines are the analytical data. R_1, R_2 and R_3 is represented by solid, dashed and dotted lines, respectively. (Up) Simulations done with the Eulerian algorithm, Eq. (4.22). Figures a) and b) plot the results along the axis and the diagonal respectively, using the soft source generation. Figures c) to d) show the results obtained with the hard source representation. (Down) In this case, the simulations use the discrete wave equation (4.23) for the propagation nodes. From e to f, the results of the soft source along the axis and the diagonal are represented. Finally, from g to h we show the results obtained with the hard source generation.

PSTD Algorithms

The numerical experiments for PSTD use a 3D mesh of $150 \times 150 \times 150$ nodes and have been carried out with $S = \frac{2}{\pi\sqrt{3}}$ and $\delta = 0.0578$. The source is located at the center of the mesh (i.e. $(75 \times 75 \times 75)$). In this cases the receivers R_1, R_2 and R_3 are located at the nodal distance 17, 34 and 51 nodes. In Fig. 5.5, it is plotted the numerical results compared to the analytical data.

Observe that in this case, all the results obtained, no matter which PSTD algorithm or punctual source generation is used, show errors sufficiently relevant to consider them completely unacceptable. More specifically, this error becomes critical in measures done along the axis of the source node.

In Fig. 5.7, we show the temporal signals of the receiver R_2 using the punctual soft source generation for the Eulerian algorithms. In the left, we plot the temporal signal measured in the axis observing that the aforementioned artifact is appeared during the emission of the source. Conversely, the temporal signal measured in the diagonal is not affected by this error since, as mentioned, it only affects along the axis of the source node (see in Fig. 5.7 (right)).

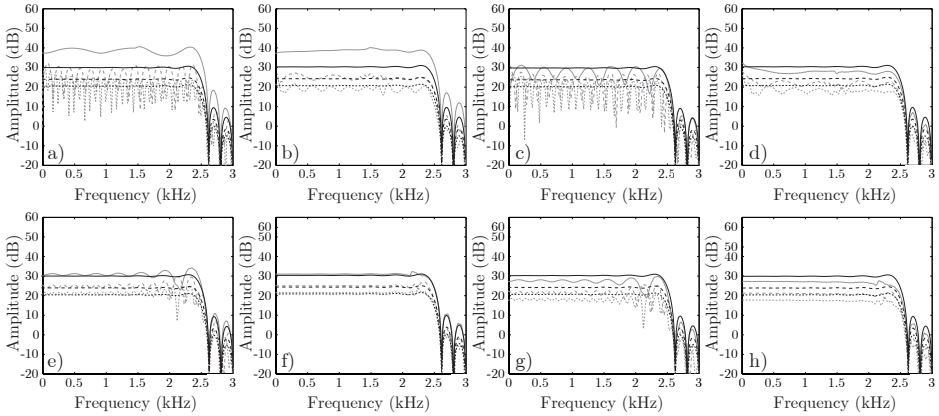

Figure 5.6: Numerical results in 3D PSTD experiments. Black lines represents the numerical results, whereas grey lines are the analytical data. R_1, R_2 and R_3 is represented by solid, dashed and dotted lines, respectively. (Up) Simulations done with the Eulerian algorithm, Eq. (4.38). Figures a) and b) plot the results along the axis and the diagonal respectively, using the soft source generation. Figures c) to d) show the results obtained with the hard source representation. (Down) In this case, the simulations use the discrete wave equation (4.39) for the propagation nodes. From e to f, the results of the soft source along the axis and the diagonal are represented. Finally, from g to h we show the results obtained with the hard source generation.

It is reported by Lee and Hagness [Lee & Hagness (2004)] that punctual sources introduce a numerical error that can be solved by defining a volumetric source called quadruplet source. In fact, the hard and the soft source generation are presented for the 1D and 2D Eulerian PSTD algorithms. In this case, the soft source generation is achieved through Eq. (5.13) by defining the source term, $s|^n$, as Eq. (5.15). Note that this representation does not correspond to the punctual soft source generation defined for the Eulerian algorithms in Sec. 5.4.1. On the other hand, the volumetric hard sources for either the Euler or the

Wave equations are implemented by using the expression Eq. (5.16), which is the same equation used for the punctual sources.

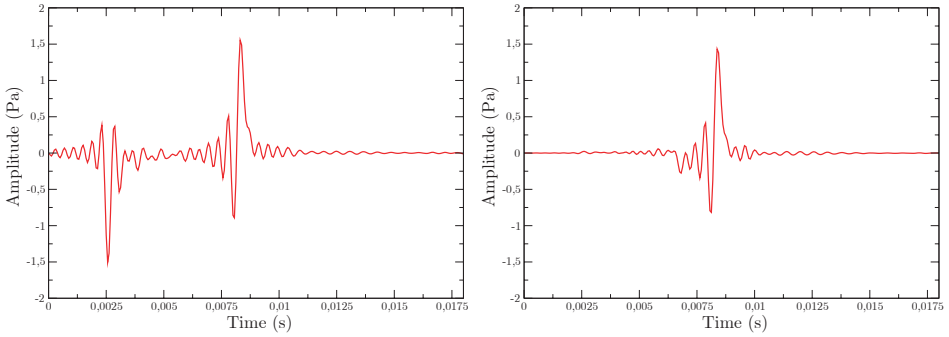

Figure 5.7: (Left) Impulse propagation at R_2 along the axis. Observe the artifact produced due to the emission of the source. (Right) Impulse propagation at R_2 along the diagonal. In this case, there is no error produced by the source generation.

In order to overcome the critical error obtained in the 3D PSTD simulations, we carried out several simulations using the volumetric sources. Basically, the idea consist on using more than one node for defining the source emission. More concretely, the source is defined by using a pair of nodes by each axis. Hence, In a 3D simulation, volumetric source is obtained with 6 source nodes leading to a numerical source of cubical shape. Moreover, we simulate either the Eulerian algorithm, Eq. (4.38), or the discrete wave equation (4.39) using both, the hard and the soft representation presented in Eqs. (5.16) and (5.15), respectively. In this case, the soft source generation for the Eulerian algorithm is also defined with $s(t)$ derived from the discrete-wave representation of the soft-source generation, thus Eq. (5.15).

In Fig. 5.8 we show the results obtained from the numerical experiments. On the one hand, the artifact of punctual source simulations is disappeared leading to smoother frequency spectra of the results. On the other hand, we observe for both algorithms that only the volumetric hard source generation simulate almost perfectly the behavior derived from the analytical expressions. Conversely, the results obtained with volumetric soft sources are far from those analytically expected in terms of the amplitude. We should remark that the volumetric soft sources in the Eulerian PSTD algorithm, Eq. (5.15), are not based on any physical assumption, instead of the punctual soft sources, Eq. (5.14). Therefore, it seems reasonable that these numerical sources do not behave as a physical source. Finally, we conclude that volumetric hard sources are, so far, the best choice in 3D PSTD simulations, although the soft source generation need to be improved since their results sensibly differs from the analytical curves.

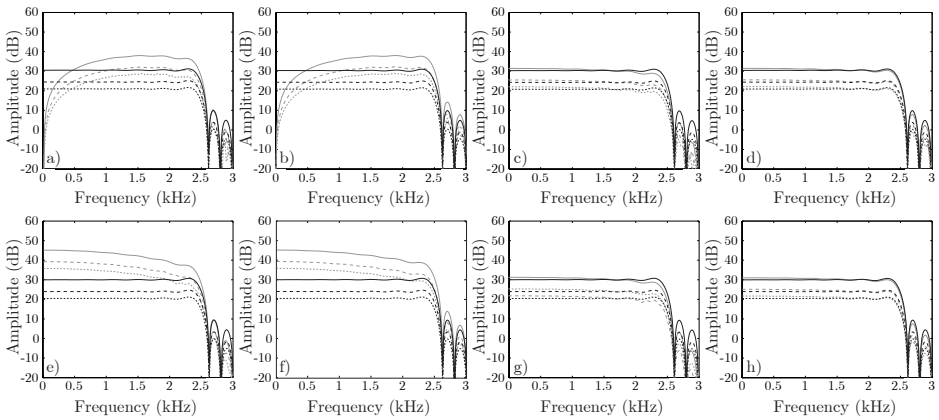

Figure 5.8: Numerical results in 3D PSTD experiments using volumetric sources. Black lines represents the numerical results, whereas grey lines are the analytical data. R_1, R_2 and R_3 is represented by solid, dashed and dotted lines, respectively. (Up) Simulations done with the Eulerian algorithm, Eq. (4.38). Figures $a)$ and $b)$ plot the results along the axis and the diagonal respectively, using the soft source generation. Figures $c)$ to $d)$ show the results obtained with the hard source representation. (Down) In this case, the simulations use the discrete wave equation (4.39) for the propagation nodes. From $e)$ to $f)$, the results of the soft source along the axis and the diagonal are represented. Finally, from $g)$ to $h)$ we show the results obtained with the hard source generation.

5.6 Conclusions

In this current chapter, we present a carefully analysis of the numerical source generation in FDTD and PSTD. Firstly, the mathematical formulation of the unit impulse propagation has been formulated either for the 2D and the 3D case (see in Sec. 5.3). In two dimensions, the afterglow phenomenon is observed leading to a different propagation than in 3D.

In Sec. 5.4, we discuss two of the main manners to approximate the Dirac delta source concluding that the *sinc*-function is the best choice to approach the unit impulse signal in the low frequency range. Moreover, we formulated either the soft or the hard source generation, observing that only the soft ones are based on physical background (see in Secs. 5.4.1 and 5.4.2).

In addition, we carried out different numerical simulations in order to compare the numerical results of the source propagation to the analytical data. On the one hand, the 2D results presented in Sec. 5.5 show that only the soft source representation obtains high accuracies, since these formulations are based on the physical assumptions. On the other hand, All 3D results exhibit high accuracies except those obtained in PSTD simulations using both, the

soft and the hard numerical sources. In Sec. 5.5.2 we observed that punctual source generates along the axis of the source node an artifact that critically affects to the numerical results. In order to overcome this situation, we also analyzed the volumetric sources that were created for solving this problem in the 2D PSTD Eulerian formulation [Lee & Hagness (2004)]. In this chapter, we extend this works to the 3D discrete wave and Eulerian formulation, providing an analysis that has been never done before. However, the best accuracies were observed in the results obtained by using the hard source generation. this fact is completely expected since the volumetric soft source generation is not based in any physical assumptions.

Finally, in the next chapter we present a complete analysis of different numerical implementations of the locally reacting model for FDTD and PSTD. The study of these particular boundary conditions methods in PSTD has never been treated before in the technical literature.

Chapter 6

Locally-Reacting Boundary Conditions

6.1 Introduction

In this chapter we overview the formulation of most common numerical BCs, based on the formulation presented in Sec. 2.3.1, for FDTD (see in Sec. 6.4) and PSTD (see in Sec. 6.5) methods. We perform different simulations, based on an experimental setup explained in Sec. 6.3, of several numerical BCs either for the Euler equations or the wave equation. The numerical results are compared with those obtained through the analytical relation, Eq. (2.42). Therefore, we discuss which boundary conditions are appropriate for room acoustics, since the locally reacting impedance behavior has to be simulated.

Conversely, the issue of impedance boundary conditions for PSTD has never been treated in the technical literature since only periodic BCs are suitable for PSTD simulations. In Sec. 4.9 we present an efficient way to eliminate this critical error defining PML beyond the impedance boundary nodes. It opens the possibility of using pseudo-spectral techniques in room acoustics and other related fields of research. Hence, in Sec. 6.5 we present for the first time impedance boundary conditions for the Eulerian and the wave PSTD formulation. The results obtained from these novel BCs are tested and validated by means of a multidimensional experiments. Finally, we extend their formulation to FDTD methods obtaining results as accurate as those presented in Sec. 6.4. Finally, in Sec. 6.6 we expose the conclusion of the Chapter.

6.2 Problem Overview

Over the past decade, many studies in the area of FDTD and DWM modelling of 2D and 3D acoustic systems have focused on reducing and/or compensating for the dispersion error. Recently, more attention has been given to the problem of formulating better numerical approximations of boundaries, and in particular

the obtention of locally-reacting boundaries. Generally, realistic boundaries can be approximated by locally-reacting ones even at narrow frequency ranges.

Basically, an impedance boundary assumes that the acoustic pressure and the outward normal direction of the particle velocity is related linearly by the acoustic impedance Z (see Sec. 2.3.1 for more details). If we assume that Z is defined as a real positive constant (i.e. locally-reacting BCs), the relation between the amplitude of the reflexion coefficient, R, and the acoustic impedance when a planar wave strikes on the wall is given by Eq. (2.42). It is worth mentioning that R depends strongly on the orientation of the planar waves.

Different equations arise by combining Eq. (2.41) and the mass conservation equation, Eq. (2.43), which are able to fit the time evolution of the acoustic quantities of an impedance boundary (see in Sec. 2.3.1 for more information).

The first contributions of FDTD impedance boundary conditions for either the lineralized Euler equations or the wave equation were presented by Bootledooren [Botteldooren (1995)] and Huopaniemi et al. [Huopaniemi et al. (1997)], respectively. These contributions served as an inspiration for the acoustics community, leading to a number of works that, in some cases, improve the initial results [Kowalczyk & van Walstijn (2007)].

In fact, we present different contributions of numerical BCs for either the Euler or the wave FDTD and PSTD algorithms that, even so, they have not been analyzed together, in order to get an objective analysis of the results. Thus, it would be very interesting for the room acoustics community to provide a fair comparative study between different numerical BCs.

6.3 Experimental Setup

In this section we define the experimental setup in order to test the accuracy of any numerical boundary conditions as a locally reacting ones when combined with FDTD or PSTD. The experimental setup used is inspired on Kelloniemi et al [Kelloniemi et al. (2005); Kelloniemi (2005)]. The system consists on a two dimensional rectangular interpolated mesh with a sound source located at $\mathbf{x}_s$. Many receivers, $\mathbf{x}_{\tau_\xi}$ and $\mathbf{x}_{\tau'_\xi}$, where $\xi = 1,2,3...$, are placed along the parallel lines τ and τ' as it is shown in Fig. 6.1.

Within the experimental setup of Fig. 6.1, two simulations are carried out: a first simulation in which a layer of boundary nodes, ∂V, is located in the middle; and a second free space simulation without the boundary layer. In both simulations the sound source $\mathbf{x}_s$ emits an unit acoustic impulse.

In the first simulation, sound pressure signals are measured in all the receiver's positions, $\mathbf{x}_{\tau_\xi}$, $\xi = 1,2,3....$ This signals contain not only the direct sound, but also the sound reflected from the boundary, ∂V. In the second simulation (in free space), sound pressure signals are measured both at $\mathbf{x}_{\tau_\xi}$ and at $\mathbf{x}_{\tau'_\xi}$. Therefore, the direct signal component radiated from the sound source to the receivers $\mathbf{x}_{\tau_\xi}$ measured in the first simulation can be erased by using the data

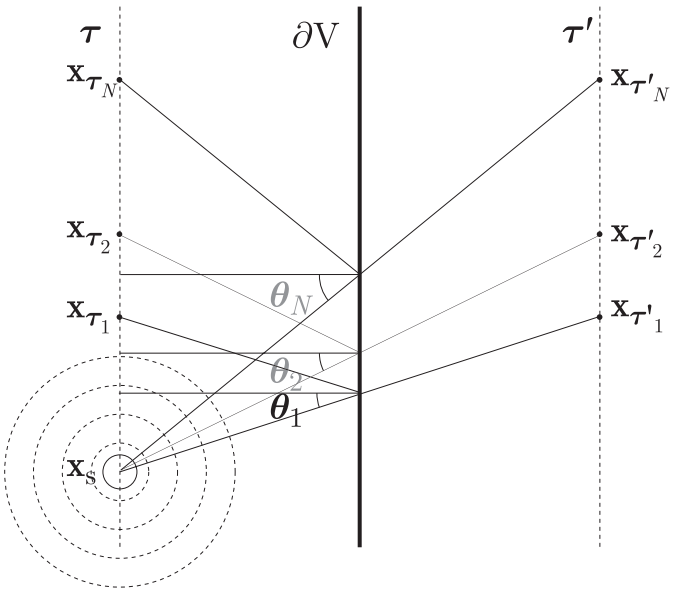

Figure 6.1: An illustrative representation of the experimental setup: The source is located at $\mathbf{x}_s$, the receivers are situated over the lines τ and τ', finally, ∂V represents the boundary layer which is at the same distance from $\mathbf{x}_\tau$ to $\mathbf{x}_{\tau'}$.

obtained in the unbounded second simulation.

In order to fit the reflection factor, the resulting frequency responses obtained from the first simulation (once the direct sound is eliminated) at the receivers, $\mathbf{x}_{\tau_\xi}$, are compared to the reference signals obtained from the unbounded simulation at the mirror locations $\mathbf{x}_{\tau'_\xi}$.

To sum up: for each receiver $\mathbf{x}_{\tau_\xi}$ we get a value of the reflection factor by comparing the spectra of the signals measured at the receiver location $\mathbf{x}_{\tau_\xi}$ and at the mirror location $\mathbf{x}_{\tau'_\xi}$. Due to the fact that the different receivers correspond to different angles of incidence, we can compute in a single numerical experiment, the absolute error,

$$\varepsilon = 20\log_{10}\|R_{th} - R_{meas}\|\,, \tag{6.1}$$

for any frequency and angle, just by comparing the numerical reflection factor R_{meas} with the theoretical predictions R_{th}, Eq. (2.42). Finally, the right half of the Hann window function has to be used for windowing the last half of the signals to avoid the truncation error in calculation of the spectra.

In this particular experiment, a two dimensional domain V of 2000×2000 nodes is generated with a boundary layer located at the nodes $(i, 1000)$. In this

case the sound source is located at node $(520, 900)$. Moreover, the input signal is an acoustic impulse approximated by[1] the hard source, Eq. (5.16), Note that this function has a flat frequency spectrum from 0 to f. All the cases are tested with $f = 2500$ Hz, $n_0 = 40$, $n_t = 80$, $\Delta t = 1/16000$ s and the minimum value of the Courant stability number for a 2D simulation, given by the algorithm employed for the propagation nodes.

The distance between the source and the receiver is varied between 0 and 800 spatial sampling intervals, corresponding to the incident angle $\theta \in [0, 80°]$, approximately. It is true that angle values are not distributed homogeneously under this experiment; however, for illustrative purposes, unknown angles are linearly interpolated. Finally, the simulation is run for 1024 time steps in order to avoid the numerical rebounds which generate the exterior boundaries and which may produce some disturbances in the analysis of the spectra.

6.4 Boundary Conditions in FDTD Methods

Different approximations can be achieved depending on the election of the PDE system chosen to be numerically solved. For example, if the Euler equations are employed, the numerical treatment of the boundary conditions is strongly influenced by the type of mesh used in the discretization of the space. If an staggered mesh is demanded (see Fig. 4.1 (right)), the boundary layers can only be defined at velocity nodes, [Botteldooren (1995)]. Therefore, the numerical boundary conditions are obtained with only one update equation for the velocity. On the other hand, if a centered mesh is used (see Fig. 4.1 (left)), the boundary layers are defined either pressure and velocity nodes. In this case, the numerical boundary scheme needs an update equation for pressure or velocity. Conversely, if the wave equation is approximated, the numerical boundary conditions are obtained with a pressure update equation since it is only computed the information for the acoustic pressure, [Huopaniemi et al. (1997); Kowalczyk & van Walstijn (2007)].

In this chapter, we present a complete analysis of the most common numerical boundary conditions derived from the analytical expressions presented in Sec. 2.3. In the next section, we formulate the numerical staggered BCs for the Euler equations [Botteldooren (1995)] and we tested comparing the numerical experiments with the analytic relation, Eq. (2.41). In Sec. 6.4.2, two different formulations of the BCs for the wave equation are presented and studied in detail. Finally, in the last section we expose the conclusions.

6.4.1 Boundary Conditions for the Euler Equations

In 1995[Botteldooren (1995)], it was presented a numerical expression of general boundary conditions for the staggered leap-frog scheme, Eq. (4.16). This

[1] For Eulerian algorithms we use the soft source representation, Eq. (5.13), to simulate the unit impulse signal

algorithm only requires to define a velocity update equation for the boundary layer, since it is defined in a staggered mesh (see Sec. 4.3 for more details). The velocity nodes which belong to ∂V (see Fig. 6.1), are governed by the analytical linear relation, Eq. (2.41), which linearly relates the normal component of the velocity and the pressure through the acoustic impedance Z of the material. The numerical equation derived from these assumptions is obtained by assuming an asimetric finite difference approximation for the space derivative. The resulting equation is capable of simulating either dependent or non-dependent frequency impedance BCs. In this section, we only study the cases when the acoustic impedance, Z, does not depend on the frequency. Moreover, although we focus the analysis on the leap-frog scheme, these boundary conditions can be directly combined with the family of algorithms presented in Sec. 4.4. The numerical equation of the local impedance velocity nodes is achieved by

$$v_x|_{i+1/2,j}^{n+1/2} = \gamma v_x|_{i+1/2,j}^{n-1/2} - \beta p|_{i,j}^{n} \,, \tag{6.2}$$

with

$$\begin{aligned} \gamma &= \frac{1 - Z/Z_{FDTD}}{1 + Z/Z_{FDTD}} \\ \beta &= \frac{1}{1 + Z/Z_{FDTD}} \\ Z_{FDTD} &= \frac{\rho\delta}{\Delta t} \,. \end{aligned} \tag{6.3}$$

Note that γ and β are adimensional constants which strongly depends on the acoustic impedance of the material. Since $Z \in [0, +\infty[$, it is more convenient to express the different boundary conditions by using the theoretic reflection factor, $R_{\text{th}} \in [-1, 1]$, as a parameter related with Z by Eq. (2.42) (see Sec. 2.3.1 for more details). The simulations have been carried out for values of $R_{\text{th}} = -1, -0.9, \ldots, 1$ ($\Delta R_{\text{th}} = 0.1$). Therefore, we compute the average error, ε, of the numerical measured reflection factor R_{meas} with respect to the theoretic reflection factor R_{th}, expressed in dB.

In what follows we will show and analyze the results obtained within the experimental setup defined in the previous section. The simulations were carried out with $\Delta t = 1/16000$ s and the maximum Courant stability number $S = 1/\sqrt{2}$. The results of the numerical experiments confirm the suitability of the boundary conditions given in Eq. (6.2) for room acoustic applications.

These results are illustrated in Fig. 6.2 . Each plot corresponds to the absolute error given by Eq. (6.1) as a function of the angle of incidence, θ, and the frequency. The error is plotted in a graded scale where black corresponds to errors of a few negative dBs whereas white corresponds to errors less than -40dB.

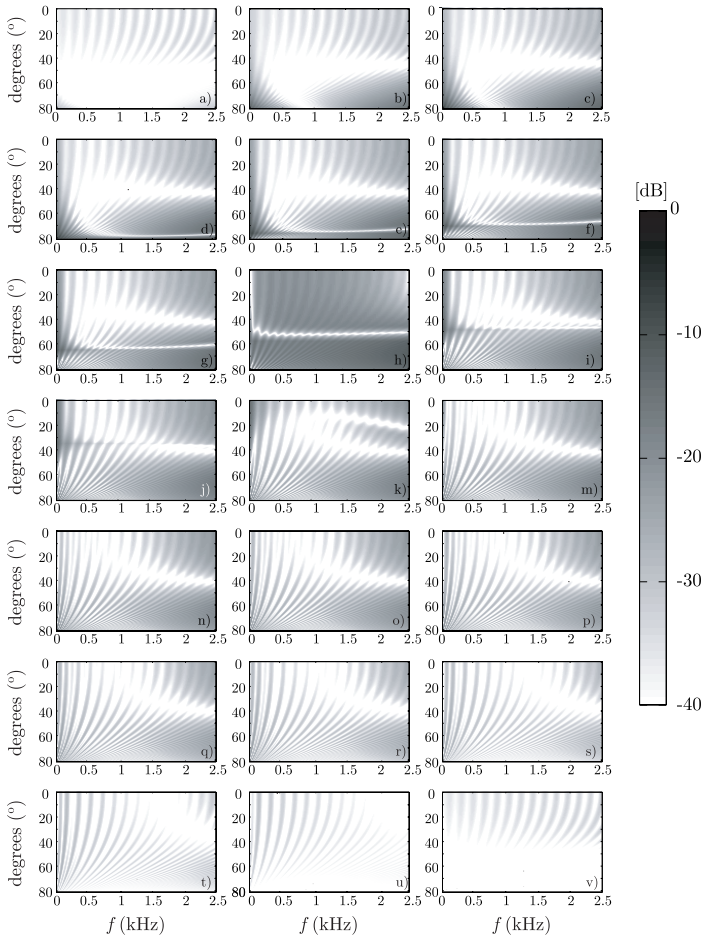

Figure 6.2: The absolute error in decibels for different values of the normal reflection coefficient R_n obtained with the numerical BCs, Eq. (6.2), combined with the leap-frog scheme. From up to down and left to right: a) $R_n = 1$, b) $R_n = 0.9$, c)$R_n = 0.8$, d) $R_n = 0.7$, e) $R_n = 0.6$, f) $R_n = 0.5$, g) $R_n = 0.4$, h) $R_n = 0.3$, i) $R_n = 0.2$, j) $R_n = 0.1$, k) $R_n = 0$, m) $R_n = -0.1$, n) $R_n = -0.2$, o) $R_n = -0.3$, p) $R_n = -0.4$, q) $R_n = -0.5$, r) $R_n = -0.6$, s) $R_n = -0.7$, t) $R_n = -0.8$, u) $R_n = -0.9$ and v) $R_n = -1$.

The label of each plot is the reflection factor for normal incidence, R_n, which fixes the value of the impedance Z in the numerical simulation via Eq. (2.42) with $\theta = 0$. Therefore for each value of R_n (i.e. of Z) the numerical experiment defined in Sec. 6.3 is performed and the absolute error is computed for different angles given by the receiver locations, $\mathbf{x}_{\tau_\xi}$, for all frequencies less than 2500 Hz.

The accuracy of the BCs is remarkable since the absolute error is smaller than $-30dB$ in almost all range of R_n for all frequencies and angles. Only for $R_n \to 0.3$, this error is increased homogeneously to $-20dB$ which is sufficiently small to consider it irrelevant. Although the agreements with the predicted values are excellent, it is worth emphasizing the fact that this BCs are defined in a staggered mesh. It means that the definition of a boundary layer is strongly constrained since it can only be defined at velocity nodes. In order to solve this problem, in the Sec. 6.5.2 we present a numerical BCs defined in a centered mesh. The results obtained with this novel method are very similar than those depicted in Fig. 6.2.

6.4.2 Boundary Conditions for the Wave Equation

The first approximation of the boundary conditions in room acoustics for the FDTD methods is presented by Huopaniemi et al. [Huopaniemi et al. (1997)]. Where the starting point appears in the definition of 1-D digital waveguide boundaries. One straightforward way tosecBC set BCs in digital waveguide mesh, is the structure in which each boundary node has only one neighbor. The simplest boundary conditions is the reflection coefficient. The difference equation for such boundary node is

$$p|_{i,j}^{n+1} = (1+R_n)p|_{i-1,j}^{n} - R_n p|_{i,j}^{n-1} \,. \tag{6.4}$$

We have chosen this boundary conditions because it has never been analyzed its two-dimensional locally-reacting behavior. For nodes which do not belong to ∂V, we chose the numerical formulation derived from the wave equation, Eq. (4.23) with a time discretization $\Delta t = 1/16000$ s and the maximum Courant stability number S allowed for the algorithm.

The results are presented in Fig. 6.3. Observe that only for $R_n \geq 0.8$ and $R_n \leq -0.6$ the Bcs, Eq. (6.4), gives values of the absolute error smaller than -20 dB. Conversely, for the rest of R_n, the absolute error is quite relevant since it is bigger than -20 dB. It is worth mentioning that highly absorbing materials are unusual in most real scenarios, i.e. room acoustics, where materials use to have at least an absorption coefficient α ($\alpha = 1 - ||R_n||^2$) which varies between 0 and 0.5. Under these circumstances, the results are most than acceptable for many purposes such as room acoustics, aeroacoustic, ...

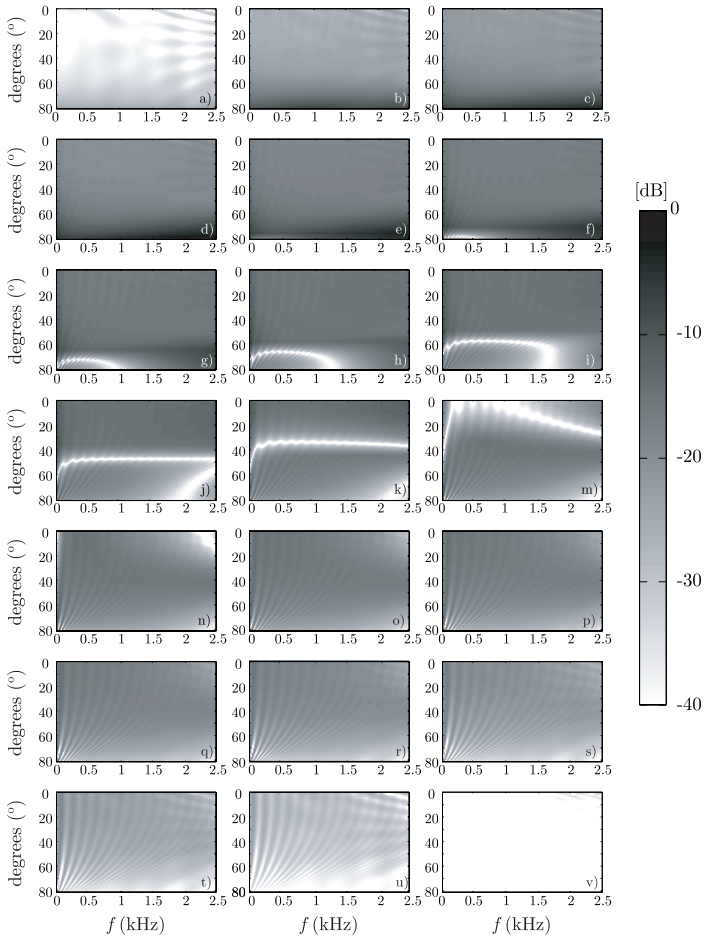

Figure 6.3: The absolute error in decibels for different values of the normal reflection coefficient R_n obtained with the numerical BCs, Eq. (6.4), combined with the leap-frog scheme . From up to down and left to right: a) $R_n = 1$, b) $R_n = 0.9$, c)$R_n = 0.8$, d) $R_n = 0.7$, e) $R_n = 0.6$, f) $R_n = 0.5$, g) $R_n = 0.4$, h) $R_n = 0.3$, i) $R_n = 0.2$, j) $R_n = 0.1$, k) $R_n = 0$, m) $R_n = -0.1$, n) $R_n = -0.2$, o) $R_n = -0.3$, p) $R_n = -0.4$, q) $R_n = -0.5$, r) $R_n = -0.6$, s) $R_n = -0.7$, t) $R_n = -0.8$, u) $R_n = -0.9$ and v) $R_n = -1$.

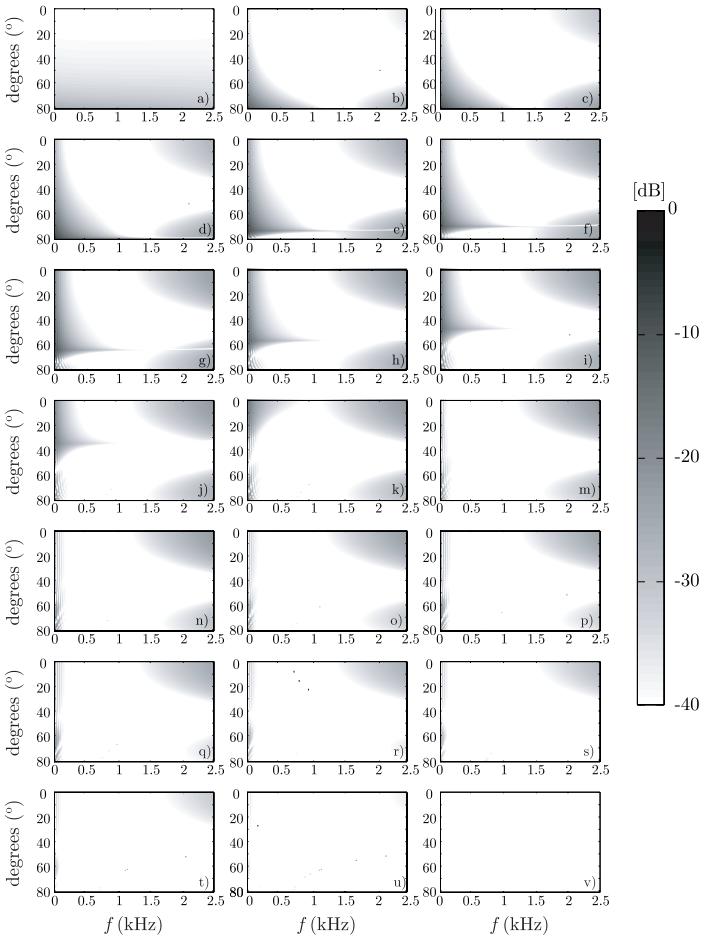

Figure 6.4: The absolute error in decibels for different values of the normal reflection coefficient R_n obtained with the numerical BCs, Eq. (6.5), combined with the leap-frog scheme. From up to down and left to right: a) $R_n = 1$, b) $R_n = 0.9$, c)$R_n = 0.8$, d) $R_n = 0.7$, e) $R_n = 0.6$, f) $R_n = 0.5$, g) $R_n = 0.4$, h) $R_n = 0.3$, i) $R_n = 0.2$, j) $R_n = 0.1$, k) $R_n = 0$, m) $R_n = -0.1$, n) $R_n = -0.2$, o) $R_n = -0.3$, p) $R_n = -0.4$, q) $R_n = -0.5$, r) $R_n = -0.6$, s) $R_n = -0.7$, t) $R_n = -0.8$, u) $R_n = -0.9$ and v) $R_n = -1$.

Nevertheless, there exist other numerical BCs formulations that improve the results in all the range of R_n. For example, in Kowalczyk and van Walstijn [Kowalczyk & van Walstijn (2007)], a FDTD boundary model of a locally reacting surface can be obtained by approximating the first-order spatial and time derivatives with centered finite difference operators.

The resulting equation can be written as an expression for the point lying outside of the modelled space, also referred to as a 'ghost point', which for the right boundary yields

$$p|_{i,j}^{n+1} = \frac{1}{(1+Z\lambda)} \left[\begin{array}{rl} & 2(1-2\lambda^2)p|_{i-1,j}^{n} + \lambda^2(p|_{i,j+1}^{n-1} + p|_{i,j-1}^{n-1}) + 2\lambda^2 p|_{i-1,j}^{n} \\ + & (Z\lambda-1)p|_{i,j}^{n-1} \end{array} \right]. \tag{6.5}$$

Given the use of the 2D wave equation in the boundary model derivation, the upper stability bound is matched for both the boundary and the interior of the room by setting $\lambda = 1/\sqrt{2}$. Therefore, the choice of the Courant number in the 2D model is unambiguous.

The numerical experiment of Eq. (6.5) has been carried out under the same assumptions than those derived from Eq. (6.4). The results of the simulations are depicted in Fig. 6.4 where the scale graded representation shows almost perfect accuracies over all the acoustic impedance range. the absolute error is smaller than -30 dBs, which represents an error of the order of $1/1000$, in all the frequency and angle range. Therefore, Eq. (6.5) seems to be the most appropriate numerical BCs in order to deal with room acoustics applications even for general acoustics problems that involve absorbing BCs since they also give excellent results for $R_n \to 0$.

Conversely, the strong dependence in the parameter λ, which is directly related with the Courant stability number S, complicates either the formulation of Eq. (6.5) combined with PSTD methods, Eq. (4.39), or the extension to three dimensional numerical simulations.

6.4.3 Remarks

In this section we reviewed several formulations of FDTD numerical BCs for either the Euler equations, Eq. (4.16), or the wave equation, Eq. (4.23). First, we discussed the numerical BCs presented by Botteldooren [Botteldooren (1995)] observing accuracies of the order of -30 dB in almost all the range of R_n. Therefore the BCs, Eq. (6.2), are suitable for any acoustics simulation that involves this kind of impedance boundary conditions. However, it is worth emphasizing that Eq. (6.2) requires an staggered mesh since the acoustic pressure and velocities are evaluated at interleaved positions and times. This fact affects to the location of the impedance boundary walls of any numerical enclosure. More specifically, the walls of the numerical domain are restricted at particle velocity nodes instead of centered algorithms whose BCs are defined anywhere in the numerical

space since each node carries information of all the acoustic quantities. In order to solve this problem in Sec. 6.5.1 we present for the first time in the acoustics a semi-empirical BCs for the Eulerian PSTD methods. These numerical BCs require a centered mesh for their implementation; moreover, the flexibility of the semi-empirical BCs are remarkable since they can be easily extended to FDTD methods (see Sec. 6.5.2).

Similarly, we studied two different BCs suitable for algorithms based on the wave equation formulation. First, we analyzed the BCs presented by Huopaniemi et al. [Huopaniemi et al. (1997)], Eq. (6.4), observing acceptable results only in a small range of R_n. We also discussed another formulation presented by Kowalczyk and van Walstijn [Kowalczyk & van Walstijn (2007)] where the numerical BCs update equation is based on the physical properties of an impedance wall. The results derived from this BCs improve the accuracy in all the range of R_n obtaining errors of the order of -35 dB for every angle and frequency. On the other hand, one important drawback of Eq. (6.5) is the strong dependence on the parameter λ which is directly related with the Courant stability number. In the case exposed before, we saw that the election of the parameter λ was unambiguous since it takes the same value than the leap-frog scheme which is $1/\sqrt{2}$. Conversely, in the next chapter BCs, Eq. (6.5), are combined with the PSTD methods observing that in this case the election of λ is confusing since there are two possible values of the Courant stability number.

6.5 Boundary Conditions in PSTD Methods

In the recent years new numerical approaches for solving acoustics problems have appeared: the Pseudo-Spectral Time-Domain (PSTD) methods [Liu (1997)]. In contrast with the common FDTD methods, PSTD methods are characterized by an isotropic dispersion relation. In the last years they have been successfully applied in many different fields such as the propagation of acoustic waves [Liu (1998)], modelling of piezoelectric transducers [Filoux et al. (2008)] or simulation of photonic devices [Pernice (2008)]. However, the formulation of impedance boundary conditions (BC) in the framework of PSTD methods is not reported yet in the technical literature.

In Secs. 6.5.1 and 6.5.3, we present for the first time numerical BCs for either the Eulerian centered algorithms, Eq. (4.38) or the discrete wave equation (4.39). On the one hand, Eulerian BCs are based in a semi-empirical approximation defined through a parameter ξ that is directly related with the acoustic impedance Z. On the other hand, we will see that numerical BCs FDO2 are the best choice to simulate locally-reacting walls when discrete wave equation is used. This formulation is based on finite difference update equation leading to an hybrid formulation of the room acoustics PSTD simulation. Finally, we extend both formulations to FDTD methods (Secs. 6.5.2 and 6.5.4) observing similar accuracies than those studied in Secs. 6.4.1 and 6.4.2.

6.5.1 Boundary Conditions for the Euler Equations

In this section, a novel algorithm capable of simulating frequency-independent impedance BCs is presented by using a semi-empirical approach. We formulate both, the one and two-dimensional BCs for the Fourier PSTD method observing that this novel algorithm provides fairly good results making it suitable for accurate simulations in different fields of acoustics.

In order to implement a partially reflecting BCs within Fourier PSTD method in one dimension we define a parameter, ξ, which controls the ratio between the acoustic pressure and the velocity. Our proposal for those points i that belong to the boundaries is:

- ***For*** $\xi \leq 1$***:***

$$\begin{aligned} v_x|_i^{n+1} &= v_x|_i^n - \frac{\Delta t}{\rho}\mathscr{F}_x^{-1}\left[\imath\frac{2\pi n_x}{N_x\Delta x}\mathscr{F}_x[p|_:^n]\right], \\ p|_i^{n+1} &= \xi\left(p|_i^n - \rho c^2\Delta t\mathscr{F}_x^{-1}\left[\imath\frac{2\pi n_x}{N_x\Delta x}\mathscr{F}_x[v_x|_:^{n+1}]\right]\right). \end{aligned}$$

- ***For*** $\xi > 1$***:***

$$\begin{aligned} v_x|_i^{n+1} &= \frac{1}{\xi}\left(v_x|_i^n - \frac{\Delta t}{\rho}\mathscr{F}_x^{-1}\left[\imath\frac{2\pi n_x}{N_x\Delta x}\mathscr{F}_x[p|_:^n]\right]\right), \\ p|_i^{n+1} &= p|_i^n - \rho c^2\Delta t\mathscr{F}_x^{-1}\left[\imath\frac{2\pi n_x}{N_x\Delta x}\mathscr{F}_x[v_x|_:^{n+1}]\right]. \end{aligned} \tag{6.6}$$

By looking at Eq. (6.6), for $\xi = 1$ we recover the one-dimensional Fourier PSTD scheme directly derived from Eq. (4.38). It is clear from Eq. (6.6) that ξ has to be related with the reflection factor R of the wall. In order to find this relation, we carried out a set of numerical experiments. The experiments were performed on a one dimensional line where an acoustic impulse was located at a relative distance of 50 cells from the wall. The acoustic impulse was approximated by Eq. (5.16). In our experiments we fix the values $f = 2500$ Hz, $n_0 = 19$ and $\Delta t = 1/16000$. The results are shown in Figs. 6.5 and 6.6 where we plot the parameter ξ as a function of the measured reflection coefficient.

From the numerical data we can conclude two interesting properties: on the one hand, the numerical reflection coefficients do not depend on the frequency; on the other hand, there is a strong dependence on the Courant number.

More interesting is the fact that there exist an analytical relation between ξ and R:

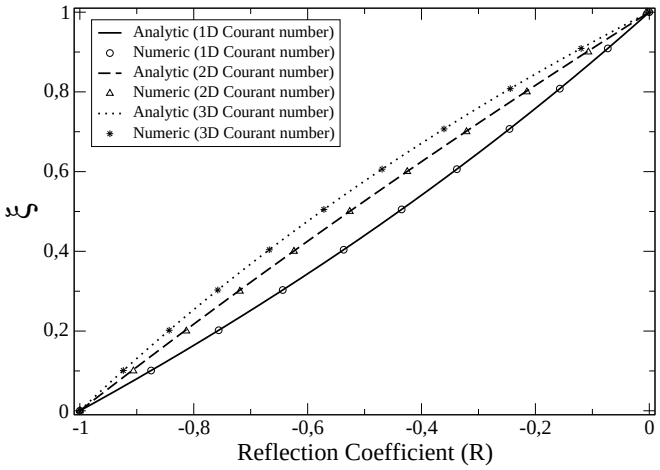

Figure 6.5: Plot of the functional relation between the boundary parameter ξ and the modulus of the reflection coefficient for $\xi \leq 1$ in one dimension. The points represent the numerical values obtained for $S = \frac{2}{\pi}$, $S = \frac{2}{\pi\sqrt{2}}$ and $S = \frac{2}{\pi\sqrt{3}}$ (from bottom to top), while the lines correspond to Eq. (6.7).

- ***For*** $\xi \leq 1$***:***

$$\xi = \frac{1+R}{1+R-2SR} \quad , \tag{6.7}$$

- ***For*** $\xi > 1$***:***

$$\xi = \frac{1-R+2SR}{1-R} \quad . \tag{6.8}$$

In Figs. 6.5 and 6.6 we can clearly see that the analytic expressions, Eqs. (6.7) and (6.8), fit perfectly with the numerical data. In these plots we have shown only three different values of the Courant stability number, $S = \frac{2}{\pi}$, $S = \frac{2}{\pi\sqrt{2}}$ and $S = \frac{2}{\pi\sqrt{3}}$ which are the optimum values of S for 1D, 2D and 3D simulations respectively. We have to remark that the analytical expressions, Eqs. (6.7) and (6.8) are valid for all values of S tested (data not shown).

Finally, it is worth mentioning the fact that for $S = 1$ we have $\xi = \frac{1+R}{1-R} = Z$, where Z is the impedance of the wall.

The results obtained for the one-dimensional case can be easily extended to two dimensions allowing for the construction of a locally reacting BCs.

In order to implement a partially absorbing BCs for ∂V, we follow the same strategy as for the one-dimensional case. Therefore, for those nodes located in the wall, we introduce the boundary parameter ξ in the two dimensional Fourier PSTD equations obtaining:

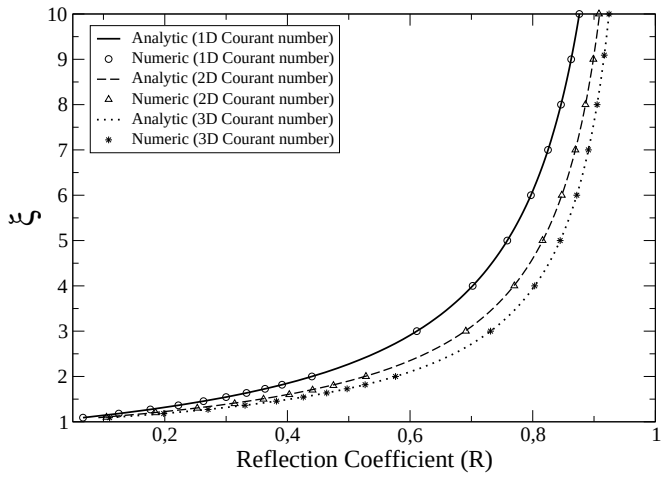

Figure 6.6: Plot of the functional relation between the boundary parameter ξ and the modulus of the reflection coefficient for $\xi > 1$ in one dimension. The points represent the numerical values obtained for $S = \frac{2}{\pi}$, $S = \frac{2}{\pi\sqrt{2}}$ and $S = \frac{2}{\pi\sqrt{3}}$ (from top to bottom), while the lines correspond to Eq. (6.8).

- ***For*** $\xi \leq 1$***:***

$$
\begin{aligned}
v_x|_{i,j}^{n+1} &= v_x|_{i,j}^{n} - \frac{\Delta t}{\rho}\mathscr{F}_x^{-1}\left[\imath\frac{2\pi n_x}{N_x\Delta x}\mathscr{F}_x[p|_{:,j}^{n}]\right], \\
v_y|_{i,j}^{n+1} &= v_y|_{i,j}^{n} - \frac{\Delta t}{\rho}\mathscr{F}_y^{-1}\left[\imath\frac{2\pi n_y}{N_y\Delta y}\mathscr{F}_y[p|_{i,:}^{n}]\right], \\
p|_{i,j}^{n+1} &= \xi\left(p|_{i,j}^{n} - \rho c^2\Delta t\,\mathscr{F}_x^{-1}\left[\imath\frac{2\pi n_x}{N_x\Delta x}\mathscr{F}_x[v_x|_{:,j}^{n+1}]\right]\right),
\end{aligned}
$$

- ***For*** $\xi > 1$***:***

$$
\begin{aligned}
v_x|_{i,j}^{n+1} &= \frac{1}{\xi}\left(v_x|_{i,j}^{n} - \frac{\Delta t}{\rho}\mathscr{F}_x^{-1}\left[\imath\frac{2\pi n_x}{N_x\Delta x}\mathscr{F}_x[p|_{:,j}^{n}]\right]\right), \\
v_y|_{i,j}^{n+1} &= v_y|_{i,j}^{n} - \frac{\Delta t}{\rho}\mathscr{F}_y^{-1}\left[\imath\frac{2\pi n_y}{N_y\Delta y}\mathscr{F}_y[p|_{i,:}^{n}]\right], \\
p|_{i,j}^{n+1} &= p|_{i,j}^{n} - \rho c^2\Delta t\,\mathscr{F}_x^{-1}\left[\imath\frac{2\pi n_x}{N_x\Delta x}\mathscr{F}_x[v_x|_{:,j}^{n+1}]\right].
\end{aligned}
\tag{6.9}
$$

Note that the updating equations for the acoustic pressure in Eq. (6.9) only

consider the gradient in the x direction, thus taking into account the fact that the wall is parallel to the $y-$axis.

From the results obtained for the one-dimensional system we expect that the scheme at the boundaries, Eq. (6.9), produce locally reacting BCs according to,

- ***For*** $\xi \leq 1$***:***

$$\xi = \frac{1+R}{1+R+S\cos(\theta)(1-R)-S(1+R)} \ , \tag{6.10}$$

- ***For*** $\xi > 1$***:***

$$\xi = \frac{RS+S+\cos(\theta)(RS-S+1-R)}{\cos(\theta)(1-R)} \ . \tag{6.11}$$

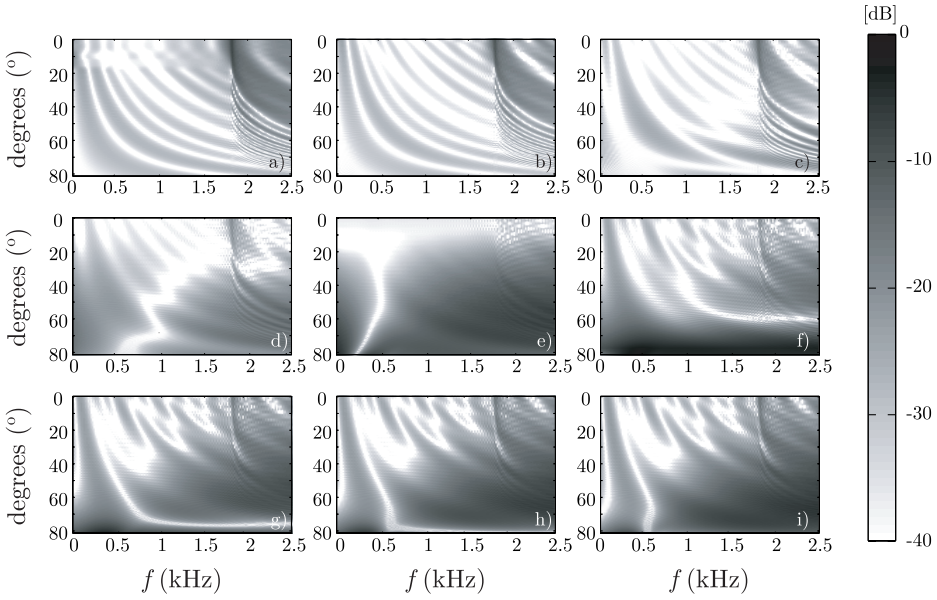

Figure 6.7: The error function for different values of ξ as a function of the angle and the frequency. The plots correspond to: *a)* $\xi = 0$; *b)* $\xi = 0.25$; *c)* $\xi = 0.5$; *d)* $\xi = 0.75$; *e)* $\xi = 1$; *f)* $\xi = 2.5$; *g)* $\xi = 5$; *h)* $\xi = 7.5$; *i)* $\xi = 10$.

In order to verify the relation between the parameter ξ and the reflection coefficient given by Eqs. (6.10) and (6.11), we perform numerical experiments explained in Sec. 6.3. We perform the experiments using the centered PSTD Eulerian algorithm, Eq (4.38), for different values of the boundary parameter ξ.

For each value of ξ, Eqs. (6.10) and (6.11) provide an analytic relation between the modulus of the reflection coefficient and the angle of incidence. By comparing the numerical reflection factor, R_{num}, with the theoretical one provided by Eqs. (6.10) and (6.11).

In Fig. 6.7 we plot the results for nine values of ξ: 0, 0.25, 0.5, 0.75, 1, 2.5, 5, 7.5 and 10 (from a) to i) respectively). Thus practically covering the whole range of values of the reflection coefficient. The simulations show remarkable good results for low angles of incidence ($\theta \leq 40°$) where the deviations from the analytic relation are lower than -30dB for all values of ξ. Deviations from the theoretic behavior are more relevant as the angle of incidence increases and for high frequencies. These results can be easily understood taking into account the fact that the number of cells per wavelength for high frequencies is very low; in particular, for $f = 2500\,Hz$ we have only three cells per wavelength[2]. This suggests that the results are acceptable for frequencies $f \leq 2000\,Hz$ with the space and time discretizations used in the numerical experiments. Finally, it is worth mentioning the fact that errors below -20 dB correspond to regions in which the modulus of the reflection coefficient itself is very low such as for the case in which $\xi = 1$ (graph e) in Fig. 6.7).

6.5.2 Additional Remarks

In the present section we have formulated a new BCs for PSTD methods by introducing a boundary parameter, ξ, in the numerical scheme of the Euler equations. These BCs have been analyzed numerically both, in one and two dimensions. From these studies we have found a very useful relations between ξ and the reflection coefficient (see Eqs. (6.10) and (6.11)). These relations can be written in terms of the wall impedance, Z, as follows:

- ***For*** $\xi \leq 1$***:***

$$\xi = \frac{Z/(\rho c)}{S + Z/(\rho c) - ZS/(\rho c)}\,, \tag{6.12}$$

- ***For*** $\xi > 1$***:***

$$\xi = ZS/(\rho c) - S + 1\,, \tag{6.13}$$

where S is the Courant stability number.

The locally reacting behavior of Eqs. (6.12) and (6.13) has been tested in two dimensions with proper numerical setup (see Sec. 6.3). The low errors found indicate that the proposed BCs can be used in many practical acoustic problems within the powerful emerging PSTD techniques.

[2]This value is the result of the time discretization and the Courant number used: $\Delta t = 1/16000$ and $S = \frac{2}{\pi\sqrt{2}}$

Therefore, the present study develops the necessary ingredients (not previously covered in the technical literature) for using PSTD techniques in many different acoustic problems. It is worth mentioning the fact that, for most practical cases, the presented BCs should be combined with the well-known Perfectly Matched Layer (PML) techniques [Berenger (1996); Yuan et al. (1997)] in order to avoid spurious reflections and the Gibbs effect inherent to all PSTD simulations [Fornberg (1996)].

Moreover, the flexibility of this BCs is a remarkable fact since it can be extended directly to any FDTD Eulerian algorithms formulated in a centered mesh (except the MacCormack scheme). For example, The BCs for the centered leap-frog scheme is easily achieved replacing the spatial Fourier derivatives of Eq. (6.9) by the forward/backward finite difference operators. The explicit form of the scheme is given by

- ***For*** $\xi \leq 1$***:***

$$\begin{aligned} v_x|_{i,j}^{n+1} &= v_x|_{i,j}^{n} - a_1(p|_{i+1,j}^{n} - p|_{i,j}^{n}) \,, \\ v_y|_{i,j}^{n+1} &= v_y|_{i,j}^{n} - a_1(p|_{i,j+1}^{n} - p|_{i,j}^{n}) \,, \\ p|_{i,j}^{n+1} &= \xi \left[p|_{i,j}^{n} - a_2(v_x|_{i,j}^{n+1} - v_x|_{i-1,j}^{n+1}) \right] \,, \end{aligned}$$

- ***For*** $\xi > 1$***:***

$$\begin{aligned} v_x|_{i,j}^{n+1} &= \frac{1}{\xi} \left[v_x|_{i,j}^{n} - a_1(p|_{i+1,j}^{n} - p|_{i,j}^{n}) \right] \,, \\ v_y|_{i,j}^{n+1} &= v_y|_{i,j}^{n} - a_1(p|_{i,j+1}^{n} - p|_{i,j}^{n}) \,, \\ p|_{i,j}^{n+1} &= p|_{i,j}^{n} - a_2(v_x|_{i,j}^{n+1} - v_x|_{i-1,j}^{n+1}) \,. \end{aligned} \tag{6.14}$$

As we mentioned, the spatial derivatives of this numerical BCs are computed through finite difference operators, instead of the Fourier pseudo-spectral BCs, Eq. (6.9). Surprisingly, the numerical BCs, Eq. (6.14), keeps the same relation between ξ and the acoustic impedance Z than the pseudo-spectral formulation (see Eqs. (6.12) and (6.13)). It means that these semi-empirical boundary conditions are not dependent on the numerical approximation used for the spatial derivatives. Therefore, It would be extremely useful to find a theoretical framework to prove the generality of Eqs. (6.12) and (6.13).

In order to test the locally-reacting behavior of Eq. (6.14), we carried out different simulations within a 2D FDTD centered algorithm, Eq. (4.22), fixing $\Delta t = 1/16000$ s and $S = 1/\sqrt{2}$ which is the maximum Courant stability number allowed for the leap-frog scheme. The results of the experiments are plotted in Fig. 6.8. The results exihibit high accuracies since the absolute error is smaller

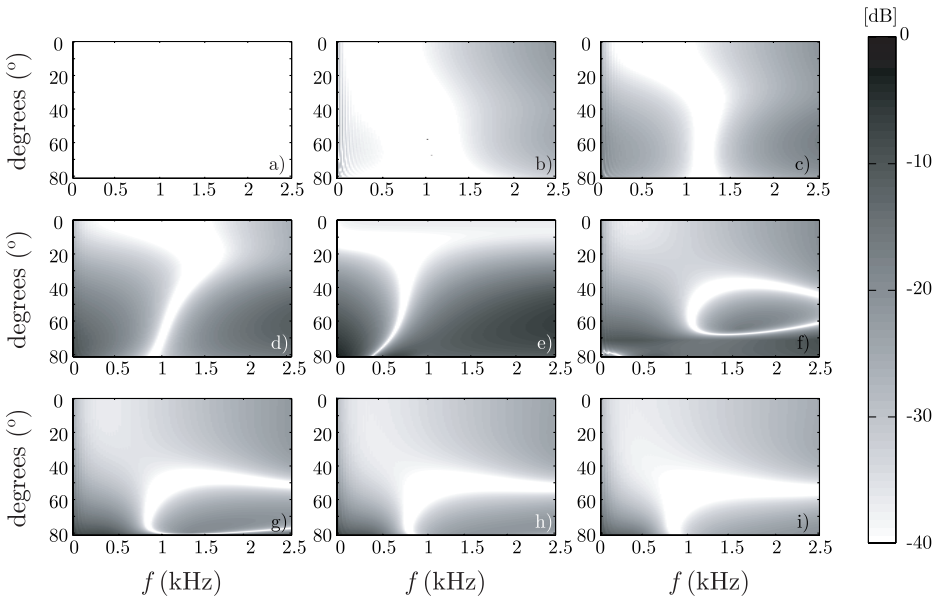

Figure 6.8: The error function for different values of ξ as a function of the angle and the frequency. The plots correspond to: *a*) $\xi = 0$; *b*) $\xi = 0.25$; *c*) $\xi = 0.5$; *d*) $\xi = 0.75$; *e*) $\xi = 1$; *f*) $\xi = 2.5$; *g*) $\xi = 5$; *h*) $\xi = 7.5$; *i*) $\xi = 10$.

than -20 dB for all the range of ξ. Only for $\xi = 1$ we observe an absolute error bigger than -20 dB at high angles, $\theta > 40$. Hence, as in the BCs, Eq. (6.9), based on the Fourier pseudo-spectral techniques, highest absolute errors correspond to regions in which the modulus of the reflection coefficient itself is very low such as for the case in which $\xi = 1$ (see in Fig. 6.8 *e*)). Nevertheless, it is worth mentioning that the improvement of the results are plausible in all the range of ξ, achieving notorious accuracies for $\xi \geq 1$. Another remarkable fact is that the accuracy of the results is preserved until 2500 Hz instead of those obtained with PSTD methods (see Fig. 6.7). It happens because the Courant stability number in FDTD methods ($S = 1/\sqrt{2}$) is less restrictive than in PSTD methods ($S = 2/(\pi\sqrt{2})$). Consequently, the spatial discretization of the FDTD simulations is decreased by a factor $2/\pi$, letting the numerical meshes become considerably thinner than those employed in PSTD simulations. In case the FDTD simulations had been carried out with $S = 2/(\pi\sqrt{2})$, deviations from the theoretical behavior would be more relevant for high frequencies.

Finally, we compare Eq. (6.14) with the results obtained by using the BCs, Eq. (6.2), proposed by Bottledooren [Botteldooren (1995)] for the staggered formulation of the leap-frog scheme (see Fig. 6.2). The main difference between both formulations is the type of mesh employed for discretizing the space,

since the ones, Eq. (6.14), require a centered mesh for their implementation. Apart from this, both experiments were carried out with either the same time discretization or the Courant stability number. Therefore, the study of both, Eqs. (6.14) and (6.2), leads to a fair comparative of the numerical BCs in terms of their accuracy since they are defined under the same assumptions. The similarity of the results is observed in all the acoustic impedance range since the absolute error is lower than -20 dB. Moreover, highest errors appear in both BCs when the reflection coefficients R_n tend to 0 (i.e. ξ tends to 1). Hence, we conclude that the semi-empirical BCs, Eq. (6.14), are more appropriate for FDTD room acoustics simulations given their higher flexibility in numerical domain -characterization of walls in enclosures, allowing for a less restrictive definition than those made in staggered meshes.

6.5.3 Boundary Conditions for the Wave Equation

In the present section, several proposals are made in order to include appropriate impedance boundary condition using the PSTD methods, Eq. (4.39), for room acoustics. Instead of Eulerian problems, we follow a different strategy for obtaining an accurate solution since the most suitable formulation for the numerical BCs are obtained using FDTD methods for the BCs update equation. The results obtained with this algorithms are sufficiently accurate to consider it suitable for room acoustics applications.

The first step consists on discretizing the boundary condition (see Eq. (2.44)) with a uniform spatial sampling frequency Δ. Without loss of generality, from now on we shall consider that the boundary is located parallel to the y-axis on the right hand side of a two-dimensional domain, as illustrated in Fig. 2.4.

In order to implement an impedance boundary condition, one may think about using a PSTD-based algorithm to perform the spatial derivatives on Eq. (2.44), resulting on the following scheme for those nodes (i,j) located at the boundaries:

$$p|_{i,j}^{n+1} = p|_{i,j}^{n} - \frac{Z\Delta t}{\rho}\mathscr{F}_x^{-1}[\imath k_x \mathscr{F}_x[p|_{:,j}^{n}]] \,. \tag{6.15}$$

The first step after the proposal of a finite difference scheme, is to analyze the stability of the finite difference itself. Then, a Von Neumann analysis of the stability is performed [Strikwerda (2004)], which consists on assuming a planar wave, $p(\mathbf{x},t) = \xi^{t/\Delta t} e^{-\imath \mathbf{k}_0^T \mathbf{x}}$, and to find under which conditions $\|\xi\| \leq 1$ occurs. $\mathbf{k}_0$ is the wavenumber vector of the plane wave and ^{T} indicates transposition. For Eq. (6.15), this analysis indicates that Z has to be purely imaginary in order to keep stable that scheme (see the Appendix B for details). This result indicates that this scheme is unconditionally unstable, since in the time domain, this will result into a non physic impedance boundary condition ($Z(\omega) \neq Z^*(-\omega)$, see [Rienstra (1975)] for details).

In order to overcome this handicap, an alternative form of Eq. (2.44) is proposed, which consists on applying a time derivative at both sides of Eq. (6.15),

$$\frac{\partial^2 p(\mathbf{x},t)}{\partial t^2} = -\frac{Z}{\rho}\frac{\partial^2 p(\mathbf{x},t)}{\partial t \partial x} \,. \tag{6.16}$$

This new equation does not essentially change Eq. (2.44), but the finite differences schemes derived from this equation could differ substantially. According to the PSTD algorithm, we obtain a new scheme for the impedance boundary condition,

$$\begin{aligned} p|_{i,j}^{n+1} &= 2p|_{i,j}^{n} - p|_{i,j}^{n-1} \\ &- \frac{Z\Delta t}{2\rho}\mathscr{F}_x^{-1}[\imath k_x \mathscr{F}_x[p|_{:,j}^{n+1} - p|_{:,j}^{n-1}]]. \end{aligned} \tag{6.17}$$

From now on, the former PSTD boundary condition, Eq. (6.15), will be named as PSO1 (*Pseudo-Spectral Order 1*), whereas the latter Eq. (6.17), will be refereed as PSO2 (*Pseudo-Spectral Order 2*). The results from the Von Neumann analysis on PSO2 show that it is an unconditionally stable scheme (see the Appendix B for details).

Despite Eq. (6.17) seems to be an appropriate solution, let us propose a local use of a finite difference time domain scheme at the boundaries. Although the number of hybrid methods involving a PSTD algorithm is really small [Fan et al. (2005)], it will be shown later how a hybrid solution gives fairly better results than a purely PSTD method.

A first approach consists on a central finite difference operator for the time derivatives whereas the spatial derivative uses a forward/backward finite difference operator, depending on the orientation of $\hat{\mathbf{n}}$. As before, we shall consider that the boundary is located parallel to the y-axis. The scheme for those nodes (i,j) located at the boundary is given by:

$$p|_{i,j}^{n+1} = p|_{i,j}^{n} - \frac{Z\Delta t}{\rho\Delta}(p|_{i,j}^{n} - p|_{i-1,j}^{n}) \,. \tag{6.18}$$

Unfortunately, the previous scheme (FDO1 from now on) is stable if $Z \leq \rho c S^{-1}$, where $S = c\Delta t/\Delta$ (see the Appendix), which is a small range of impedance values. In order to overcome this handicap we follow the same procedure as before by using Eq. (6.16). In this case, central finite differences are applied to both first and second order time derivatives, whereas the spatial derivative requires a forward/backward finite difference operator again, just to avoid checking information of the grid points which are located before/after the boundary, respectively. Finally, the numerical scheme reads:

$$p|_{i,j}^{n+1} = \frac{2\rho\Delta}{\rho\Delta+0.5Z\Delta t}p|_{i,j}^{n} - \frac{\rho\Delta-0.5Z\Delta t}{\rho\Delta+0.5Z\Delta t}p|_{i,j}^{n-1} + + \frac{0.5\Delta tZ}{\rho\Delta+0.5Z\Delta t}(p|_{i-1,j}^{n+1} - p|_{i-1,j}^{n-1}) \,. \quad (6.19)$$

The Von Neumann analysis over this particular difference scheme (from now on, FDO2) demonstrates that it is unconditionally stable for all values of Z (see the Appendix B for a detailed derivation).

Although PSO2 and FDO2 seem to be both appropriate as candidates to be used in numerical simulations, a basic situation is simulated in order to confirm the suitability of all the previous presented schemes. The experimental system consists on a 1D scenario where the input signal is located at a relative distance of 50 cells of the impedance boundary condition. In this simple experiment, the input signal is an acoustic impulse approximated by Eq. (5.16),

All the cases are tested with $f = 2500$ Hz, $n_0 = 19$, $\Delta t = 1/16000$ s and the minimum value of the Courant stability number, given by Eq. (4.37), which means that at the highest frequency ($f = 2500$) a minimum value of the number of cells per wavelength is obtained: $N_\lambda \simeq 3$ cpw. The simulation is run during a convenient number of time steps in order to avoid spurious numerical signals and to minimize the truncation error in the analysis of the spectra. Therefore, we compute the average error, ε, of the numerical measured reflection factor R_{meas} with respect to the theoretic reflection factor R_{th}, expressed in dB

Figure 6.9 shows the results of that simulation. As expected from the previous analysis, the PSO1 is unconditionally unstable since Z has to be purely imaginary. Surprisingly, despite PSO2 is an unconditionally stable scheme, results are stable from $R_{\text{th}} = -1$ until $R_{\text{th}} = -0.6$ ($Z = 0.25\rho c$). The reason is not clear; however, in the technical literature it is reported that pseudo-spectral methods can be very sensitive to boundaries [Fornberg (1996)]. Which means that the incorporation of impedance boundary conditions could produce serious instabilities, that they are even independent of the time stepping used.

Fortunately, the finite differences approach give considerable better results. The results of FDO1 (see Fig. 6.9) are in accordance with the Von Neumann analysis. Since the scenario is a 1D simulation, the Courant number is $S = 2/\pi$ implying that the simulation should be stable until $Z \leq 1.57\rho c$ ($R_{\text{th}} = 0.22$), which is confirmed by the numerical simulations where a divergence is found at $R_{\text{th}} \approx 0.2$. However, by using FDO2 the results are completely stable for all the range of values of Z (and hence for all R_{th}). This option is clearly the best option among the rest of proposed methods, since is the unique method which is unconditionally stable and the error is below -30 dB from $R_{\text{th}} = -1$ to $R_{\text{th}} = 0.5$ ($Z \in [0, 3\rho c]$), and around -20 dB for the rest of values. Furthermore, it is also noticeable that for those values of Z for which all the schemes are stable, the error is lower using finite-difference schemes at the boundaries than using a purely PSTD approach.

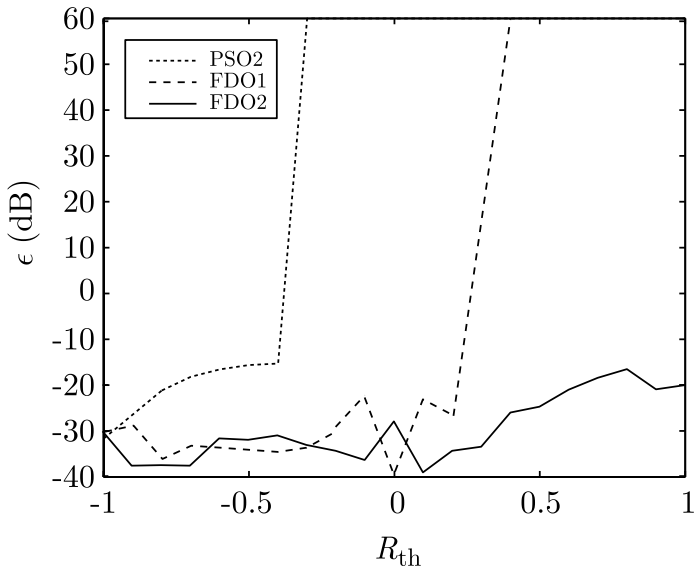

Figure 6.9: Average error, ε, between the measured numerical reflection factor, R_{meas}, and the theoretical one R_{th} in dB.

Then, as a first conclusion, the use of a finite-difference scheme FDO2, Eq. (6.19), for boundary conditions in PSTD schemes provide a unconditionally stable scheme which results have demonstrated good accuracy.

In order to test the suitability of FDO2, Eq. (6.19), combined with multidimensional PSTD simulations, we carried out different numerical experiments according to those defined in Sec. 6.3. The time discretization is fixed to $\Delta t = 1/16000$ s and the Courant stability number is the maximum allowed for the PSTD methods which is $S = 2/(\pi\sqrt{2})$ The agreement with the theoretical predictions is remarkable. The numerical simulations fit fairly good ($\varepsilon \leq -25$ dB) from $R_n = -1$ to $R_n = -0.3$, for all frequencies and angles of incidence. From $R_n = -0.2$ to $R_n = 0.2$, the absolute error increases in the region of high frequencies and small angles of incidence. From $R_n = 0.2$ to $R_n = 0.8$ the results are again more than acceptable with errors $\varepsilon \leq -20$ dB. Finally, for $R_n = 0.9$ and $R_n = 1$, the absolute error is homogeneous with errors of the order of -15 dB.

It is worth mentioning that highly absorbing materials are unusual in most real scenarios. Therefore, the results are most than acceptable for many purposes such as room acoustics or aeroacoustic. Nevertheless, a non-reflecting boundary condition may be accurately approached by using a Perfectly Matched Layer [Berenger (1996); Yuan et al. (1997); Liu (1999)] if needed.

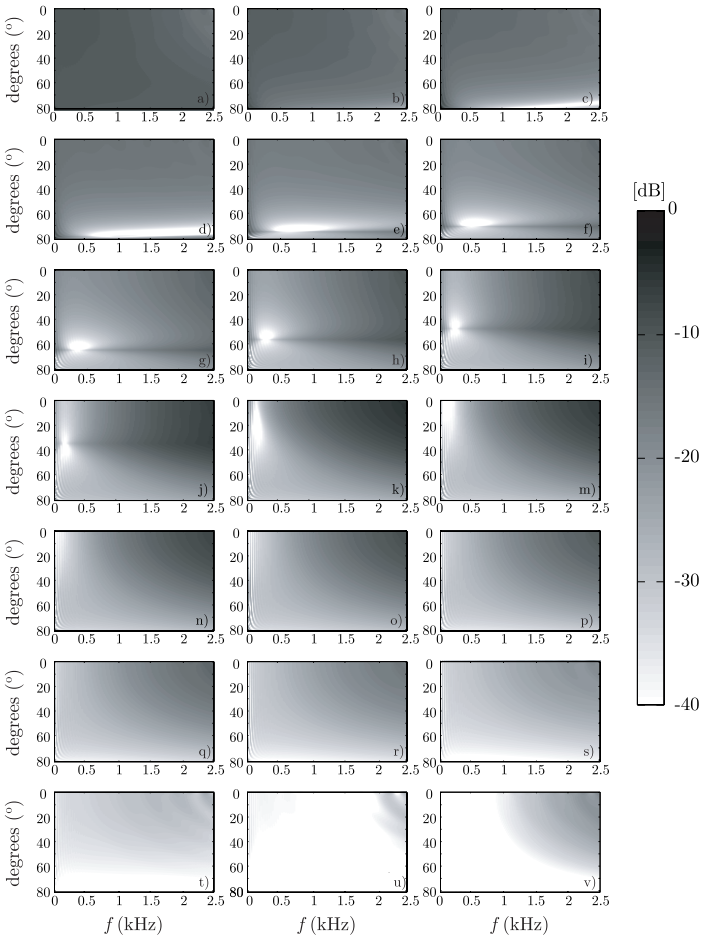

Figure 6.10: The absolute error in decibels for different values of the normal reflection coefficient R_n obtained with the numerical FDO2 scheme, Eq. (6.19). From up to down and left to right: a) $R_n = 1$, b) $R_n = 0.9$, c)$R_n = 0.8$, d) $R_n = 0.7$, e) $R_n = 0.6$, f) $R_n = 0.5$, g) $R_n = 0.4$, h) $R_n = 0.3$, i) $R_n = 0.2$, j) $R_n = 0.1$, k) $R_n = 0$, m) $R_n = -0.1$, n) $R_n = -0.2$, o) $R_n = -0.3$, p) $R_n = -0.4$, q) $R_n = -0.5$, r) $R_n = -0.6$, s) $R_n = -0.7$, t) $R_n = -0.8$, u) $R_n = -0.9$ and v) $R_n = -1$.

These results are not unexpected: on the one hand, the regions with values of the absolute error greater than -10 dB coincide with those regions in which the theoretic reflection coefficient, R_{th}, is smaller than -35 dB when considered in logarithmic scale (see Fig. 6.11). These are quasi-perfect absorbing regions that can not be easily performed for any multidimensional numerical method (as it is well reported in the technical literature [Taflove (1995)]); on the other hand, the increase of error in the range of $R_n > 0.8$ suggests that the use of a finite difference boundary condition FDO2 with a PSTD approximation for the propagation equation gives an inherent error which gets unacceptable only for $R_n \to 1$.

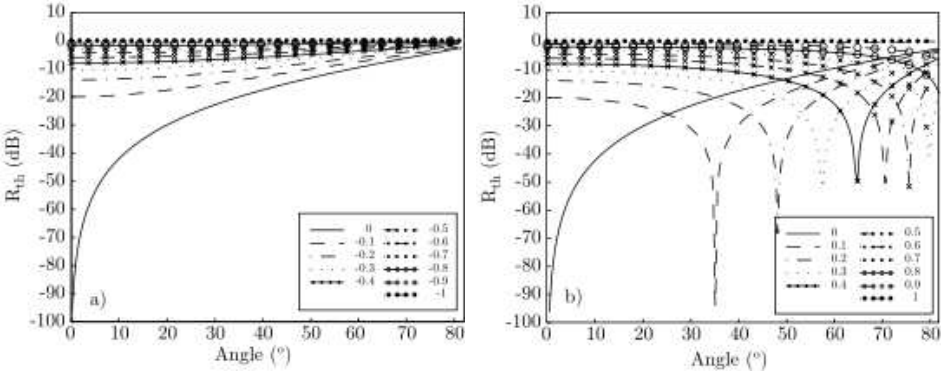

Figure 6.11: Different representations of Eq. (2.42) for different impedances fixed by R_n. On the top it is plotted R_n from -1 to 0 and at the bottom from 0 to 1.

In order to understand more the behavior of FDO2, we test this boundary conditions using the FDTD scheme for the free space propagation, Eq. (4.23). The simulations has been run with the same time discretization, Δt, but with different Courant stability number, and therefore, with different spatial discretization. For these experiments, we fixed the optimum Courant stability number allowed by the leap-frog scheme, $S = 1/\sqrt{2}$. The results are presented in Fig. 6.12. Observe that the accuracy is improved considerably respect the results obtained when FDO2 was combined with PSTD method. More concretely, the results are clearly better in the range of $R_n > 0.3$. Hence, it affirms that the combination of finite differences for the boundaries and psudospectral techniques for the propagation yields an inherent error that for $R_n \to 1$ can be sufficiently relevant to consider critical. On the other hand, the absolute error is increased when the reflection coefficient tends to 0, instead of the porpousal made by [Kowalczyk & van Walstijn (2007)] which achieve almost perfect results in all the range of R, even for the most absorbing impedances. Thus, It suggests that FDO2 leads to considerably high error where R is near to 0, independently of the algorithm employed for the propagation nodes.

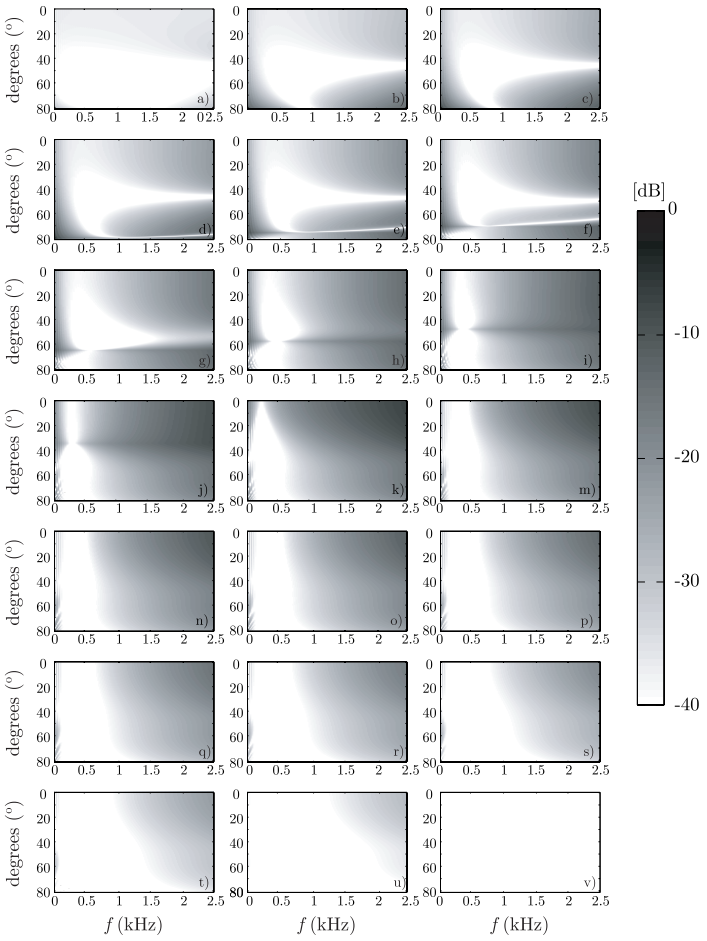

Figure 6.12: The absolute error in decibels for different values of the normal reflection coefficient R_n obtained with the numerical FDO2 scheme, Eq. (6.19) combined with the FDTD algorithm, Eq. (4.23). From up to down and left to right: a) $R_n = 1$, b) $R_n = 0.9$, c)$R_n = 0.8$, d) $R_n = 0.7$, e) $R_n = 0.6$, f) $R_n = 0.5$, g) $R_n = 0.4$, h) $R_n = 0.3$, i) $R_n = 0.2$, j) $R_n = 0.1$, k) $R_n = 0$, m) $R_n = -0.1$, n) $R_n = -0.2$, o) $R_n = -0.3$, p) $R_n = -0.4$, q) $R_n = -0.5$, r) $R_n = -0.6$, s) $R_n = -0.7$, t) $R_n = -0.8$, u) $R_n = -0.9$ and v) $R_n = -1$.

6.5.4 Discussion

In the previous sections we have presented several formulations of numerical BCs for the wave equation based on FDTD and Fourier PSTD methods. We observed that the most suitable BCs for PSTD methods are those based on an hybrid formulation since the numerical BCs FDO2, Eq. (6.19), employs finite differences operators for the spatial derivatives. The results obtained with the hybrid BCs can be used in room acoustics application since the best results appear in the range of the acoustic impedance which corresponds to the one used for characterizing walls in real scenarios.

Moreover, we compare the results of FDO2 combined with PSTD methods to a purely FDTD numerical scheme observing several interesting properties. On the one hand, the hybrid formulation of numerical BCs, Eq. (6.19), gives an inherent error which turns critical for $R \to 1$. On the other hand, independently of the propagation algorithm employed for the numerical simulation, the highest errors are obtained in the regions where the reflection coefficient tends to 0, thus, we can consider without lost of generality that BCs FDO2 does not simulate accurately the locally reacting behaviour of high absorbing walls.

At this point, it is important to confirm whether the best option to implement BCs for the Fourier PSTD methods is the one obtained with the hybrid formulation FDO2. Perhaps, Keeping the strategy of building hybrid algorithms, one could define more appropriate finite difference BCs. Therefore, we carried out several experiments using the numerical BCs presented in Sec. 6.4.2 but, in this case, using the Fourier PSTD algorithm for the propagation nodes.

Firstly, we analyze the suitability for PSTD methods of numerical BCs, Eq. (6.4), presented by Huopaniemi et al. [Huopaniemi et al. (1997)]. The poor accuracy exhibit by these BCs combined with the leap-frog scheme for the propagation nodes (see Fig. 6.3), added to the inherent error due to the formulation of an hybrid algorithm, suggests that BCs, Eq. (6.4), would not be sufficiently appropriate for PSTD simulations.

Nevertheless, the numerical analysis of Eq. (6.4) is presented since it would give information of hybrid formulations for solving room acoustics scenarios. The numerical experiments have been run under the same conditions than the experiments done with Eq. (6.19). So, we use the BCs, Eq. (6.4), for the boundary nodes and the PSTD update equation (4.39) for the propagation nodes, fixing $\Delta t = 1/16000$ s and $S = 2/(\pi\sqrt{2})$ which is the maximum Courant stability number for this algorithm. The results of the experiments are depicted in Fig. 6.13. As we expected, the absolute errors in almost all the range of R_n are higher than -15 dB which is too relevant to consider for PSTD simulations. It is worth emphasizing that the absolute error is increased respect the one obtained with FDTD methods. Therefore, it reaffirms that the combination of Fourier PSTD and FDTD methods adds an inherent error which in this case makes BCs, Eq. (6.4), unacceptable for room acoustics. In order to improve the results obtained with Eq. (6.4), we tested the BCs equation (6.5) proposed by Kovalczyk and van Walstijn [Kowalczyk & van Walstijn (2007)] within a PSTD simulation.

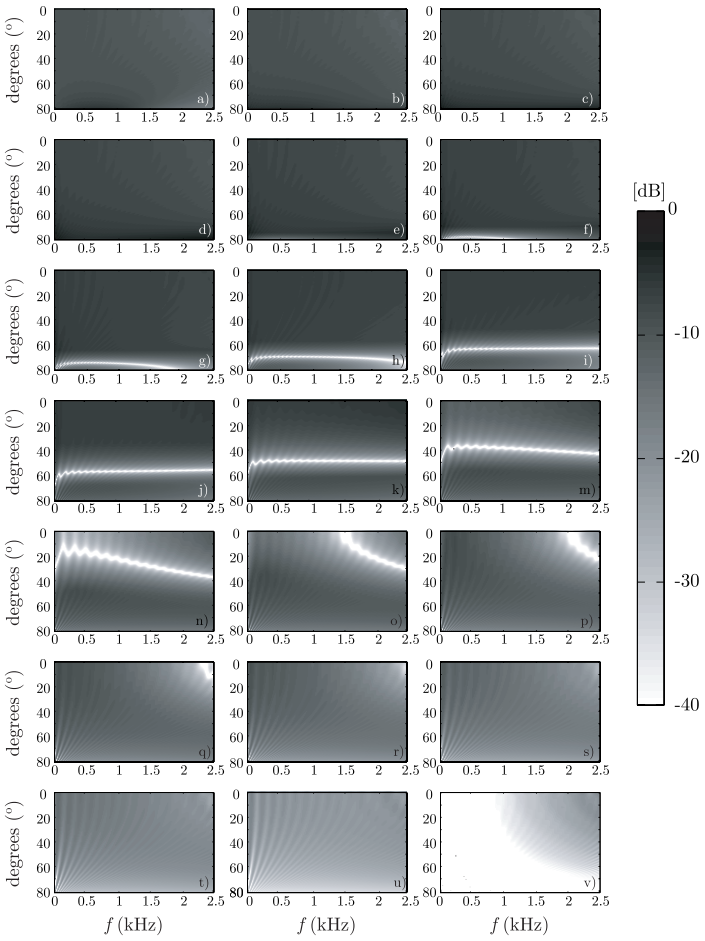

Figure 6.13: The absolute error in decibels for different values of the normal reflection coefficient R_n obtained with the numerical BCs, Eq. (6.4), using the PSTD algorithm, Eq. (4.39), for the propagation nodes. From up to down and left to right: a) $R_n = 1$, b) $R_n = 0.9$, c)$R_n = 0.8$, d) $R_n = 0.7$, e) $R_n = 0.6$, f) $R_n = 0.5$, g) $R_n = 0.4$, h) $R_n = 0.3$, i) $R_n = 0.2$, j) $R_n = 0.1$, k) $R_n = 0$, m) $R_n = -0.1$, n) $R_n = -0.2$, o) $R_n = -0.3$, p) $R_n = -0.4$, q) $R_n = -0.5$, r) $R_n = -0.6$, s) $R_n = -0.7$, t) $R_n = -0.8$, u) $R_n = -0.9$ and v) $R_n = -1$.

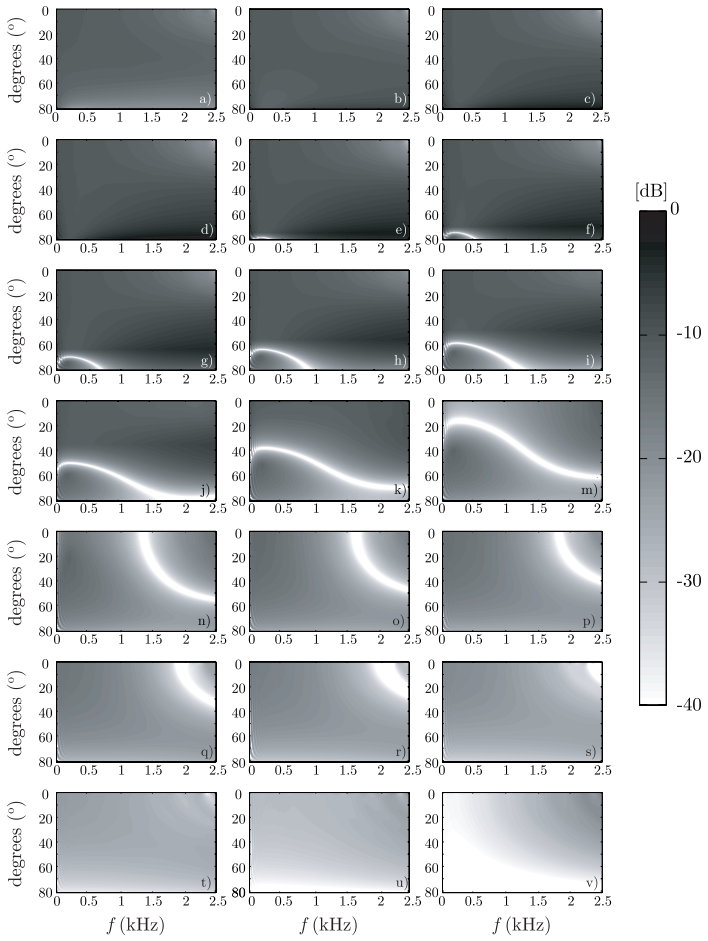

Figure 6.14: The absolute error in decibels for different values of the normal reflection coefficient R_n obtained with the numerical BCs, Eq. (6.5), fixing $\lambda = 1/\sqrt{2}$ and using the PSTD algorithm, Eq. (4.39), for the propagation nodes. From up to down and left to right: a) $R_n = 1$, b) $R_n = 0.9$, c)$R_n = 0.8$, d) $R_n = 0.7$, e) $R_n = 0.6$, f) $R_n = 0.5$, g) $R_n = 0.4$, h) $R_n = 0.3$, i) $R_n = 0.2$, j) $R_n = 0.1$, k) $R_n = 0$, m) $R_n = -0.1$, n) $R_n = -0.2$, o) $R_n = -0.3$, p) $R_n = -0.4$, q) $R_n = -0.5$, r) $R_n = -0.6$, s) $R_n = -0.7$, t) $R_n = -0.8$, u) $R_n = -0.9$ and v) $R_n = -1$.

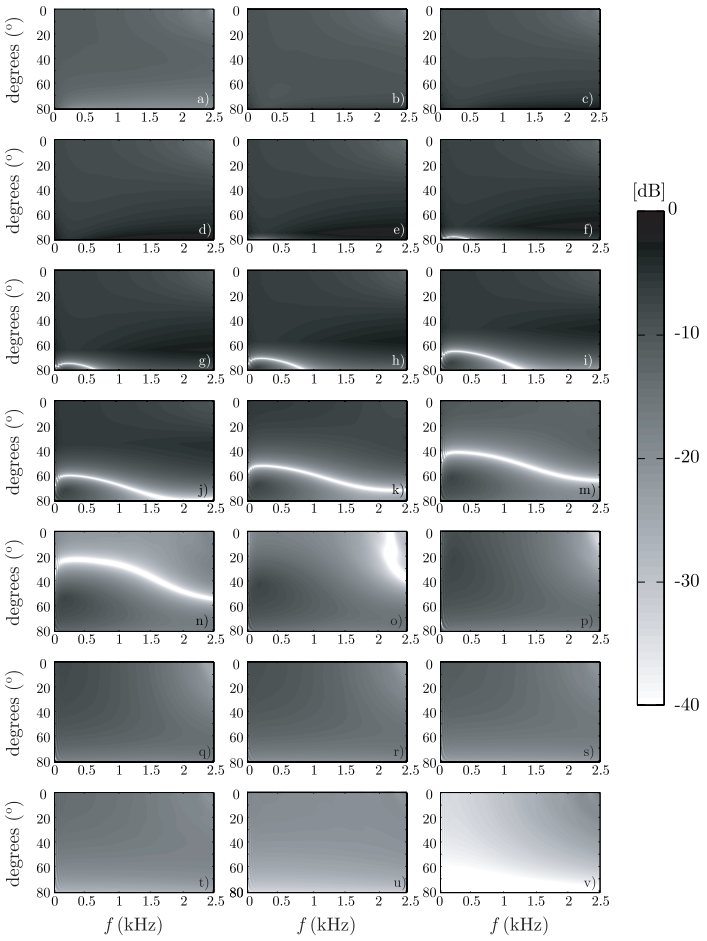

Figure 6.15: The absolute error in decibels for different values of the normal reflection coefficient R_n obtained with the numerical BCs, Eq. (6.5), fixing $\lambda = 2/(\pi\sqrt{2})$ and using the PSTD algorithm, Eq. (4.39), for the propagation nodes. From up to down and left to right: a) $R_n = 1$, b) $R_n = 0.9$, c)$R_n = 0.8$, d) $R_n = 0.7$, e) $R_n = 0.6$, f) $R_n = 0.5$, g) $R_n = 0.4$, h) $R_n = 0.3$, i) $R_n = 0.2$, j) $R_n = 0.1$, k) $R_n = 0$, m) $R_n = -0.1$, n) $R_n = -0.2$, o) $R_n = -0.3$, p) $R_n = -0.4$, q) $R_n = -0.5$, r) $R_n = -0.6$, s) $R_n = -0.7$, t) $R_n = -0.8$, u) $R_n = -0.9$ and v) $R_n = -1$.

On the one hand, we expect better results than those obtained with Eq. (6.4) since the numerical experiments of Eq. (6.5) combined with the FDTD scheme achieve the most accurate results presented in this Thesis. On the other hand, one important drawback of Eq. (6.5) is that the election of the parameter λ is ambiguous due to the close relation between λ and the stability Courant number of the propagation algorithm.

Therefore, we carried out two experiments combining Eq. (6.5) with the PSTD method for the propagation junctions. In one simulation, we fixed $\lambda = 1/\sqrt{2}$ and in the other, $\lambda = 2/(\pi\sqrt{2})$. The election of the coefficients is directly related with the optimum S allowed to be stable by each method. Therefore, both experiments were run with the two dimensional optimum S for PSTD methods. Figs. 6.14 and 6.15 illustrate the numerical results obtained in the simulations. Surprisingly, in both cases, the absolute error is homogeneous and bigger than $-10\ dB$ in whole the range of R_n. Only in $R_n \leq -0.8$, the absolute error is of the order of $-20\ dB$, which can be considered acceptable. Although we expected an inherent error due to the combination of different numerical methods, the high errors obtained in a wide range of R_n for both simulations is completely unexpected. Moreover, the best results of BCs, Eq. (6.5), yield when $\lambda = 1/\sqrt{2}$. more concretely, for $R_n < -0.3$, the absolute error decreases homogeneously from -20 dB to -40 dB which are very low errors and similar to those obtained with our proposal, Eq. (6.19). The results of these experiments confirm that FDO2 BCs is, so far, the best option when PSTD methods are used to solve numerical problems.

6.6 Conclusions

PSTD techniques based on Fourier transforms are used nowadays in many different fields such as the propagation of electromagnetic waves [Liu (1997)] or the simulation of photonic devices [Pernice (2008)]. In all the cases reported in the literature, PSTD is combined with Perfectly Matched Layer [Berenger (1996)] absorbing boundary conditions. In order to use these PSTD methods in room acoustics we develop and validate a numerical implementation of impedance boundary conditions. We have proposed several alternatives in order to simulate locally reacting impedance boundary conditions. More concretely, we separate the analysis depending on the PDE chosen to be numerically solved.

On the one hand, we present for the first time in acoustics a novel semi-empirical BCs for 1D and 2D algorithms for the Eulerian problems. This BCs are obtained through a parameter ξ, which controls the ratio between the acoustic pressure and the velocity. The results obtained in the simulations show that these BCs, Eq. (6.9), are sufficiently accurate to be considered in any room acoustics simulation. Moreover, we extend their formulation into FDTD algorithms defined through centred meshes. The accuracy of FDTD simulations outperforms those obtained with PSTD schemes in the whole range of R_n, getting similar results than those proposed by Bottledooren [Botteldooren

(1995)]. Additionally, the centered formulation of the semi-empirical BCs, Eqs. (6.9) and (6.14), allows to model easily complex enclosures since BCs can be defined at any node of the discrete domain.

On the other hand, among the proposed boundary schemes for the wave equation, we found that the conditions labelled as FDO2 are the most stable and accurate. The FDO2 is defined by Eq. (6.19) which is the numerical finite-difference approach of the second order impedance boundary condition, Eq. (6.16). In this case, we show the convenience of combining Eq. (6.19) with the PSTD scheme for the propagation nodes, Eq. (4.39), for the locally reacting boundary condition.

We performed numerical experiments in order to test the locally reacting behavior of the proposed boundary conditions obtaining fairly good results. In these experiments we computed the absolute error between the numerical and the theoretical reflection factors, analyzing the dependence with frequency and angle of incidence. The absolute error obtained in most cases is below that -25 dB demonstrating the suitability of the method for the computation of acoustic impulse responses. To sum up: we developed and tested a new impedance boundary conditions for PSTD schemes with applications in room acoustics.

Moreover, we tested the boundary conditions FDO2 by using the discrete wave FDTD algorithm, Eq. (4.22), observing better results than in Fourier PSTD simulations. It suggests that the combination of different numerical methods for computing impedance boundary problems gives an inherent error which is increased for positive values of R_n. In order to confirm this assumption, we carried out different experiments with several finite difference BCs [Huopaniemi et al. (1997); Kowalczyk & van Walstijn (2007)] within a PSTD simulation. The results obtained from the numerical experiments confirm either the best accuracy of FDO2 for PSTD applications or the increase of error due to the hybrid formulation employed for PSTD simulations.

In the near future, in order to improve this results, it would be very interesting to give efforts in the study of impedance boundary conditions which are not based on hybrid formulations.

Chapter 7

Conclusions and Outlooks

7.1 Summary and Conclusions

Room acoustics is the science devoted to study the sound propagation in enclosures. Although the mathematical and physical problem is perfectly stated (see Chapter 2), the analytical solution, as a function of the space and time, of the sound propagation in closed environments is in general impossible to obtain. Therefore, the use of computers has emerged as a proper manner to get accurate solutions of the sound phenomena. These computer simulations have a considerable interest of engineers and architects, and also for the entertainment industry, as well as virtual reality applications.

In fact, in this Thesis we presented different approximations used to solve the inhomogeneous boundary problem. Each computational approach gives different advantages and drawbacks that were commented with detail in Chapter 3. For example, the main advantage of geometrical methods is the velocity of the algorithms, letting to construct efficient algorithms, even for real time applications. Conversely, the main drawback of these methods is that they cannot simulate wave phenomena such as diffraction or interference. On the other hand, the wave-based methods take into account the PDE which governs the sound propagation, directly simulating those phenomena that geometrical methods could not perform. More concretely, the use of discrete-time modelling is justified since it allows relatively efficient simulations with a high level of accuracy. Moreover, since these methods are defined in the time-domain, only one simulation is demanded to calculate the impulse response of any room. For these reasons, we decided to study carefully the main aspects of either FDTD methods, which is one of the most important wave-based methods in the time-domain, or PSTD methods, which is a new emerging technique successfully applied in fields such as electromagnetism or optics.

The main motivation of this thesis consists on contributing in the main topics of numerical methods in the time-domain. Firstly, we overviewed the formulation of several FDTD and PSTD algorithms (Chapter 4). Then, we ana-

lyzed the sound source generation for unit impulse signals (see Chapter 5), and finally, we reviewed and made contributions to different implementations of numerical impedance boundary conditions either for FDTD or PSTD methods (Chapter 6).

On the one hand, we overviewed the most popular FDTD and PSTD algorithm for either the Euler or the wave equation. Moreover, we presented an analytical formulation of the dispersion error, supported by numerical experiments of high accuracy. Finally, we rewrote the Eulerian algorithms in terms of non-staggered meshes, in order to improve their flexibility when numerical boundary conditions are required.

On the other hand, the sound source generation of a unit impulse signal was studied and analyzed carefully. We presented the 2D and 3D Green's function which give information of the impulse propagation in the free space, observing that a phenomenon so-called afterglow is appeared when the dimension of the problem is 2. Furthermore, we carried out different numerical experiments of the two most relevant numerical source generation: the soft and the hard sources. Both sources were tested using FDTD and PSTD algorithms observing the best results in the soft source simulations, since they are based on physical assumptions. In fact, the 2D results using the hard source generation are unacceptable since the data obtained in numerical simulations did not fit with the analytical curves. In 3D results, high accuracies are obtained no matter which source generation is employed to simulate the impulse signal. It is worth mentioning, that in PSTD Eulerian algorithm, the punctual source emission generates an artifact that appears along the axis and increases with the dimension of the problem. A proper solution of this consits on using volumetric sources for the generation of the impulse.

Finally, this Thesis deals with the locally reacting impedance concept. Basically, the acoustic pressure and the particle velocity is related through an impedance value which simplifies considerably the boundary model. With this assumption, we analyzed the most common numerical boundary conditions presented in the last decade for FDTD methods using either the Euler or the wave formulation. Moreover, we presented for the first time in room acoustics the formulation of numerical boundary conditions for the Fourier PSTD methods. Firstly, we defined a semi-empirical boundary conditions for the Eulerian algorithms observing acceptable accuracies of the reflexion coefficient. Secondly, we presented numerical boundary conditions suitable for the discrete wave equation. This scheme combines the PSTD methods for the propagation nodes and FDTD methods for the boundary equation. Finally, we extended the PSTD boundary conditions to FDTD formulations leading to remarkable results in terms of accuracy.

7.2 Contributions of the Thesis

In this Thesis, the main contributions can be highlighted as follows:

- Reformulation of FDTD and PSTD algorithms using a centered space and time numerical meshes (Chapter 4). These formulations allow to easily define proper boundary conditions and source generations. Moreover, we formulated the PSTD methods using the wave equation, see in Sec. 4.6.

- A novel methodology for computing the dispersion error via 2D numerical simulations. The accuracies of the results are remarkable, since it gives high accuracies even for algorithms with isotropic dispersion error, see in Sec. 4.8.

- A complete source analysis in 2 and 3 dimensions. We reviewed the most typical source generation using either FDTD or PSTD methods for the propagation nodes (Chapter 5). It is worth emphasizing that the analysis of the source generation using the discrete PSTD wave equation has never been done before.

- A deep overview of the most commonly used numerical boundary conditions for FDTD methods, (Sec. 6.4). We define two novel discrete boundary conditions based on both, the Eulerian and the wave algorithms leading to remarkable accuracies, see in Secs. 6.5.2 and 6.5.4, respectively.

- A novel implementation of numerical boundary conditions for PSTD, but in this case, using the Eulerian algorithms. The boundary conditions are defined through a constant ξ which is related with the impedance, Z, and the Courant stability number, S. Moreover, we showed the numerical results of 2D experiments observing remarkable accuracies, (Sec. 6.5.1).

- Another implementation of numerical impedance boundary conditions for the Eulerian PSTD algorithms. In this case, we defined an hybrid formulation since we used a finite difference operator to build the numerical boundary conditions. Moreover, we presented 2D numerical experiments that confirmed the suitability of the porpousal (Sec. 6.5.3).

Some parts of this thesis have been presented previously, at journal and conferences papers. These publications are listed as follows:

Journal articles

- C. Spa, T. Mateos and A. Garriga. "Methodology for Studying the Numerical Speed of Sound in Finite Difference Scheme". *Acta acustica united with Acustica*.95(4) pp 690 – 695. 2009.

- C.Spa, J. Escolano and A. Garriga. "Impedance Boundary Conditions for Pseudo-Spectral Time-Domain Methods in Room Acoustics". *Applied Acoustics*. Accepted.

- C. Spa, A. Garriga and J. Escolano."Semi-empirical Boundary Conditions for the Linearized Acoustic Euler Equations using Pseudo-Spectral Time-Domain Methods". *Journal of Sound and Vibration.* Submitted.

- C. Spa, A. Garriga, T. Mateos and J. Escolano. "Analysis of Different Sound Source Generation in Multidimensional Numerical Algorithms". *IEEE Transactions on Audio, Spech and Language Processing.* Preprint.

Conferences articles

- A. Garriga, C. Spa and V. López. "Computation of the Complete Acoustic Field with Finite Difference Algorithms".*Proceeding of the Forum Acusticum.* Budapest. 2006

- C. Spa, T. Mateos and A. Garriga. "General Impedance Boundary Conditions in Pseudospectral Time-Domain Methods for Room acoustics", *ASA Conference ACOUSTICS'08.* Paris. 2008.

7.3 Future Research Lines

From the conclusions of this work, some new and challenging research lines could be proposed, being some of them already open. Future work may follow the lines listed here:

- In order to compare with the FDTD and PSTD methods, it would be interesting to explore formulations using different DWM (rectangular, interpolated, triangular/hexagonal...). This analysis would complete the study of the wave-based methods in the time-domain.

- In numerical source generation, the complete analysis of volumetric sources for PSTD methods is an interesting line of research, since punctual sources introduces an undesired artifact in the axis of the simulation that needs to be improved.

- Regarding the PSTD numerical boundary conditions, it would be interesting to obtain analytical background for the semi-empirical impedance boundary conditions based on the Eulerian formulation, since their results can be easily extended into FDTD methods.

- To formulate proper numerical boundary conditions for the PSTD discrete wave equation capable to improve the results that those obtained with FDO2, using either hybrid formulations, as presented in this Thesis or with purely PSTD algorithms.

- To include frequency dependent boundary conditions such as those created by Escolano and Jacobsen [Escolano & Jacobsen (2007)] , in order to obtain more realistic models of simulated walls.

- To compute numerical impulse responses according to experimental measures, such as the Round-Robin room [Bork (2000); Vorländer & Mommertz (2000)]. These simulations would give information of the accuracy of the different numerical boundary conditions presented in this Thesis.

Bibliography

Ahnert, W., Bansal, M., & Feistel, S. (2006). Large scale FEM analysis of a studio room by. Dins *Proc. Audio Eng. Soc. Convention*, ps. Paris, France.

Allen, J. & Berkley, D. (1979). Image method for efficiently simulating small-room acoustics. *Journal of the Acoustical Society America*, 65:943–950.

Bai, M. R. (1992). Study of acoustic resonance in enclosures using eigenanalysis based on boundary element methods. *J. Acoust. Soc. Am.*, 91:2529–2538.

Balanis, C. A. (1997). *Antenna theory*. John Wiley & Sons.

Barton, G. (1989). *Elements of Green's Functions and Propagation : Potentials, Diffusion, and Waves*. Oxford University Press.

Beranek, L. (1940). Acoustic impedance of commercial materials and the performance of rectangular rooms with one treated surface. *J. Acoust. Soc. Am.*, 12(1):14–23.

Beranek, L. L. (1954). *Acoustics*. McGraw-Hill.

Berenger, J.-P. (1996). Three-dimensional perfectly matched layer for the absorption of electromagnetic waves. *Journal of Computational Physics*, 127:363–379.

Bilbao, S. D. (2001). *Wave and scattering methods for the numerical integration of partial differential equations*. Tesi Doctoral, Electrical Engineering Department, Stanford University.

Borish, J. (1984). Extension of the image model to arbitrary polyhedra. *J. Acoust. Soc. Am.*, 75(6):1827–1836.

Bork, I. (2000). A comparison of room simulation software - the 2nd round robin on room acoustical computer simulation. *Acta Acust. united Ac.*, 86:943–956.

Botteldooren, D. (1994). Acoustical finite-difference time-domain simulation in a quasi-cartesian grid. *J. Acoust. Soc. Am.*, 95:2313–2319.

Botteldooren, D. (1995). Finite-difference time-domain simulation of low-frequency room acoustic problems. *J. Acoust. Soc. Am.*, 98(6):3302–3308.

Campos, G. (2003). *Three Dimensional Digital Waveguide Mesh Modelling for Room Acoustics Simulations*. Tesi Doctoral, University of York.

Campos, G. & Howard, D. M. (2005). On the computation efficiency of different waveguide mesh topologies for room acoustic simulation. *IEEE on antennas and wireless propagation letters*, 13(5):1063–1072.

Cátedra, M. F., Pérez, J., de Adana, F. S., & Gutiérrez, O. (1998). Efficient ray-tracing techniques for three-dimensional analyses of propagation in mobile communications: Application to picocell ands microcell scenarios. *IEEE Antennas and Propagation Magazine*, 40(2):15–28.

Chen, G. & Zhou, J. (1992). *Boundary Element Methods*. Academic Press.

Christopoulos, C. (1995). *The Transmission-Line Modelling Method*. Institute of Electrical and Electronics Engineers.

Coleman, C. (1998). A ray tracing formulation and its application to some problems in over-the-horizon radar. *Radio Science*, 33:1187–1197.

Cooley, J. & Tukey, J. (1965). An algorithm for the machine calculation of complex fourier series. *Math. Comput.*, 19:297–301.

Courant, R. (1943). Variational methods for the solution of problems of equilibrium and vibrations. *Bull. Am. Math. Soc.*, 49:1–23.

Cox, T. J., Dalenbäck, B.-I. L., D'Antonio, P., Embrechts, J. J., Jeon, J. Y., Mommertz, E., & Vorländer, M. (2006). A tutorial on scattering and diffusion coefficients for room acoustic surfaces. *Acta Acust. united Ac.*, 92:1–15.

Dalenbäck, B.-I. L. (1996). Room acoustic prediction based on a unified treatment of diffuse and specular reflection. *J. Acoust. Soc. Am.*, 100(2):899–909.

Dominguez, J. (1993). *Boundary Elements in Dynamics*. Elsevier Applied Science.

Duyne, S. A. V. & Smith, J. O. (1993). Physical modeling with the 2-D digital waveguide mesh. Dins *Proc. of the 1993 International Computer Music Conference*. Waseda University, Japan.

Elmasri, S., Pelorson, X., Saguet, P., & Badin, P. (1998). The use of the transmisson line matrix in acoustics and in speech. *International Journal of Numerical Modelling*, 11:133–151.

Embleton, T., Piercy, J., & Olson, N. (1976). Outdoor sound propagation over ground of finite impedance. *J. Acoust. Soc. Am.*, 59(2):267–277.

Embrechts, J. J. (2000). Broad spectrum diffusion model for room acoustics ray-tracing algorithms. *J. Acoust. Soc. Am.*, 107(4):2068–2081.

Escolano, J. & Jacobsen, F. (2007). A note on the physical interpretation of frequency dependent boundary conditions in a digital waveguide mesh. *Acta Acust. united Ac.*, 93(3):398–402.

Escolano, J., López, J. J., & Pueo, B. (2007). Directive sources in acoustic discrete-time domain simulations based on directivity diagrams. *J. Acoust. Soc. Am.*, 121:256–262.

Escolano, J., López, J. J., & Pueo, B. (2009). Broadband directive sources for acoustic discrete-time simulations. *J. Acoust. Soc. Am.*, In press.

Fan, Y., Ooi, B., & Leong, M. (2005). A novel hybrid tdfem-pstd method with stability consideration. *Microwave and Optical Letters*, 47(2):195–197.

Farina, A. (1995). RAMSETE - a new pyramid tracer for medium and large scale acoustic problems. Dins *Proc. Euro-Noise 95*.

Filoux, E., Callé, S., Certon, D., Lethiecq, M., & Levassort, F. (2008). Modeling of piezoelectric transducers with combined pseudospectral and finite-difference methods. *J. Acoust. Soc. Am.*, 123(6):4165–4173.

Fontana, F. & Rocchesso, D. (1998). Physical modeling of membranes for percussion instruments. *Acta Acustica United with Acustica*, 83:529–542.

Fornberg, B. (1996). *A Practical Guide to Pseudospectral Methods*. Cambridge University Press, Cambridge, UK.

Funkhouser, T., Carlbom, I., Elko, G., Pingali, G., Sondhi, M., & West, J. (1998). A beam tracing approach to acoustic modeling for interactive environments. Dins *In Proceedings of the 25th annual conference on Computer graphics and interactive techniques*, ps. 21–32. ACM Press., New York, NY, USA.

Funkhouser, T., Tsingos, N., Carlbom, I., Elko, G., Sondhi, M., West, J., Pingali, G., Min, P., & A.Ngan (2004). A beam tracing method for interactive architectural acoustics. *J. Acoust. Soc. Am.*, 115(2):739–756.

Garriga, A., Spa, C., & López, V. (2005). Computation of the complete acoustic field with finite-difference algorithm. *Proceeding of the Forum Acusticum Budapest*.

Glassner, A. S. (1989). *An introduction to Ray Tracing*. Academic Press.

H. Hacıhabiboğlu, B. G. & Kondoz, A. M. (2007). Source directivity simulation in digital waveguide mesh based room acoustics models. Dins *Proc. AES 30th Int. Conf. on Intelligent Audio Environments*.

H. Hacıhabiboğlu, B. G. & Kondoz, A. M. (2008). Time-domain simulation of directive sources in 3d digital waveguide mesh-based acoustical models. *IEEE Trans. Audio, Speech, and Language Processing*, 16:934–946.

Halton, J. H. (1970). A retrospective and prospective of the Monte Carlo method. *SIAM Review*, 12(1):1–63.

Hodgson, M. (1989). Case history: Factory noise prediction using ray tracing - experimental validation and the effectiveness of noise control measures. *Noise Control Engineering Journal*, 33(3):97–104.

Hodgson, M. & Nosal, E.-M. (1996). Experimental evaluation of radiosity for room sound-field prediction. *J. Acoust. Soc. Am.*, 120:808–819.

Hoffman, J. (1992). *Numerical Methods for Engineers and Scientists*. MacGraw-Hill.

Hu, F. Q. (1996). On absorbing boundary conditions for linearized euler equations by a perfectly matched layer. *Journal of Computational Physics*, 129(1):201–219.

Huopaniemi, J., Savioja, L., & Karjalainen, M. (1997). Modeling of reflections and air absorption in acoustical spaces: a digital filter design approach. Dins *IEEE Workshop on Applications of Signal Processing to Audio and Acoustics (WASPAA'97)*. New Platz, NY, USA.

Ihlenburg, F. (1998). *Finite Element Analysis of Acoustic Scattering*. Springer-Verlag, New York, USA.

Jacobsen, F. (2007). *Handbook of Acoustics*, capítol Sound intensity, ps. 1053–1075. Springer.

Ji, Z., Li, B.-H., Wang, H.-X., Chen, H.-Y., & Sarkar, T. K. (2001). Efficient ray-tracing methods for propagation prediction for indoor wireless communications. *IEEE Antennas and Propagation Magazine*, 43(2):41–49.

Jin, J. (2002). *The Finite Element Method in Electromagnetics*. Wiley-IEEE Press.

Johns, P. (1987). On the relationship between TLM and finite-difference methods for Maxwell's equations. *IEEE Trans. Microwave Theory Tech.*, 35(1).

Kapralos, B. (2006). *The sonel mapping acoustical modeling method*. Tesi Doctoral, York University, Toronto, Canada.

Kelloniemi, A. (2005). Improved adjustable boundary condition for the 2-d digital waveguide mesh. *Proc. of the 8th Int. Conference on Digital Audio Effects (DAFx 05), Madrid*.

Kelloniemi, A., Savioja, L., & Välimäki, V. (2005). Spatial filter-based absorbing boundary for the 2-d digital waveguide mesh. *IEEE Signal Processing Letters*, 12(2):126–129.

Kirkup, S. (1998). *The boundary element method in acoustics*. Integrated Sound Software.

Kleiner, M., Svensson, P., & Dalenbäck, B.-I. (1990). Auralization: Experiments in acoustical CAD. Dins *Proc. of the 89th Audio Eng. Soc. Convention*. Los Angeles, USA.

Kowalczyk, K. & van Walstijn, M. (2007). Multichannel sound reproduction based on Wave Field Synthesis. Dins *International Symposium on Room Acoustics. Satellite Symposium of the 19th International Congress on Acoustics, Seville*.

Krokstad, A., Strom, S., & Sorsdal, S. (1968). Calculating the acoustical room response by the use of a ray tracing technique. *Journal of Sound and Vibrations*, 8:118–125.

Krumpholz, M., Huber, C., & Russer, P. (1995). A field-theoretical comparison of FDTD and TLM. *IEEE Trans. Microwave Theory Tech.*, 43(8):1935–1950.

Kulowski, A. (1985). Algorithmic representation of the ray tracing technique. *Appl. Acoust.*, 18(6):449–469.

Kutruff, H. (2000). *Room Acoustics*. Spon Press.

Lam, Y. W. (1996). A comparison of three diffuse reflection modeling methods used in room acoustics computer models. *J. Acoust. Soc. Am.*, 100(4):2181–2192.

Lee, T.-W. & Hagness, S. C. (2004). A compact wave source condition for the pseudospectral time-domain method. *IEEE on antennas and wireless propagation letters*, 3:253–256.

Lehnert, H. (1993). Systematic errors of the ray-tracing algorithm. *Appl. Acoust.*, 38:207–221.

Li, Q., Chen, Y., & Ge, D. (2000). Comparison study of the pstd and fdtd methods for scattering analysis. *Microwave and Optical Technology Letters*, 25(3):220–226.

Lipson, S. G., Lipson, H., & Tannhauser, D. S. (1995). *Optical Physics*. Cambridge University Press.

Liu, Q. (1998). The pseudospectral time-domain (pstd) algorithm for acoustic waves in absorptive media. *IEEE transactions on ultrasonics, ferroelectrics, and frequency control*, 45(4):1044–1055.

Liu, Q. (1999). Pml and pstd algorithm for arbitrary lossy anisotropic media. *IEEE Microwave and Guided Wave Letters*, 9(2):48–50.

Liu, Q. H. (1997). The pstd algortihms: a time-domain method requiring only two cells per wavelenght. *Microwave and Optical Technology Letters*, 15:158–165.

Liu, Y. (1996). Fourier analysis of numerical algorithms for the maxwell equations. *The Journal of Computational Physics*, 124:396–416.

Maloney, J. G. & Cummings, K. E. (1995). Adaptation of FDTD techniques to acoustic modeling. Dins *11th Annual Review of Progress in Applied Computational Electromagnetics*. Monterey, Canada.

McJown, J. W. & Hamilton, R. L. (1991). Ray-tracing as a design tool for radio networks. *IEEE Network Magazine*, 5(6):27–30.

Miklavcic, S. & Ericsson, J. (2004). Practical implementation of the 3d tetrahedral tlm method and visualization of room acoustics. *Int. Conference on Digital Audio Effects (DAFx04),Verona, Italy*, ps. 262–267.

Morse, P. & Ingard, K. (1986). *Theoretical Acoustics*. Princeton University Press.

Murphy, D., Kelloniemi, A., Mullen, J., & Shelley, S. (2007). Acoustic modeling using the digital waveguide mesh. *IEEE Signal Processing Magazine 2007*, 24:55–66.

Murphy, D. T. (2000). *Digital waveguide mesh topologies in room acoustics modelling*. Tesi Doctoral, Dept. Electronics, University of York, UK.

Namiki, T. & Ito, K. (2000). Investigation of numerical errors of the two-dimensional adi-fdtd method. *IEEE Trans. Microwave Theory Techniques*, 48:1950–1956.

Naylor, G. (1993). ODEON - another hybrid room acoustical model. *Appl. Acoust.*, 38:131–143.

Nosal, E.-M., Hodgson, M., & Ashdown, I. (2004). Investigation of the validity of radiosity for sound-field prediction in cubic rooms. *J. Acoust. Soc. Am.*, 116:3505–3514.

Osa, T., Murakamib, K., Horinouchia, Y., & Takahashia, D. (2006). Application of audience-seats characteristics to the sound field analysis for large enclosures. *Appl. Acoust.*, 68(9):939–952.

Pernice, W. (2008). Pseudo-spectral time-domain simulation of the transmission and the group delay of photonic devices. *Opt. Quant. Electron*, 40:1–12.

Petrausch, S. & Rabenstein, R. (2005). Simulation of room acoustics via block-based physical modeling with the functional transformation method. *IEEE Workshop on Applications of Signal Processing to Audio and Acoustics (WASPAA'05), New Platz, NY.*, ps. 195–198.

Pierce, A. D. (2007). *Handbook of Acoustics*, capítol Basic linear acoustics, ps. 25–112. Springer.

Pietrzyk, A. & Kleiner, M. (1997). The application of the finite-element method to the prediction of soundfields of small rooms at low frequencies. Dins *Proc. 102th Audio Eng. Soc. Convention*, ps. Munich, Germany.

Proakis, J. G. & Manolakis, D. G. (1998). *Digital Signal Processing. Principles, algorithms and applications*. Prentice Hall.

Rienstra, S. (1975). 1d reflection at an impedance wall. *J. Sound Vib.*, 125:43–51.

Rindel, J. (1995). Computer simulation techniques for acoustical design of rooms. *Acoustics Australia*, 23:81–86.

Rossing, T. D. (2007). *Handbook of Acoustics*. Springer.

Savioja, L. (1999). *Modeling Techniques for Virtual Acoustics*. Tesi Doctoral, Helsinki University of Technology, Telecommunications Software and Multimedia Laboratory.

Savioja, L., Backman, J., Järvinen, A., & Takala, T. (1995). Waveguide mesh method for low-frequency simulation of room acoustic. Dins *Proc. 15th Int. Congr. Acoust. (ICA'95)*, volum 2, ps. 637–640. Trondheim, Norway.

Savioja, L., Huopaniemi, J., Lokki, T., & Väänänen, R. (1999). Creating interactive virtual acoustic environments. *J. Audio Eng. Soc.*, 47(9):675–705.

Savioja, L., Järvinen, A., Melkas, K., & Saarinen, K. (1996a). Determination of the low frequency behaviour of an iec listening room. *Proc. of the Nordic Acoustical Meeting*, ps. 55–58.

Savioja, L., Karjalainen, M., & Takala, T. (1996b). DSP formulation of a finite difference method for room acoustics simulation. Dins *Proc. IEEE Nordic Signal Processing Symp. (NORSIG'96)*, ps. 455–458. Espoo, Finland.

Savioja, L., Rinne, T. J., & Takala, T. (1994). Simulation of room acoustics with a 3-D finite difference mesh. Dins *Proceedings of the International Computer Music Conference*, ps. 463–466. Aarhus, Denmark.

Savioja, L. & Välimäki, V. (2003). Interpolated rectangular 3-d digital waveguide mesh algorithms with frequency warping. *IEEE Trans. on Speech and Audio Processing 2003*, 11:783–790.

Schneider, J. B., Wagner, C. L., & Broschat, S. L. (1998). Implementation of transparent sources embedded in acoustic finite-difference time-domain grids. *J. Acoust. Soc. Am.*, 103:136–142.

Schroeder, M. (1973). Computer models for concert hall acoustics. *American Journal of Physics*, ps. 461–471.

Siltanen, S., Lokki, T., Kiminki, S., & Savioja, L. (2007). The room acoustic rendering equation. *J. Acoust. Soc. Am.*, 122(3):1624–1635.

Smith, J. (2007). *Introduction to Digital Filters with Audio Applications*. Setember 2007 Editorial.

Spa, C., Mateos, T., & Garriga, A. (2009). Methodology for studying the numerical speed of sound in finite differences schemes. *Acta Acustica United with Acustica*, 95(4):690–695.

Strikwerda, J. (2004). Finite difference schemes and partial differential equations. *SIAM*.

Sun, G. & Trueman, C. W. (2003). Analysis and numerical experiments on the numerical dispersion of two-dimensional adi-fdtd method. *IEEE Antennas and Wireless Propagation Letters*, 2:78–81.

Svensson, U. P., Fred, R. I., & Vanderkooy, J. (1999). Analytic secondary source model of edge diffraction impulse responses. *J. Acoust. Soc. Am.*, 106(5):2331—2344.

Taflove, A. (1995). *Computational Electrodynamics: The Finite-Difference Time-Domain Method*. Artech House, Norwood, MA.

Tipler, P. A. (2006). *Física*. Editorial Reverté.

Trefethen, L. (1982). Group velocity in finite difference schemes. *SIAM Review*, 24:113–136.

Tsingos, N., Carlbom, I., Elko, G., Kubli, R., & Funkhouser, T. (2002). Validating acoustical simulations in the Bell Labs box. *IEEE Computer Graphics and Applications*, 22(4):28–37.

van der Geest, R. & McChulloch, C. (1998). The virtual room: deriving acoustic characteristics by modelling. *Proocedings of the Institute of Acoustics – Reproduced Sound*, 20:169–180.

VanDuyne, S. & Smith, J. (1995). The tetrahedral digital waveguide mesh. *Proc. of the IEEE Workshop on Applications of Signal Processing of Audio and Acoustics, New Platz, NY*, ps. 234–237.

Vian, J. P. & van Maercke, D. (1986). Calculation of the room response using a ray tracing method. Dins *In Proc. of the ICA Symposium on Acoustics and Theater Planning for the Performing Arts*, ps. 74–78.

Vorländer, M. & Mommertz, E. (2000). Definition and measurement of random-incidence scattering coefficients. *Appl. Acoust.*, 60:187–199.

Wagner, C. & Schneider, J. (2005). An acoustic finite-difference time-domain algorithm with isotropic dispersion. *Journal of Computational Acoustics*, 13(2):365–384.

Whitted, T. (1980). An improved illumination model for shaded display. *Communications of the ACM*, 23(6):343–349.

Wright, J. (1995). An exact model of acoustic radiation in enclosed spaces. *J. Audio Eng. Soc.*, 43:813–820.

Wrobel, L. & Aliabadi, F. (2002). *The Boundary Element Method, Volume 1: Applications in Thermo-Fluids and Acoustics*. John Wiley, New York, USA.

Yee, K. (1966). Numerical solution of initial boundary values problems involving maxwell equations in isotropic media. *IEE Transactions on antennas and propagation*, 14:302–307.

Yuan, X., Borup, D., J.W. Wiskin, M. B., Eidens, R., & Johnson, S. (1997). Formulation and validation of berenger's pml absorbing boundary for the fdtd simulation of acoustic scattering. *IEEE Trans. on Ultrasonics, Ferroelectrics and Frequency Control*, 44:816–822.

Zhao, A. & Mäkinen, R. (2004). An accurate and logically correct way to verify the numerical dispersion relations of fdtd and adi-fdtd methods. *Microwave and Optical Technology Letters*, 40(5):427–431.

Zhou, D. & Huang, W. P. (2001). The perfectly matched layer boundary condition for scalar finite-difference time-domain method. *IEEE Photonics Technology Letters*, 13(5):454–456.

Appendix A

Different Formulations of Perfectly Matched Layers

In this appendix we present the basic formulation of the PML equations for either the Euler equation or the wave equation. On the one hand, the analytical equations of the PML in three dimensions read as follows

$$\begin{aligned}
\frac{\partial v_x(x,y,z,t)}{\partial t} + \sigma_x v_x(x,y,z,t) &= \frac{\partial p(x,y,z,t)}{\partial x} \ , \\
\frac{\partial v_y(x,y,z,t)}{\partial t} + \sigma_y v_y(x,y,z,t) &= \frac{\partial p(x,y,z,t)}{\partial y} \ , \\
\frac{\partial v_z(x,y,z,t)}{\partial t} + \sigma_z v_z(x,y,z,t) &= \frac{\partial p(x,y,z,t)}{\partial z} \ .
\end{aligned} \tag{A.1}$$

Observe that this equation is similar than Eqs. (2.12) to (2.14) except by an additional term proportional to v_μ, where refers to the spatial coordinate x, y or z. Conversely the pressure equation (2.15) differs from the PML equations since it is necessary to define three auxiliary quantities, (p_x, p_y, p_z) that are governed by

$$\begin{aligned}
\frac{\partial p_x(x,y,z,t)}{\partial t} + \sigma_x p_x(x,y,z,t) &= \frac{\partial v_x(x,y,z,t)}{\partial x} \ , \\
\frac{\partial p_y(x,y,z,t)}{\partial t} + \sigma_y p_y(x,y,z,t) &= \frac{\partial v_y(x,y,z,t)}{\partial y} \ , \\
\frac{\partial p_z(x,y,z,t)}{\partial t} + \sigma_z p_z(x,y,z,t) &= \frac{\partial v_z(x,y,z,t)}{\partial z} \ ,
\end{aligned} \tag{A.2}$$

where $p = p_x + p_y + p_z$. In this case, we the three quantities are calculated separately since the coefficient $\sigma = (\sigma_x, \sigma_y, \sigma_z) \in [0,1]$ is related with the absorption of the sound field along the outward normal direction noting that for $\sigma = (0,0,0)$ the Euler equations are recovered. The absorption direction is obtained through the outward direction of the impedance walls (see Fig. 4.4).

Firstly, we present the 3D PML algorithm for the non-staggered leap-frog scheme mentioning that they can be easily extended to the parametric algorithm presented in section . For velocity nodes defined in a non-staggered mesh (i.e. $\mathbf{x} = (i, j, k)$) the numerical update equations for the PML yield

$$\begin{aligned} v_x|_{i,j,k}^{n+1} = & \left(\frac{v_x|_{i,j,k}^{n} - a_1 (p|_{i+1,j,k}^{n} - p|_{i,j,k}^{n})}{1+\sigma_x} \right) \\ v_y|_{i,j,k}^{n+1} = & \left(\frac{v_y|_{i,j,k}^{n} - a_1 (p|_{i,j+1,k}^{n} - p|_{i,j,k}^{n})}{1+\sigma_y} \right) \\ v_z|_{i,j,k}^{n+1} = & \left(\frac{v_z|_{i,j,k}^{n} - a_1 (p|_{i,j,k+1}^{n} - p|_{i,j,k}^{n})}{1+\sigma_z} \right) \end{aligned} \tag{A.3}$$

On the other hand, the pressure update equation is achieved splitting p in p_x, p_y and p_z as

$$\begin{aligned} p_x|_{i,j,k}^{n+1} = & \quad (1-\sigma_x) p_x|_{i,j,k}^{n} - a_2 (v_x|_{i,j,k}^{n+1} - v_x|_{i-1,j,k}^{n+1}) \\ p_y|_{i,j,k}^{n+1} = & \quad (1-\sigma_x) p_y|_{i,j,k}^{n} - a_2 (v_y|_{i,j,k}^{n+1} - v_y|_{i,j-1,k}^{n+1}) \\ p_z|_{i,j,k}^{n+1} = & \quad (1-\sigma_x) p_z|_{i,j,k}^{n} - a_2 (v_z|_{i,j,k}^{n+1} - v_z|_{i,j,k-1}^{n+1}) \end{aligned} \tag{A.4}$$

(A.5)

Similarly, the PML equations for the PSTD algorithm are directly obtained by replacing the spatial finite difference operators by the spectral derivative, see Sec. 4.2. The explicit for the velocity of the numerical scheme reads

$$\begin{aligned} v_x|_{i,j,k}^{n+1} = & \left(\frac{v_x|_{i,j,k}^{n} - \frac{\Delta t}{\rho} \mathscr{F}_x^{-1} \left[\iota \frac{2\pi n_x}{N_x \Delta x} \mathscr{F}_x [p|_{:,j,k}^{n}] \right]}{1+\sigma_x} \right) \\ v_y|_{i,j,k}^{n+1} = & \left(\frac{v_y|_{i,j,k}^{n} - \frac{\Delta t}{\rho} \mathscr{F}_y^{-1} \left[\iota \frac{2\pi n_y}{N_y \Delta y} \mathscr{F}_y [p|_{i,:,k}^{n}] \right]}{1+\sigma_y} \right) \\ v_z|_{i,j,k}^{n+1} = & \left(\frac{v_z|_{i,j,k}^{n} - a_1 \frac{\Delta t}{\rho} \mathscr{F}_z^{-1} \left[\iota \frac{2\pi n_z}{N_z \Delta z} \mathscr{F}_z [p|_{i,j,:}^{n}] \right]}{1+\sigma_z} \right) \end{aligned} \tag{A.6}$$

and for the pressure,

$$\begin{aligned} p_x|_{i,j,k}^{n+1} = & \quad (1-\sigma_x) p_x|_{i,j,k}^{n} - a_2 \rho c^2 \Delta t \mathscr{F}_x^{-1} \left[\iota \frac{2\pi n_x}{N_x \Delta x} \mathscr{F}_x [v_x|_{:,j,k}^{n+1}] \right] \\ p_y|_{i,j,k}^{n+1} = & \quad (1-\sigma_x) p_y|_{i,j,k}^{n} - \rho c^2 \Delta t \mathscr{F}_y^{-1} \left[\iota \frac{2\pi n_y}{N_y \Delta y} \mathscr{F}_y [v_y|_{i,:,k}^{n+1}] \right] \\ p_z|_{i,j,k}^{n+1} = & \quad (1-\sigma_x) p_z|_{i,j,k}^{n} - \rho c^2 \Delta t \mathscr{F}_z^{-1} \left[\iota \frac{2\pi n_z}{N_z \Delta z} \mathscr{F}_z [v_z|_{i,k,:}^{n+1}] \right] \end{aligned} \tag{A.7}$$

We conclude that PML for the Euler equations are a simple and powerful alternative for computing perfectly absorbing BCs.

Conversely, the formulation of PML for the wave equation is not obtained as easy as those achieved using the Euler equations. In this case, it is needed to define two mathematical quantities, $\mathbf{D_1}$ and $\mathbf{D_2}$, without any physical meaning. For illustrative reasons, we focus the analysis for absorptions along the x-axis since it can be straightforwardly derived for other orientations. Therefore, the PML for the wave equation for $\sigma = (\sigma_x, 0, 0)$ takes the following form

$$\begin{aligned} \frac{\partial D_1(x,y,z,t)}{\partial t} - \sigma\rho c^2 D_1(xy,z,t) &= \frac{\partial P(x,y,z,t)}{\partial x} \\ \frac{\partial D_2(x,y,z,t)}{\partial t} - \sigma\rho c^2 D_2(x,y,z,t) = &= \frac{\partial^2 D_1(x,y,z,t)}{\partial t \partial x} \\ \frac{\partial^2 P(x,y,z,t)}{\partial t^2} &= c^2 \frac{\partial D_2(x,y,z,t)}{\partial t} \end{aligned} \tag{A.8}$$

where this PDE is derived from Eulerian formulation of the PMLs. Moreover, D_1 has been discretized in interleave times and positions, $D_1|_{i+1/2}^{n+1/2}$ and D_2 only in interleave times $D_2|_i^{n+1/2}$.

$$\begin{aligned} D_1|_{i+1/2}^{n+1/2} &= \left(\frac{1-\sigma a_1/2}{1+\sigma a_1/2}\right) D_1|_{i+1/2}^{n-1/2} + \frac{\Delta t}{\Delta x(1+\sigma a_1/2)}(P_{i+1}^n - P_i^n) \\ D_2|_i^{n+1/2} &= \left(\frac{1-\sigma a_1/2}{1+\sigma a_1/2}\right) D_2|_i^{n-1/2} + \frac{D_1|_{i+1/2}^{n+1/2} - D_1|_{i-1/2}^{n+1/2} - D_1|_{i+1/2}^{n-1/2} + D_1|_{i-1/2}^{n-1/2}}{\Delta x(1+\sigma a_1/2)} \\ P_i^{n+1} &= P_i^{n-1} + 2P_i^n + c^2\Delta t(D_2|_i^{n+1/2} - D_2|_i^{n-1/2}) \end{aligned} \tag{A.9}$$

In order to obtain the optimum absorption and to minimize the numerical reflexion due to a abrupt changes in medium, σ follows the following expression

$$\sigma_i = -\left(\frac{i}{N_{pml}}\right)^m \frac{(m+1)\log R_0}{a_1 N_{pml}\Delta x} \tag{A.10}$$

where N_{pml} refers to the total number of PML modes in μ-direction, m and R_0 are two constants that are 10^{-2} and 5 respectively. With this non-constant σ it is obtained a smooth change of the medium that it sufficiently absorbing with only 16 grid points. One important drawback of this numerical boundary conditions is that they cannot be extended to PSTD formulations, since it is no posible to compute the spectral derivative of D_1. In PSTD simulations, it is possible to use the FDTD formulation already presented leading to stable simulations. Nevertheless, in order to achieve acceptable absorptions, we must reduce the spatial sampling, δ. Therefore, it would be very interesting to dedicate efforts in the implementation of perfectly absorbing BCs with a purely PSTD algorithm just to avoid the limitations of the hybrid formulations.

Appendix B

Stability Analysis of Numerical Boundary Conditions

In this Appendix, the stability of the proposed boundary conditions is computed through a Von Neumann analysis. For all cases, it is assumed a numerical plane wave of the form $p(\mathbf{x},t) = \Xi^{t/\Delta t} e^{-\imath \mathbf{k}_0^T \mathbf{x}}$, with a wavenumber $\mathbf{k}_0$. The scope is to find the range of values for Z which verify the condition $\|\Xi\| \leq 1$ (or alternatively, $\|\Xi\|^2 \leq 1$) [Strikwerda (2004)].

FDO1 Stability

In this section we analyze the stability of the FDO1 boundary condition (see Eq. (2.44). After applying the Von Neumann procedure to Eq. (2.44), it yields

$$\begin{aligned} \Xi^{n+1} e^{-\imath(k_{x_0} i\Delta + k_{y_0} j\Delta)} &= \Xi^n e^{-\imath(k_{x_0} i\Delta + k_{y_0} j\Delta)} \\ &- \frac{Z\Delta t}{\rho\Delta} \Xi^n e^{-\imath(k_{x_0} i\Delta + k_{y_0} j\Delta)} \\ &- \frac{Z\Delta t}{\rho\Delta} \Xi^n e^{-\imath(k_{x_0}(i-1)\Delta + k_{y_0} j\Delta)}) \end{aligned} \tag{B.1}$$

where $k_{x_0} = \|\mathbf{k}_0\| \cos\theta$ and $k_{y_0} = \|\mathbf{k}_0\| \sin\theta$. After simplifying by the factor $\Xi^n e^{-\imath(k_{x_0} i\Delta + k_{y_0} j\Delta)}$ we obtain:

$$\Xi = 1 - \frac{Z\Delta t}{\rho\Delta}(1 - e^{\imath k_{x_0}\Delta}). \tag{B.2}$$

Therefore, we get for $\|\Xi\|^2$,

$$\begin{aligned}\|\Xi\|^2 &= \left(1-\frac{Z\Delta t}{\rho\Delta}(1-\cos(k_{x_0}\Delta))\right)^2+\left(\frac{Z\Delta t}{\rho\Delta}\sin(k_{x_0}\Delta)\right)^2\\ &= 1+2\left(\left(\frac{Z\Delta t}{\rho\Delta}\right)^2+\frac{Z\Delta t}{\rho\Delta}\right)(1-\cos(k_{x_0}\Delta))\\ &\leq 1+4\left(\left(\frac{Z\Delta t}{\rho\Delta}\right)^2+\frac{Z\Delta t}{\rho\Delta}\right).\end{aligned} \tag{B.3}$$

Since the stability of the numerical scheme is guaranteed when $\|\Xi\|^2 \leq 1$, the range of allowed values for Z is:

$$\frac{Z\Delta t}{\rho\Delta}+1 \leq 0. \tag{B.4}$$

Finally, this scheme is stable if, and only if, $Z \leq \rho c S^{-1}$, where $S = c\Delta t/\Delta$.

FDO2 Stability

Following the same procedure, the stability of Eq. (6.16) leads to the next equation

$$\Xi = \frac{2\rho\Delta}{\rho\Delta+0.5Z\Delta t}-\frac{\rho\Delta-0.5Z\Delta t}{\rho\Delta+0.5Z\Delta t}\Xi^{-1}+\frac{0.5\Delta tZ}{\rho\Delta+0.5Z\Delta t}(\Xi-\Xi^{-1})e^{\imath k_{x_0}\Delta} \tag{B.5}$$

which could be seen as a second order polynomial and where Ξ is solved as

$$\Xi = \left\{1, 1-\frac{2ZS/(\rho c)}{1+ZS/(\rho c)\pm\imath\cot(k_{x_0}\Delta/2)}\right\}. \tag{B.6}$$

Although there exist the solution $\Xi = 1$, one should focus on the more restrictive solution. The next step is to obtain $\|\Xi\|$, which is calculated as

$$\|\Xi\| = 1-\frac{4ZS/(\rho c)}{(1+\frac{ZS}{\rho c})^2+\cot^2(k_{x_0}\Delta/2)}. \tag{B.7}$$

Since $\cot(x) \in]-\infty,\infty[$ and it is situated in the denominator, it maximizes the fraction when $\cot^2(k_{x_0}\Delta/2) = 0$, leading to an expression which is always smaller or equal than the unity, concluding that this scheme is unconditionally stable.

PSO1 Stability

The application of the Von Neumann analysis to a PSTD-based equation requires to take some care with the spatial derivatives. This section deals with the stability of Eq. (6.15). After applying $p(\mathbf{x},t) = \Xi^{t/\Delta t}e^{-\imath\mathbf{k}_0^T\mathbf{x}}$ on this particular equation, the following equation yields

$$\begin{aligned}\Xi^{n+1} \quad e \quad & ^{-\iota(k_{x_0} i\Delta + k_{y_0} j\Delta)} = \Xi^n e^{-\iota(k_{x_0} i\Delta + k_{y_0} j\Delta)} \\ - \quad & \frac{Z\Delta t}{\rho} \mathscr{F}_x^{-1}[jk_x \mathscr{F}_x[Xi^n e^{-\iota(k_{x_0} i\Delta + k_{y_0} j\Delta)}]] \\ = \quad & \Xi^n e^{-\iota(k_{x_0} i\Delta + k_{y_0} j\Delta)} \\ - \quad & \frac{Z\Delta t}{\rho} \Xi^n e^{-\iota k_{y_0} j\Delta} \mathscr{F}_x^{-1}[jk_x \mathscr{F}_x[e^{-\iota k_{x_0} i\Delta}]].\end{aligned} \tag{B.8}$$

From the basis of the Fourier transform, let us to define

$$\mathscr{F}_x[e^{-\iota k_{x_0} i\Delta}] = 2\pi\delta(k_x - k_{x_0}) \tag{B.9}$$

$$\begin{aligned}\mathscr{F}^{-1}[\iota k_x 2\pi\delta(k_x - k_{x_0})] &= \frac{\partial\{e^{-\iota k_{x_0} i\Delta}\}}{\partial(i\Delta)} \\ &= -\iota k_{x_0} e^{-\iota k_{x_0} i\Delta}\end{aligned} \tag{B.10}$$

After that, Eq. (B.8) becomes

$$\Xi = 1 + \iota k_{x_0} \frac{Z\Delta t}{\rho} \tag{B.11}$$

Therefore, after apply the operator $\|\cdot\|^2$ at both sides of the equation, it yields

$$\|\Xi\|^2 = 1 + \left(k_{x_0} \frac{Z\Delta t}{\rho}\right)^2. \tag{B.12}$$

That means this scheme is stable only if Z is purely imaginary.

PSO2 Stability

The stability of Eq. (6.17) follows the same steps than the previous scheme. After applying same the algebraic simplifications once a plane wave is assumed in the equation, it yields

$$\Xi = 2 - \Xi^{-1} + \frac{Z\Delta t}{2\rho} \iota k_{x_0} (\Xi - \Xi^{-1}) \tag{B.13}$$

Rearranging this equation, next equation is obtained

$$\Xi^2 (1 - \iota k_{x_0} \frac{Z\Delta t}{2\rho}) - 2\Xi + (1 + \iota k_{x_0} \frac{Z\Delta t}{2\rho}) = 0 \tag{B.14}$$

Since Eq. (B.14) is a second order polynomial, their roots are calculated as

$$(\Xi - 1)(\Xi - \frac{1 + \iota k_{x_0} \frac{Z\Delta t}{2\rho}}{1 - \iota k_{x_0} \frac{Z\Delta t}{2\rho}}) = 0 \tag{B.15}$$

The first root $(\Xi - 1)$ accomplishes with the stability condition. Therefore, the second root has to be analyzed in detail. After calculating the modulus of this root, it is obtained the following expression

$$\|\Xi\| = \left\| \frac{1 + \imath k_{x_0} \frac{Z\Delta t}{2\rho}}{1 - \imath k_{x_0} \frac{Z\Delta t}{2\rho}} \right\| = 1, \tag{B.16}$$

it shows that this scheme is unconditionally stable.